Strål
säkerhets
myndigheten
Swedish Radiation Safety Authority

Authors: Jeoung Seok Yoon
Ove Stephansson
Ki-Bok Min

Technical Note

# 2016:23

# Modelling of the thermal evolution of the KBS-3 repository at Forsmark and associated induced seismic activity

## Main Review Phase

Report number: 2016:23 ISSN: 2000-0456
Available at www.stralsakerhetsmyndigheten.se

## SSM perspektiv

### Bakgrund

Strålsäkerhetsmyndigheten (SSM) granskar Svensk Kärnbränslehantering AB:s (SKB) ansökningar enligt lagen (1984:3) om kärnteknisk verksamhet om uppförande, innehav och drift av ett slutförvar för använt kärnbränsle och av en inkapslingsanläggning. Som en del i granskningen ger SSM konsulter uppdrag för att inhämta information och göra expertbedömningar i avgränsade frågor. I SSM:s Technical Note-serie rapporteras resultaten från dessa konsultuppdrag.

### Projektets syfte

Det övergripande syftet med projektet är att ta fram synpunkter på SKB:s säkerhetsanalys SR-Site för den långsiktiga strålsäkerheten för det planerade slutförvaret i Forsmark. Innehållet i denna rapport redovisar resultaten från modellering av den termiska utvecklingen i slutförvaret och den seismiska aktivitet som kan uppkomma i samband med värmen som det utbrända kärnbränslet alstrar. I rapporten redovisas också resultaten från modellering av skjuvdeformationer hos sprickor som förekommer i berget för slutförvaret till följd av att ett jordskalv bildas i någon av de större deformationszonerna i slutförvarets omedelbara närhet under den tid som värmen alstras av utbrända kärnbränslet.

### Författarnas sammanfattning

Denna studie redovisar flera förlopp som kan påverka den fysiska integriteten hos ett slutförvar av utbränt kärnbränsle i Forsmak. Två möjliga skäl till detta är: i) den värme som det utbrända kärnbränsle i kapslarna som avklingar med tiden alstrar och som värmer upp berget, och ii) jordskalv som bildas hos någon av de större deformationszoner som finns i slutförvarets omedelbara närhet samtidigt som värme alstras av det utbrända kärnbränslet.

Av speciell vikt för säkerheten är skjuvdeformationen hos existerande sprickor i slutförvaret som kan uppkomma i samband med värmelasten från utbrända bränslet eller skjuvdeformationen som effekt av ett jordskalv som bildas hos någon av deformationszonerna i närheten av slutförvaret eller en kombination av dessa bägge. I SKB:s säkerhetsanalys SR-Site redovisas en största tillåten skjuvdeformation om 50 mm för en bergspricka som förekommer i deponeringshålet för kapseln eller dess omedelbara närhet.

Den termiska belastningen och simuleringen av jordskalv i denna studie har utförts med den tvådimensionella beräkningskoden PFC2D som baseras på diskreta elementmetoden DEM. Beräkningsmodellen simulerar explicita deformationszoner och spricknät som finns i Forsmarksområdet samt för de olika paneler som slutförvaret består av som SKB redovisat. I modellerna simuleras värmelasten som punktkällor. Tvådimensionella horisontal- och vertikalsektioner av slutförvaret har simulerats i denna studie. Ett jordskalv som simuleras i beräkningarna

alstras genom en momentan frigörelse av den töjningsenergi som bergspänningarna alstrat och som lagrats hos de många små sprickor (smooth joints) som deformationszonen består av.

Från simuleringen av värmelastens respons hos sprickorna i slutförvaret visar resultaten att skjuvdeformationerna ökar när temperaturen i bergmassan ökar. Resultaten från PFC2D- simuleringen visar att för såväl en momentan deponering av samtliga kapslar i slutförvaret och för det fall deponeringen sker under en tidsperiod av ca 100 år så överskrids i intet fall deformationsvillkoret 50 mm.

Från samtidig modelleringen av värmelasten och simuleringen av ett jordskalv vid rådande spänningstillstånd i berget visar resultaten från PFC2D-simuleringen av ett jordskalv med magnituden på upp till Mw4.7 på någon av deformationszonerna ZFMMWNW0809A (i horisontalsektionen) respektive deformationszon ZFMA3 (i vertikalsektionen) 100 år efter deponeringen har avslutats leder till att ingen spricka i slutförvaret överskrider gränsvärdet för skjuvdeformationen på 50 mm.

Från en tolkning av modelleringsresultaten där man tar i beaktande de möjliga felkällorna hos beräkningskoden, drar författarna slutsatsen att risken för kapselbrott till följd av värmelasten samt värmelasten i kombination med ett jordskalv vid dagens förhållanden är mycket osannolik.

**Projektinformation**
Kontaktperson på SSM: Flavio Lanaro
Diarienummer ramavtal: SSM2011-3631
Diarienummer avrop: SSM2013-3839
Aktivitetsnummer: 3030012-4077

## SSM perspective

### Background

The Swedish Radiation Safety Authority (SSM) reviews the Swedish Nuclear Fuel Company's (SKB) applications under the Act on Nuclear Activities (SFS 1984:3) for the construction and operation of a repository for spent nuclear fuel and for an encapsulation facility. As part of the review, SSM commissions consultants to carry out work in order to obtain information and provide expert opinion on specific issues. The results from the consultants' tasks are reported in SSM's Technical Note series.

### Objectives of the project

The general objective of the project is to provide review comments on SKB's post-closure safety analysis, SR-Site, for the proposed repository at Forsmark. In particular, this assignment concerns the development of shear displacements of the repository target fractures induced by the heat that is generated from the disposed canisters containing the spent nuclear fuel. This assignment also concerns the shear displacements of the repository target fractures induced by an earthquake at a nearby deformation zone occurring while the repository is under heat loading.

### Summary by the authors

This study addresses several events that could impair the physical integrity of the repository of spent nuclear fuel at the Forsmark site. Two sources of threat are: i) events due to thermal loading on the rock mass by the heat from canisters with spent nuclear fuel, and ii) seismic events, i.e. earthquakes, at the nearby deformation zones that occur during the time when the repository is under heat loading.

The effect relevant to the repository safety is the shear displacement on rock fracture induced either by the effect of thermal loading, or by an earthquake at a nearby deformation zone, or by the combination of the two. In SKB's safety assessment SR-Site, a shear displacement of 50 mm of a target fracture that crosses a canister position in the repository is regarded as the upper limit of canister damage.

Thermal loading and earthquake simulations in this study are conducted using PFC2D, a 2-D discrete element code (DEM). The PFC2D models include a large number of explicitly modelled deformation zones, target fractures and point-heat sources arranged into deposition panels as reported by SKB. Horizontal and vertical cross-sections of the repository are considered in this study.

Earthquake at a specific deformation zone is simulated by a sudden release of the strain energy that was accumulated under the given present-day stress conditions and stored in smaller fractures building up the deformation zones.

From the modelling of heat induced fracture responses, it is observed that the shear displacement of the repository target fractures increase

when the temperature in the rock mass increases. Taking into account of the possible numerical artefacts of PFC2D and outliers in the results, in both modelling cases where the canisters are disposed simultaneously and sequentially, canister damage by the shear of the target fractures due to heat loading is very unlikely.

From the modelling of heat and earthquake induced fracture responses under present-day stress conditions at Forsmark, it is found that for an earthquake with moment magnitude up to Mw4.7 at deformation zones ZFMWNW0809A (horizontal section) and ZFMA3 (vertical section) that occur 100 year after completion of simultaneous deposition, there are no fractures experiencing shear displacements larger than the canister damage threshold of 50 mm.

From the interpretation of the modelling results with full consideration of the possible effects of the numerical artefacts in PFC2D, the Authors draw a conclusion that a risk of canister damage due to the heat loading or the combined loading of heat and the earthquake in present-day conditions is very unlikely.

**Project information**
Contact person at SSM: Flavio Lanaro

Strål
säkerhets
myndigheten
Swedish Radiation Safety Authority

**Authors:** Jeoung Seok Yoon [1], Ove Stephansson [2]
[1] Stephansson Rock Consultant, Berlin, Germany
[2] Seoul National University, Seoul, Republic of Korea

Technical Note 94

# 2016:23

# Modelling of the thermal evolution of the KBS-3 repository at Forsmark and associated induced seismic activity

## Main Review Phase

**Date:** August2016
**Report number:** 2016:23 **ISSN:** 2000-0456
Available at www.stralsakerhetsmyndigheten.se

This report was commissioned by the Swedish Radiation Safety Authority (SSM). The conclusions and viewpoints presented in the report are those of the author(s) and do not necessarily coincide with those of SSM.

# Contents

# 1. Introduction

The Swedish Radiation Safety Authority (SSM) reviews the Swedish Nuclear Fuel Company's (SKB) applications under the Act on Nuclear Activities (SFS 1984:3) for the construction and operation of the KBS-3 repository for spent nuclear fuel and for an encapsulation facility. As part of the review, SSM commissions consultants to carry out work in order to obtain information and provide expert opinions on specific scientific and technical issues. The results from the consultants' tasks are reported in SSM's Technical Note series.

The general objective of the review is to provide comments on SKB's post-closure safety analysis, SR-Site (SKB, 2011), for the proposed repository at Forsmark, Sweden. In particular, this assignment concerns the development of the shear displacement along repository fractures induced by the heat that is generated by the disposed canisters containing the spent nuclear fuel. This assignment also concerns the shear displacement of the repository fractures induced by an earthquake at a nearby deformation zone occurring while the repository is under heat loading from the disposed canisters.

This Technical Note is complementary to SSM Technical Note 2014:59 entitled "Relation between earthquake magnitude, fracture length and fracture shear displacement in the KBS-3 repository at Forsmark – Main Review Phase" (Yoon et al., 2014).

## 1.1. Background

Yoon et al. (2014) have conducted numerical modelling studies that analyse the shear displacement of the repository fractures (also called "target fractures") induced by the heat generated from the disposed canisters containing the spent nuclear fuel and/or by a seismic loading generated by earthquakes occurring at nearby large deformation zones. The heat sources in the thermo-mechanical coupled analyses in Yoon et al. (2014) were modelled similarly to the methods used in a few other SSM reports (Backers and Stephansson, 2011; Ofoegbu and Smart, 2013; Backers et al. 2014), which used the output temperature of SKB's 3DEC modelling results as an input to their modelling. Furthermore, the rock mass temperature in Yoon et al. (2014) was instantaneously increased from 11.2°C to 50°C. Such instantaneous increase of temperature over an area of a few square kilometres caused large thermal shocks to the repository rock mass, and consequently resulted in thermally induced seismic events of relatively large magnitude. The concern that Yoon et al. (2014) might have overestimated the fracture responses led to development of the present assignment where the shear displacement on rock fractures in the numerical model is verified against analytical solutions and results from other numerical codes. Furthermore, thermo-mechanical coupled modelling of the KBS-3 repository is conducted by considering more realistic heat emission curves from the canisters and the effect of possible numerical artefacts in PFC2D discrete element modelling are studied.

## 1.2. Assigned topics

The following tasks are conducted in this study:

- Task A: Verification of the modelling method with PFC2D, in particular reliability of the calculation of fracture shear displacements,
- Task B: Modelling of thermally induced shear displacements of the repository target fractures, distribution of induced seismic events and their magnitudes in the horizontal and vertical sections of the repository,
- Task C: Modelling of earthquake induced shear displacements of the repository target fractures, distribution of induced seismic events during operational and thermal phase of the repository.

Task A's verification of the calculations of fracture shear displacement is covered in Chapter 2.

Task B's analyses of target fracture responses due to thermal loading induced by the heat from the spent nuclear fuel for the horizontal and vertical sections of the repository are covered in Chapters 3, 4 and 5.

Task C's analysis of target fracture responses induced by a tectonic earthquake at a nearby major deformation zone hits the repository during the operational and thermal phase of the repository due to the heat generated by the spent nuclear fuel for the horizontal and vertical sections of the repository is covered in Chapter 6.

General considerations on the modelling results and their implications for the safety of the repository are covered in Chapter 7.

## 1.3. Description of the Appendices

This report contains five Appendices that contain the following:

- Appendix A lists SKB reports that were reviewed for this assignment,
- Appendix B presents close-up views of the parts of the model with fracture intersections. The model is used for verification of the fracture shear displacements covered in Chapter 2.
- Appendix C lists the results of the modelling with FRACOD2D of fracture shear displacements to be compared with the modelling results with PFC2D in Chapter 2.
- Appendix D discusses the results of the heat conduction modelling using COMSOL.
- Appendix E presents additional plots of the modelling results with PFC2D.

# 2. Analysis of fracture shear displacements with PFC2D

In this Chapter, we investigate the shear displacement of a fracture that consists of many smooth joints (Mas Ivars et al., 2011), a so called "PFC fracture", and embedded in an elastic continuum volume. The objective of this investigation is to study if the shear displacement of a single PFC fracture shows the parabolic profile along its trace when subjected to shear stress.

For the verification tests, we use a two-dimensional rectangular model with size of 2 km by 2 km as shown in Figure 1 that contains an inclined and isolated PFC fracture with 500 m half-length and subjected to an anisotropic stress field.

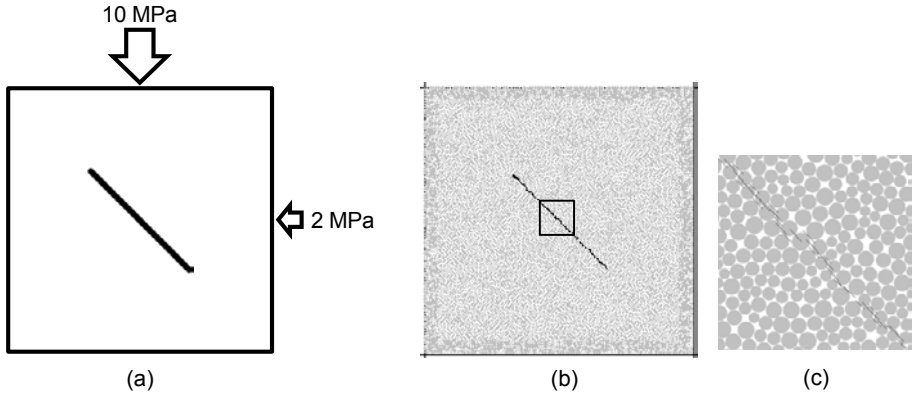


**Figure 1.** (a) Schematics of the verification test model containing an inclined and isolated fracture subjected to shear loading, (b) realization in PFC2D using smooth joints, and (c) enlarged view of the box area in (b) showing a detail of the PFC particles and smooth joints.

## 2.1. Comparison with an analytical solution

According to Pollard and Segall (1987), the shear displacement at an arbitrary position within a fracture can be calculated in 2D using the following equation:

$$u(r) = \frac{2(1-\nu)}{G}\Delta\tau\sqrt{a^2 - r^2} \qquad \text{Eq. (1)}$$

where $\tau_r$ is the remote shear stress, $\tau_c$ is the shear stress on the fracture, $\nu$ is the Poisson's ratio and $G$ is the shear modulus of the rock, $a$ is the fracture half length, and $r$ is the distance of the occurrence point of the shear displacement from the fracture centre. In the example in Figure 2, $\Delta\tau$ is 4 MPa and the friction angle and cohesion of the fracture are assumed to be zero.

Shear displacement of the smooth joints in the PFC2D model are plotted with respect to their distance from the fracture centre and compared in Figure 2 with the analytical solution of Equation (1). The Young's modulus $E$ and the Poisson's ratio $\nu$ of the particle assembly block can be obtained by the uniaxial compression

simulation, and are chosen in range between 59 GPa to 70 GPa and in range between 0.23 to 0.28, respectively. These properties match well with those of the dominant rock type at Forsmark. The shear modulus $G$ is calculated by the equation $G = E/2(1+\nu)$. The smooth joint friction coefficient $\mu$ is set to zero. The simulated shear displacements of the smooth joints with PFC2D show a good match with the analytical solution.

Equation (2) is a 3D version of Equation (1) and gives the shear displacement at a distance $r$ from the centre of a circular fracture of radius $a$:

$$u(r) = \frac{8}{\pi(2-\nu)} \frac{(1-\nu)}{G} \Delta\tau \sqrt{a^2 - r^2} \qquad \text{Eq. (2)}$$

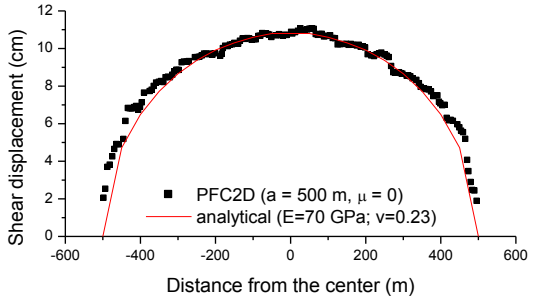


**Figure 2.** Comparison between the shear displacement profile of a PFC fracture and the analytical solution by Pollard and Segall (1987) (Eq.1).

## 2.2. Effect of friction and length of the fractures

This test is intended to investigate how the friction coefficient of the smooth joints affects the shear displacement distribution of a PFC fracture. The bond strength of the smooth joints is set to zero so that the smooth joints of the PFC fracture can slide at the onset of applying shear stress. Five cases of smooth joint friction coefficients (0, 0.1, 0.3, 0.6 and 0.9) are tested and the results are shown in Figure 3a. The results show that the lower the friction of the smooth joints the larger the displacement of the fracture.

The second test investigates how dependent the fracture displacement is on the fracture length in the PFC2D model. In this test, the length of the fracture is varied (half length $a$ = 100, 200, 300, 400 and 500 m) while the friction coefficient $\mu$ is set to 0.1. The results show that the larger the fracture the larger the shear displacement (Figure 3b). The results indicate that the proportionality between the fracture length and the fracture displacement is confirmed by the PFC2D modelling.

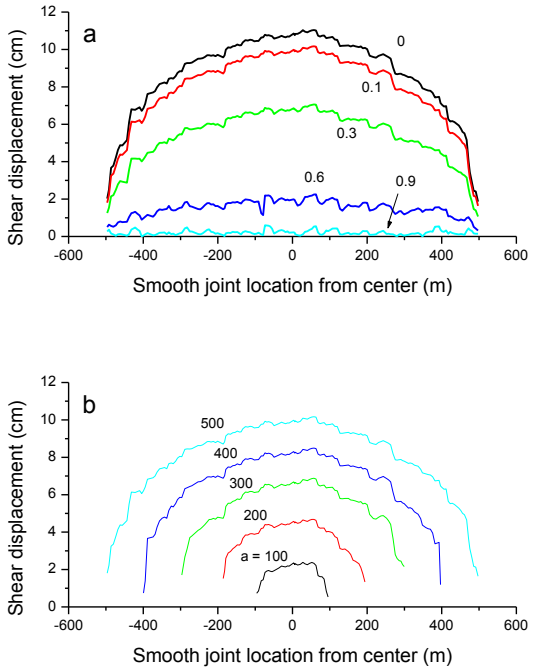


**Figure 3.** Effect of (a) friction coefficients $\mu$ and (b) fracture length 2*a* on the shear displacements of the smooth joints of the PFC fractures.

## 2.3. Effect of intersecting fractures

This test is intended to investigate if the parabolic profile of shear displacement of a PFC fracture holds when multiple PFC fractures are intersecting each other. Three cases are tested: (i) one PFC fracture, (ii) two intersecting PFC fractures, and (iii) five intersecting PFC fractures (Figure 4). The applied principal stresses are the same as in the two previous tests. Figure 5 shows the shear displacement of smooth joints after normalization against the maximum shear displacement in each of the PFC fractures (in red: the largest displacement, green: the smallest displacement, see the colour scale on the left side of Figure 5a). Along the traces of the PFC fractures, we present the absolute shear displacements of the smooth joints in the right column of Figure 5. The figure shows that the parabolic profiles are broken when PFC fractures are intersected by other fractures also under shear. Especially, there is a sudden jump/drop of the displacement at the location of fracture intersection (Figure 5b). The displacement profiles become more complex when there are more fractures intersecting: this is evident when comparing the red curves in Figure 5b and Figure 5c. The intersection between Fracture #3 and #4 in Figure 5c shows one smooth joint with very high shear displacement compared to the others. The particle displacement field near that area of fracture intersection is shown in Figure 6, which indicates that the displacement is localized at one specific particle located at the corner of the two fractures (black arrow). Due to this localized displacement at the particle, the smooth joints attached to the particle undergo relatively large shear displacements compared to other neighbouring smooth joints, also addressed as "spikes" of the fracture shear displacement profiles. The smooth joints are coloured according to 10-based logarithm of the shear displacement.

Appendix B provides close-up views on all seven fracture intersections.

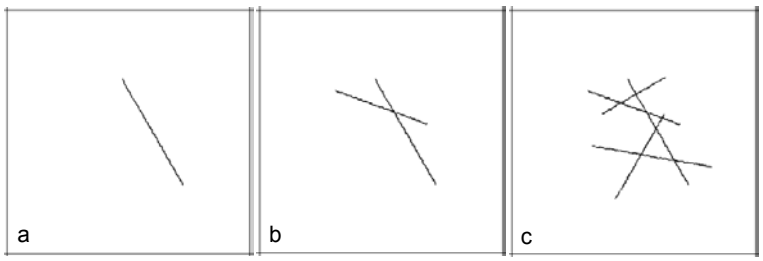


**Figure 4.** PFC2D models containing (a) one PFC fracture, (b) two intersecting PFC fractures, and (c) five intersecting PFC fractures.

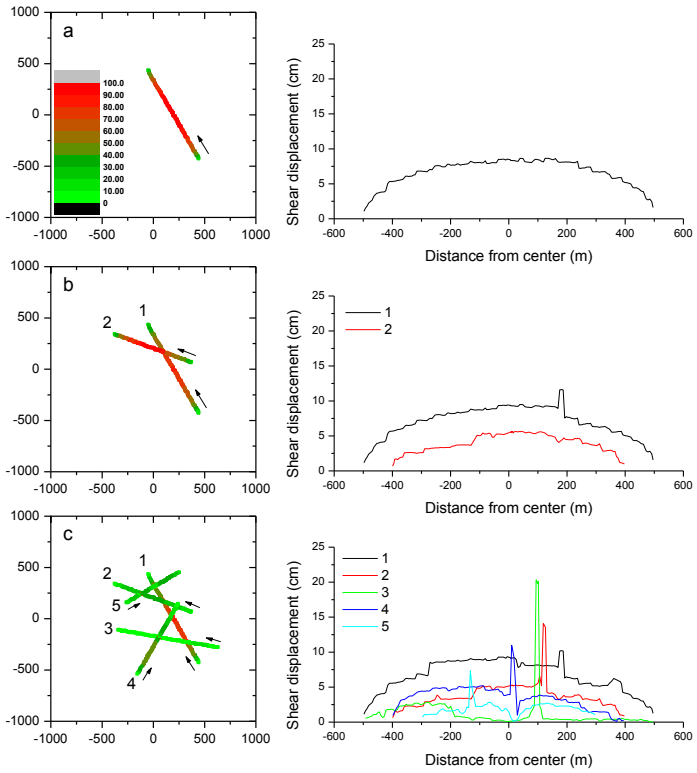


**Figure 5.** Distribution of shear displacement of the smooth joints of (a) one PFC fracture, (b) two intersecting PFC fractures, (c) five intersecting PFC fractures, and their absolute displacement distributions along the traces.

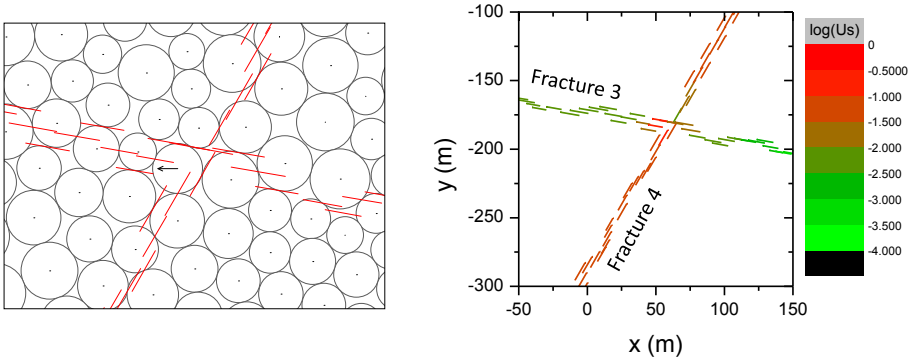


**Figure 6.** (Left) Close-up view of the intersection 6 between Fracture #3 and #4 in the PFC2D model (smooth joints in red and particle displacement with a black arrow). (Right) The smooth joints are coloured according to 10-based logarithm of the shear displacements.

## 2.4. Effect of fracture insertion order

This test is intended to investigate the effect of the order of fracture insertion on the fracture shear displacement, i.e. whether the occurrence of spikes in the profile of the shear displacements is dependent on the order in which fractures are inserted. The five fractures shown in Figure 5c are inserted in the model in different orders: 12345, 54321, 25143, 34152 and 42513. Figure 7 shows the shear displacement profiles of the five intersecting PFC fractures that are placed in the model in different orders.

The results show that the occurrence of spikes and their locations along the fracture trace are dependent on the fracture insertion order, and thus on the particular position of some of the smooth joints.

## 2.5. Effect of particle size

The tests presented in Section 2.4 are repeated on a particle assembly packed with relatively small particles. The tests are intended to investigate the effect of particle size on the shear displacement profile of the fractures. The diameter range of the particle assembly in Section 2.4 is 7 to 22 m, whereas in this section it is chosen to be 5 to11 m for the smaller particle assembly in this section. Figure B-3 in Appendix B shows the shear displacement profiles of the five intersecting PFC fractures that are placed in the smaller particle assembly in different orders.

The results show that, irrespective of the fracture insertion order, there are four distinct peaks or spikes of shear displacements at the intersection of Fracture #1 and #3 and at the intersection of Fracture #2 and #5. The particle displacement fields near the area of intersections for the case of fracture insertion order of 12345 are also shown in Appendix B. Compared to the results in Section 2.4, the use of smaller particle does not seem to have significant effect on reducing the peak displacement, but on the opposite, it seems to increase the peak. Shear displacement profiles of other fractures are more or less the same irrespective of the fracture insertion order.

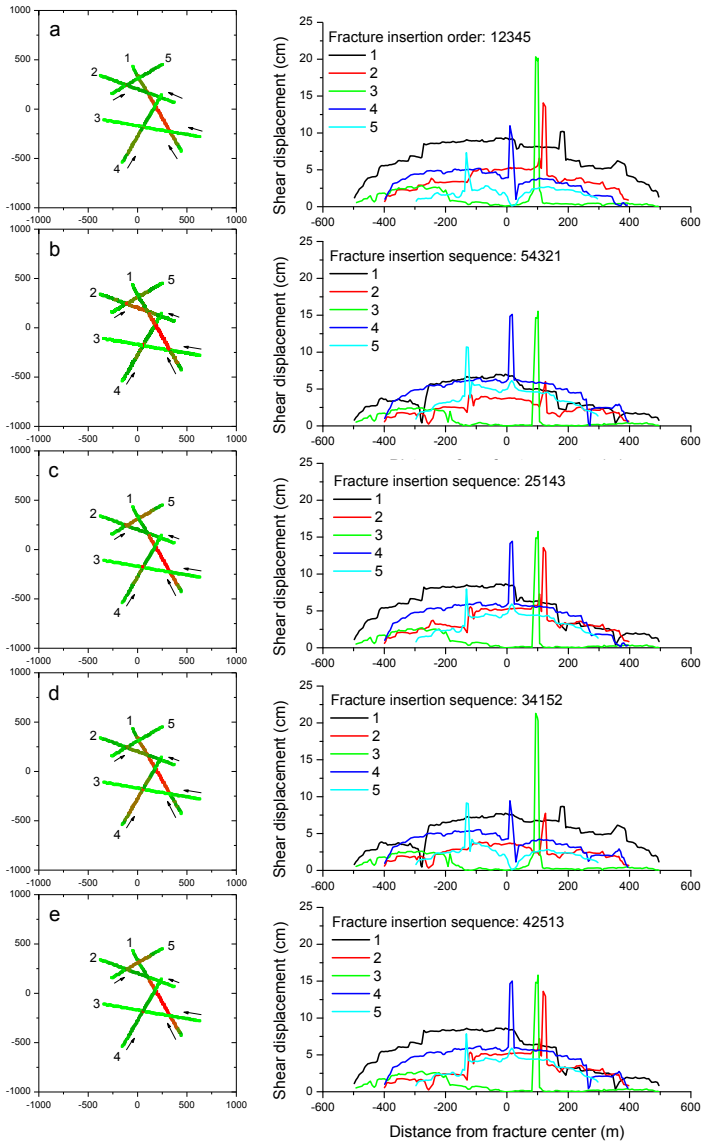


**Figure 7.** Shear displacement profiles of five intersecting fractures placed in different orders, (a) 12345, (b) 54321, (c) 25143, (d) 34152 and (e) 42513 in a larger particle assembly.

## 2.6. Effect of “rattler” particles and stress concentrations at the tips of the fractures

The PFC2D modelling results show that the shear displacement profile of an isolated fracture is in good agreement with the analytical solution. This demonstrates that modelling with PFC2D of shear displacement of a fracture represented by a collection of smooth joints is reliable.

The displacement profile deviates from the parabolic shape when fractures are intersecting. The shear displacement profiles of five intersecting fractures shown in Figure 5 are modelled with FRACOD2D (Shen, 2014) and results are presented in Figure 8. In general, the parabolic shear displacement profile for an isolated fracture is interrupted at the intersection with other fractures. Also as seen in Figure 8a and 8b, the maximum displacement in the models is larger than for an isolated fracture of the same size.

Differently than for the PFC2D results, the results from FRACOD2D show smooth distributions of the displacement along the fractures independently of the intersections. This is due to the fact that a fracture modelled in FRACOD2D is perfectly linear, whereas a fracture modelled in PFC2D consists of many discrete smooth joints. Nevertheless, for an isolated fracture case, the maximum shear displacement takes place at the centre of the fracture and the calculated magnitudes the same identical for the two models (8.32 cm as in Figure 8a).

For the case with two intersecting fractures, the FRACOD2D results also show a displacement jump at the intersection. However, the displacement profile of Fracture #1 does not show a spike of the displacement as in the PFC2D model in Figure 5b where it reaches about 12 cm.

For the case with five intersecting fractures, the difference between the two modelling results becomes more distinct. The PFC2D results show four distinct displacement spikes at the fracture intersections, whereas the FRACOD2D results show no displacement spikes but only several smaller jumps at the intersections.

In summary, the displacement profiles of some of the PFC fractures are showing significantly large of the shear displacement values at the intersections. As there is no closed form solution for calculating shear displacements of intersecting fractures, efforts have been made to investigate if such peak displacements at the intersection areas are physically possible or are only local numerical errors or artefacts produced by PFC2D.

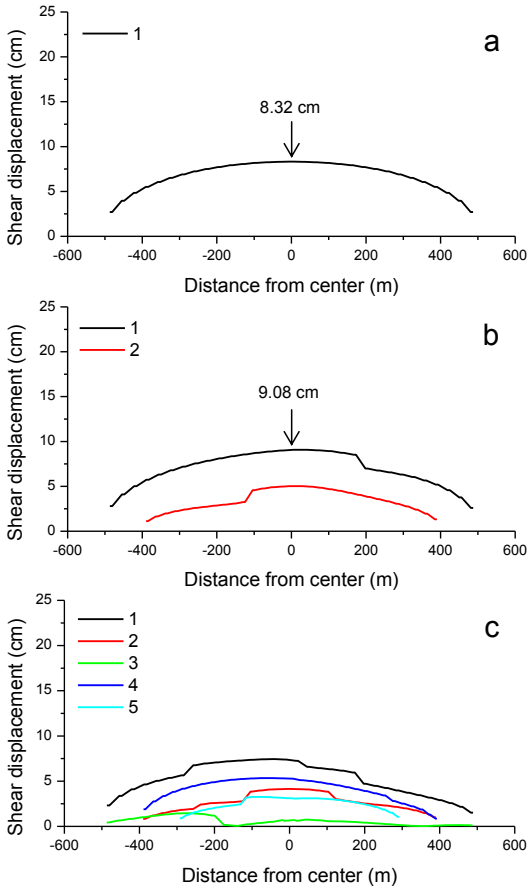


**Figure 8.** Shear displacement profiles of (a) single isolated fracture, (b) two intersecting fractures, and (c) five intersecting fractures modelled with FRACOD2D.

From a number of tests, it is found that irrespective of the particle size and the order of fracture insertion, there are always several spikes of the shear displacement at some of the fracture intersections. By the stress analysis in FRACOD2D (see Appendix C) and in PFC2D (see Appendix C, Figures C-10 and C-11), it is confirmed that stresses tend to concentrate at the fracture intersections where the spikes occur.

The stress analysis demonstrates that the spikes of shear displacement at the fracture intersection in PFC2D are due to excessive stress concentration on rigid particles as shown in Figure 6. Localized displacement of one particle leads to concentrated shear displacements of the smooth joints around the particle. This is the reason why significantly large shear displacement spikes occur at the fracture intersections.

In reality, however, stress concentrations at the fracture tip or at the fracture intersection may easily lead to local failure of the rock at that point. If the rock at the location of fracture intersection fails, a localized displacement as it was modelled in PFC2D, i.e. displacement spikes, may not be observed. The failure of the rock near the fracture intersection may dissipate some of the energy concentration. Therefore, in reality, fracture shear displacement at that location would be reduced. But at the same time, the left-over energy after the local failure could go into the neighbouring

space and volume and slightly increase the shear displacement adjacent to the fracture intersection.

Later investigation on this issue has led to further findings namely, that the highly localized displacement on one particle in PFC2D as shown in Figure 6 is due to the fact that the particle detaches from the surrounding particles. For this reason, particles behaving this way are named “rattlers”. The rattler particle occurs due to stress concentration as shown in the stress analysis (see Appendix C) and depends on the fact that the particles in PFC2D are rigid and non-breakable. When high stress concentrations are developed at some smooth joint intersections, the bond strength between the particles can be overcome and the bonds may break. The particle might then lose all bonds with the neighbouring particles and become a rattler.

In order to mitigate the side effects of the rattler particles, the concentrated stress and the particle rigidity, we have developed a scheme by FISH programming in the PFC2D code. The developed scheme has two functions: first, to detect and eliminate the rattlers, therefore the smooth joints attached to the rattler particles are not taken into account in the calculation of the shear displacement of a fracture; second, to detect and soften the rigid particles that in reality would be damaged by fracturing. These “virtually damaged” particles are located where the level of concentrated stress is envisaged to be high enough to induce breakage of the material inside the particles. Detection of the virtually damaged particles is done using a Mohr-Coulomb failure criterion with parameters (tensile strength, cohesive strength and frictional angle) higher and different than those assigned to the particle smooth joints to mimic the failure of the rock inside the particle.

This scheme is applied to the PFC2D model with five intersecting fractures (Figure 4c) and the results are shown in Figure 9. The displacement profiles show that all the large spikes are eliminated compared to Figure 5c. However, there are still some points (indicated by red arrows in Figure 9) where the displacements are locally higher. We have investigated this issue by using a model with higher particle resolution and found that those higher displacements can be eliminated.

A consequence of introducing “virtual damage” of some particles is that the stress concentrations at the tips of fractures might break some particles closest to the tip. This in turn increases the stresses on their neighbouring particles and smooth joints, which can experience larger displacements than before the application of the “virtual damage”. This can be seen for example for the left tip of Fracture #1 when comparing Figure 5c and Figure 9.

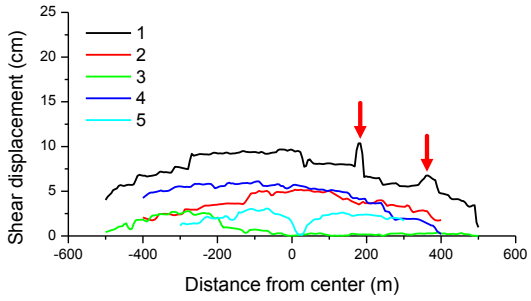


**Figure 9.** Distribution of shear displacement of the smooth joints of five intersecting PFC2D fractures after the spikes are eliminated by deleting the rattler particles and softening the virtually damaged particles.

This confirms that the large spikes of the shear displacement at the fracture intersections modelled in PFC2D should be regarded as numerical artefacts due to rigid and non-breakable particles. Figure 9 shows that those numerical artefacts can be properly handled and the displacement spikes can be eliminated.

## 2.7. Selection of representative shear displacements of fractures in PFC2D models

Considering that the elimination of the "rattler particles" and the "virtual damage" in relation to high stress concentrations at the tips of the fractures was not applied in the modelling presented in this report, it is then necessary to investigate how to properly calculate representative shear displacements of the fractures in the PFC2D models of the repository.

In Yoon et al. (2014), the mean value of the shear displacement of the smooth joints along a fracture in the PFC2D model was chosen as a representative shear displacement of a PFC2D fracture and used for the safety assessment of the repository. In this case, it can be said that the displacement of a PFC fracture is overestimated as spike shear displacement values of the smooth joints at the intersections are taken into account in the calculation of the mean.

As an alternative choice to calculate a representative shear displacement of a PFC2D fracture, we suggest using the median value. By using the median value of shear displacement of the smooth joints that represent a PFC2D fracture, multiple large shear displacement values, numerical artefacts in the model, are overlooked.

Moreover, in case of an isolated fracture under shear as shown in Figure 5a, choosing the median displacement instead of the mean displacement is more conservative due to the fact that for the kind of shear displacement distribution observed in the models, the median is usually larger than the mean value, as also shown in Figure 10a.

For the highest level of conservativeness of the safety assessment of the repository, one should use the maximum displacement as a representative displacement of a fracture. However, for choosing the maximum displacement, the correction scheme for "rattlers" and "virtual damage" introduced above should be applied first. In this report, we choose to use the median displacement since the correction scheme was developed after and not applied to the results presented in the following chapters.

In case of an fracture as Fracture #2 in Figure 5c, choosing the median instead of the mean displacement is acceptable due to the fact that the median is not sensitive as the mean value to the large peak values in the model that come from the numerical artefact. Moreover, the difference between the mean and the median is less than 10%. Figure 10b shows the median and mean values of the shear displacement for a fracture intersected by other fractures under shear as Fracture #2.

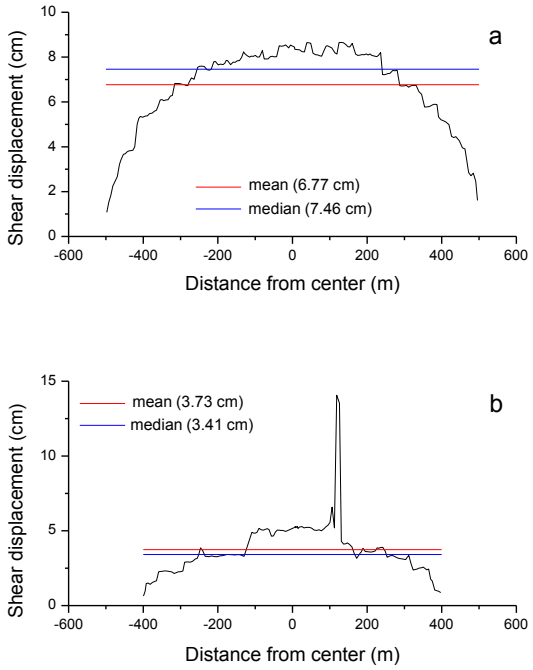


**Figure 10.** Shear displacement profile of (a) an inclined isolated PFC2D fracture (Figure 5a) and (b) an intersected fracture (Fracture #2 in Figure 5c) under shear loading and mean and median values for the representative shear displacements.

## 2.8. The Consultants' assessment

PFC2D can reproduce the parabolic distribution of shear displacement of an isolated fracture along its trace that match the analytical solution in Eq. (1). The parabolic distribution of shear displacement disappears when a fracture is intersected by other fractures. When fractures are intersecting, there are many jumps and drops of the shear displacement along their traces due to the intersections. This behaviour is verified by the modelling results by FRACOD2D, which is a numerical code based on different theory from PFC2D. However, as presented in the previous section, some spikes of the shear displacement plots in the PFC2D modelling cannot be explained by the behaviour of the fracture intersections. The reason for such spikes is investigated and it is found to be due to stress and displacement singularity due to the fact that particles are not allowed to break even under high stress concentrations (no "virtual damage") and that some particles detach from the neighbouring particles ("rattler particles"). Material failure and detachment/fragmentation would probably occur in nature in the rock at such locations with complex fracture settings. This cannot be simulated with PFC2D. Such features are the key factors in generating large displacement spikes at fracture intersections, which can be regarded as a numerical artefact. Although, the Consultants suggest a possible solution that can properly eliminate the numerical artefacts, in this report the Consultants propose that the median displacement is used on the results of fracture displacements containing the spikes. The choice of the median value is expected to filter away the effect of the numerical artefacts arising at the intersections between fractures, and still provide enough conservative estimates of shear displacement, especially for the isolated fractures.

# 3. The Forsmark repository model

## 3.1. Model generation and boundary conditions

The Forsmark repository model is constructed based on the integrated geological model by Stephens et al. (2015). The horizontal section model contains deformation zones and fracture domains at 460 m depth inside the proposed repository volume in the SKB's Local Model Volume. The deformation zones marked in dark red shown in Figure 11a are steeply dipping or vertical and have a trace length at the surface longer than 3000 m. Zones marked in dark green are steeply dipping or vertical and have surface trace length less than 3000 m. Zones marked in light green are gently dipping.

The PFC2D horizontal section model is shown in Figure 11b and contains almost all the deformation zones in the integrated geological model by Stephens et al. (2015), except the light green gently dipping deformation zones ZFMA1, ZFMA2, ZFMB7, ZFMB8 and ZFMF1. Exclusion of these deformation zones is due firstly to the 2D nature of the PFC2D model and, secondly to the fact that the zones are cutting the repository depth far from the planned location of the deposition panels.

Fractures in the repository ("target fractures") are embedded in the models and shown in red in Figure 11b. The repository fractures are stochastically generated in a 3D space within the SKB's Local Model Volume, and then their traces at the depth of the repository (460 m) are determined. The traces of the fractures are extracted from the Discrete Fracture Network (DFN) realisations and embedded in the PFC2D model (see Appendix 2 in Yoon et al., 2014) after converting to a format readable in PFC2D. Black dots in the figure show the heat emitting particles in the PFC2D models that have assigned heat power equivalent to disposed spent fuel canisters.

The maximum horizontal stress (black) and the minimum horizontal stress (red) are shown in Figure 11b by two sets of arrows indicating their orientation. The initial magnitude of the maximum and the minimum horizontal stresses is 40 MPa and 22 MPa, respectively. The model is compressed by controlling the velocity of the particles on the outer layer (light blue region) until the internal stresses match the nominal magnitude of the maximum and minimum horizontal stresses. After this, the movement of the particles on the outer layer is fixed throughout the modelling. The in situ stresses are total stresses and the effect of pore pressure was not taken into account.

The initial temperature field in the vertical section is shown in Figure 11d.

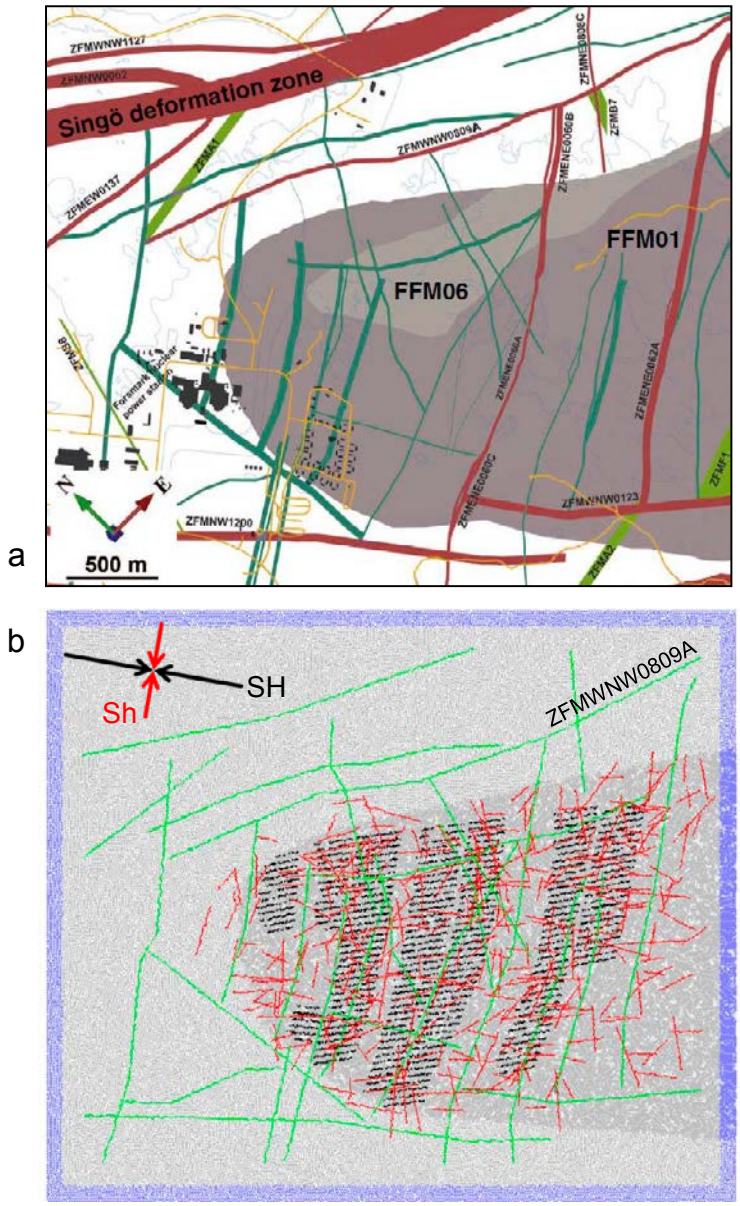


**Figure 11.** (a) Integrated geological model by Stephens et al. (2015), and (b) PFC2D horizontal section model containing the deformation zones (green), the repository target fractures (red) and the heat emitting particles (black dots). ZFMWNW0809A is the deformation zones used for the earthquake modelling in this study. The arrows indicate the orientations of the maximum and the minimum horizontal stresses.

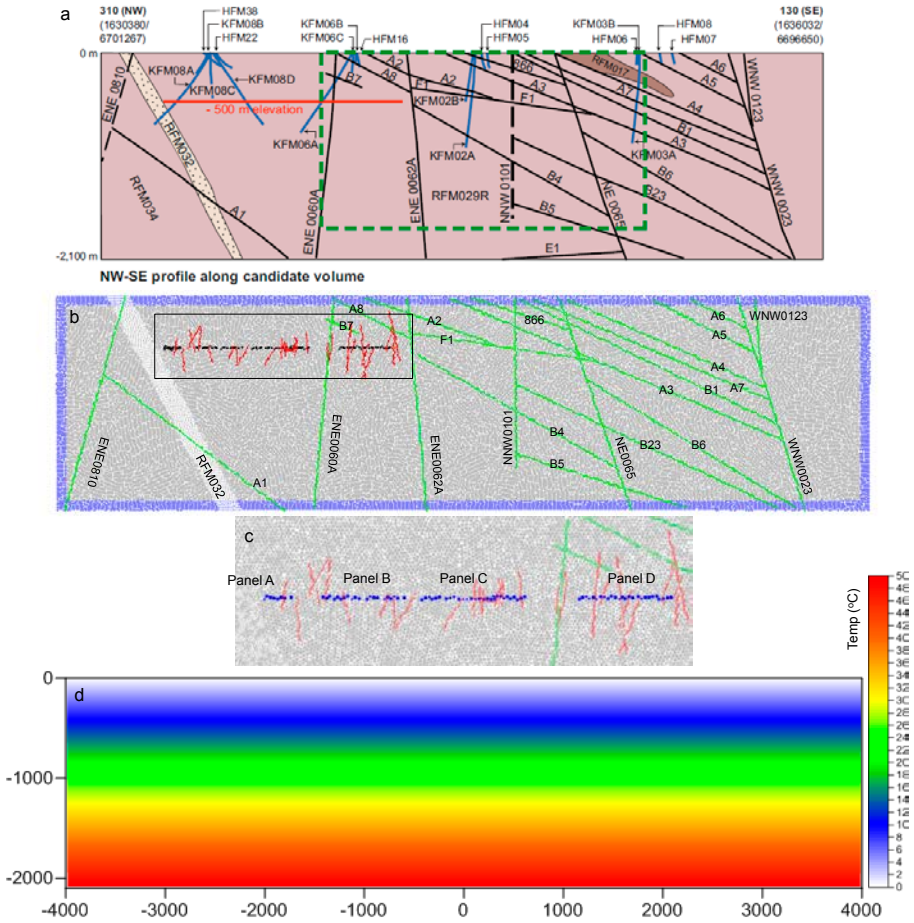


**Figure 12.** (a) NW-SE cross-section through the candidate volume in the structural model (Figure 4-12 in SKB, 2011) showing rock domains and deformation zones, (b) vertical section of the PFC2D model containing deformation zones (green), fractures at the repository depth (red) and the particles representing deposition panels (black dots), (c) enlarged view of the repository area in (a), and (d) initial temperature field with depth.

The PFC2D model of the vertical section is generated based on the section of the integrated geological model on the NW-SE vertical plane through the candidate volume as shown in Figure 12a (SKB, 2011). The PFC2D vertical section model is shown in Figure 12b and contains the deformation zones (green), repository fractures (red) and the particles representing the deposition panels (black dots). As for the horizontal section model, the velocity of the particles on the outer layer (light blue region in Figure 12b) is controlled until the initial stress state at the depth of the repository reaches approximately 40 MPa and 12.5 MPa for the maximum horizontal stress and for the vertical stress, respectively. The velocity of the particles on the outer layer is programmed to change in order to achieve stresses with a depth gradient of 0.078 MPa/m for the maximum horizontal stress and 0.026 MPa/m for the vertical stresses, respectively. The in situ stresses are total stresses and the effect of pore pressure was not taken into account.

After the stresses are applied, a temperature field is assigned with a depth gradient of 23°C/km, computed from the mean in situ temperatures at different depths at Forsmark (Sundberg et al., 2008). Convective heat boundary conditions are assigned to the top outer particle layer in order to simulate heat loss to the atmosphere by forced convection that maintain a temperature of 0°C at the top surface as in SKB's

modelling in Hökmark et al. (2010). As in the horizontal section model, the movement of the outer layer particles is fixed after the present-day initial stresses are applied. However, due to the forced convective heat loss condition assigned to the top layer of the model, where the particle temperature is forced to maintain 0°C by removing the heat, the thermal boundary condition leads to decrease in the size of the particles due to thermal contraction, and consequently has the effect of softening the top boundary.

The parameters used for the Forsmark repository models in for the horizontal and vertical settings are listed in Table 1. For the rock mass, the enhanced parallel bond model (see definition by Itasca, 2012) was used, which allows to input the tensile strength, cohesion and friction angle to the particle contacts where deformations and failure potentially occur without need of heavy calibration campaigns of the bond parameters. For the deformation zones and the repository target fractures, we used the smooth joint model (Mas Ivars et al., 2011).

**Table 1.** Model parameters used for generation of the PFC2D Forsmark repository model.

| Bond model | Property (unit) | Value | Reference |
|---|---|---|---|
| Rock mass (Enhanced parallel bond model) | Particle density (km/m$^3$) | 2700 | Hökmark et al. (2010) |
| | Particle elastic modulus (GPa) | 70 | - |
| | Particle stiffness ratio (-) | 2.5 | - |
| | Particle friction coefficient (-) | 5.0 | - |
| | Parallel bond elastic modulus (GPa) | 70 | - |
| | Parallel bond stiffness ratio (-) | 2.5 | - |
| | Parallel bond tensile strength (MPa) | 2.3 | Glamheden et al. (2007) |
| | Parallel bond cohesion (MPa) | 27 | Glamheden et al. (2007) |
| | Parallel bond friction angle (°) | 50 | Glamheden et al. (2007) |
| | Thermal conductivity (W/mK) | 3.57 | Hökmark et al. (2010) |
| | Thermal expansion coefficient (1/K) | 7.7E-06 | Hökmark et al. (2010) |
| | Specific heat (J/kgK) | 793 | Hökmark et al. (2010) |
| Deformation zones and fractures (Smooth joint model) | Smooth joint normal stiffness (GPa/m) | 60.4 | - |
| | Smooth joint shear stiffness (GPa/m) | 34 | - |
| | Smooth joint friction coefficient (-) | 0.9 | - |
| | Smooth joint tensile strength (MPa) | 0.1 | - |
| | Smooth joint cohesion (MPa) | 0.5 | Hökmark et al. (2010) |
| | Smooth joint friction angle (°) | 35.8 | Hökmark et al. (2010) |
| | Smooth joint dilation angle (°) | 3.2 | Hökmark et al. (2010) |

## 3.2. Heat loading

Due to the 2D nature of the horizontal section models, i.e. no heat dispersion in the out-of-plane direction, adjustment of the heat power output is necessary. It is confirmed by COMSOL modelling (see Appendix D) that using the full canister heat power shown in Figure 13 (black curve) assigned to the 1 m thick insulated panel plane results in extremely high temperatures. Therefore, an assumption is made that about 10% of the total heat energy coming from a full size canister (9034 GJ represented by the area under the black curve in Figure 13) and spreading in a 3D volume goes into the 1 m thick insulated panel. Lowering the curve is done by changing the parameter $t_i$ of the canister power curve as listed in Table 2, which

results in a total heat energy of 1073 GJ (red curve in Figure 13) input in the model with 1 m thickness in the out-of-plane direction.

Another adjustment of the heat power curve is necessary due to the size of the particles in the PFC models. The total number of heat point sources equivalent to spent fuel canisters in the model is 5844, which is obtained by applying the Full Perimeter Intersection Criterion to the DFN03h fracture realization (Yoon et al., 2014). However, due to larger size of the particles in the PFC2D model compared to the size of the deposition holes in the repository, a scaling factor is introduced based on the particle size where the heat source is applied. Table 3 lists the scaling factors applied to the heat emitting particles in each panel of the repository. The scaling factors are applied to the modified heat power curve in Figure 13 (red curve) which is assigned to the heat emitting particles (black dots in Figure 11b).

For the PFC2D vertical section model, the original heat power curve (black curve in Figure 13) is applied to the particles that are grouped into individual panels (blue dots in Figure 12c). The following equation for the heat power is assigned to the grouped particles representing the panels, assuming line heat source similar to that of Probert and Claesson (1997):

$$q(t) = 1700 \sum_{i=1}^{7} a_i \exp(-\frac{t}{t_i}) / px \qquad \text{Eq. (2)}$$

where $px$ is the distance between deposition tunnels (40 m). Coefficients $a_i$ and $t_i$ from Hökmark et al. (2009) are listed in Table 2.

Figures 14 and 15 show the heat power curves applied to the heat emitting particles for the simultaneous and sequential heating of the panels for the horizontal and the vertical section models, respectively. Different starting times of the curves for the cases of sequential heating are due to the fact that the time taken to complete the deposition of the canisters in each panel is taken into account. It is assumed that it takes about 3 days to place one canister in a deposition hole. Therefore, for example, the heat curve for the Panel A in the horizontal section model (black curve in Figure 14b) starts at 2.5 years, because it takes 2.54 years to place 310 canisters (310 canisters × 3 days/canister × 1 year / 365 days = 2.54 years). And the heat release from the canisters is designed to start after all 310 canisters have been placed at the deposition locations.

**Table 2.** Parameters used for the heat power curves in the PFC2D horizontal section model.

| $i$ | $a_i$ (-) | $t_i$ (years) in Hökmark et al. (2009) | $t_i$ (years) in PFC2D |
|---|---|---|---|
| 1 | 0.060147 | 20 | 20 |
| 2 | 0.705024 | 50 | 20 |
| 3 | -0.054753 | 200 | 20 |
| 4 | 0.249767 | 500 | 20 |
| 5 | 0.025408 | 2000 | 20 |
| 6 | -0.009227 | 5000 | 20 |
| 7 | 0.023877 | 20000 | 20 |

**Table 3.** Scaling factors used for the heat power curves in the PFC2D horizontal section model.

| | | Panel A | Panel B | Panel C | Panel D |
|---|---|---|---|---|---|
| Total number of heat sources | DFN03h | 310 | 1456 | 2263 | 1815 |
| | PFC2D | 235 | 1143 | 1746 | 1412 |
| Total area of heat source ($m^2$) | DFN03h[1)] | 7.46e2 | 3.50e3 | 5.44e3 | 4.37e3 |
| | PFC2D[2)] | 2.07e4 | 1.01e5 | 1.54e5 | 1.24e5 |
| Scale factor[3)] | | 0.036 | 0.036 | 0.036 | 0.036 |

1) Area of deposition hole is 2.40 $m^2$.

2) Area of particle heat source in the PFC2D model is 86.5 $m^2$.

3) Scale factor = total area of heat source in the repository layout with DFN03h / total area of heat source in the PFC2D model.

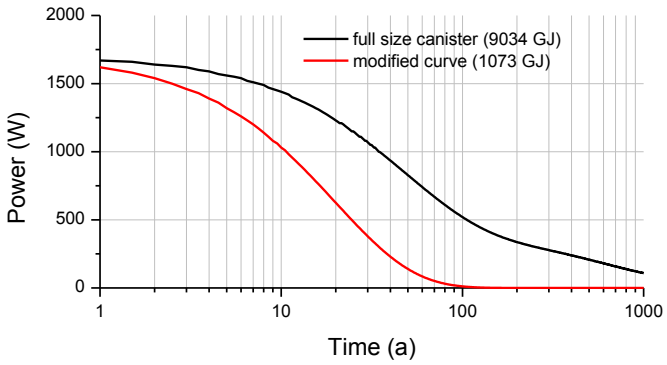


**Figure 13.** Power curve with modified $t_i$ parameters (red) and the original power curve of full size canister (black) for the PFC2D modelling of the horizontal section.

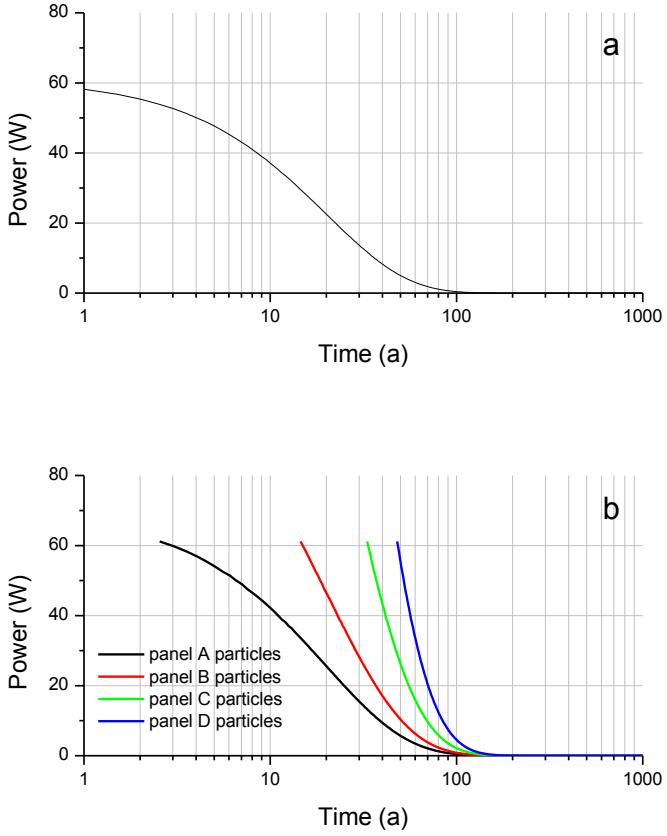


**Figure 14.** Power curves applied to the heat particles for (a) simultaneous heating and (b) sequential heating of the panels for the PFC2D horizontal section model.

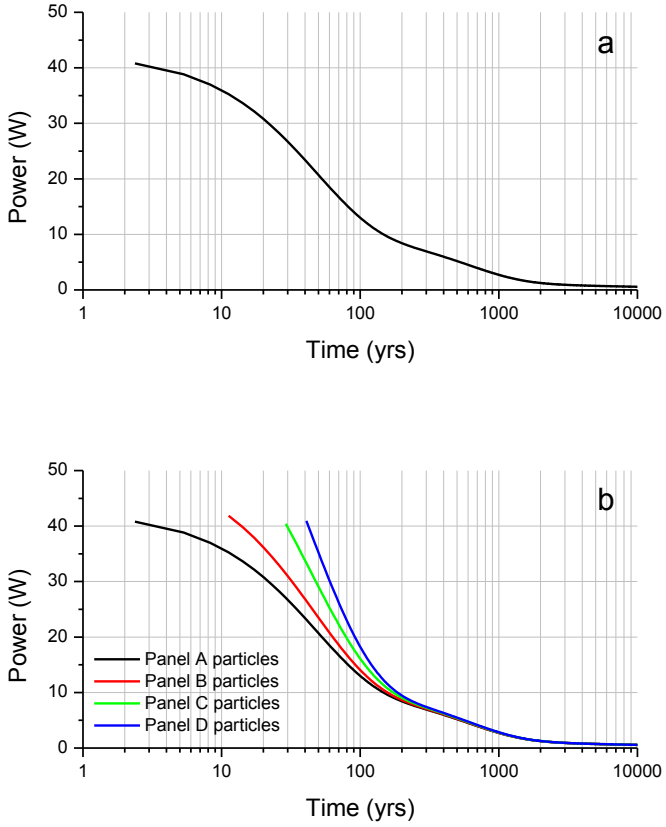


**Figure 15.** Power curves applied to the heat particles for (a) simultaneous heating and (b) sequential heating of the panels in the PFC2D vertical section model.

Several particles are selected in the horizontal section model to monitor the temporal evolution of the temperature and the thermal stresses as shown in Figure 16a. Four particles, #1 to #4, are located at the centre of the panels and other four particles, #5 to #8, are located outside the panel areas. These monitoring particles (Figure 16b) are selected to compare the temperature evolution as a function of time simulated in the PFC2D model with SKB's results from 3DEC models (Hökmark et al. 2010). However, the locations of particle #1 and #3 do not exactly match with the locations of Scanline C and Scanline A in SKB's 3DEC model shown in Figure 16b due to unknown exact coordinates of the scanlines in SKB's model.

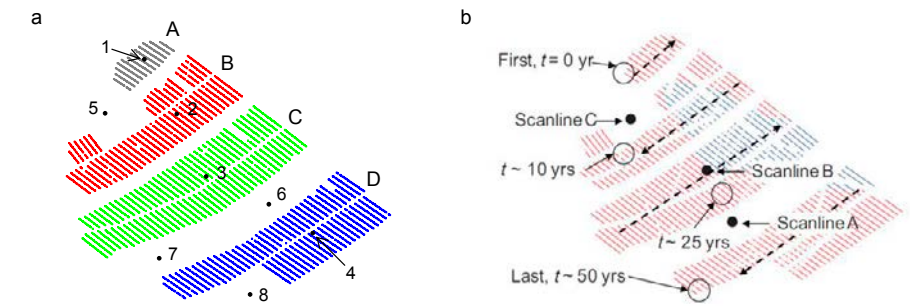


**Figure 16.** Particles selected for monitoring the evolution of temperature and thermal stress (#1 - #4: at the panel area centres, #5 - #8: outside the panel areas) and the locations of the scanlines in SKB's 3DEC model (Hökmark et al. 2010).

## 3.3. Earthquake loading

An earthquake at a specific deformation zone is simulated by releasing the stored strain energy under a given stress condition at the smooth joint contacts forming the activated deformation zone. In order to accumulate strain energy and store it along the trace of a deformation zone, the bond strength of the smooth joint contacts at the earthquake hosting deformation zone is multiplied by a factor of 1000. This allows deformation at the smooth joints contacts, but failure of the smooth joint is not allowed. Thereafter the model is compressed until the internal stresses reach the target present-day principal stresses (in Table 4, SH and Sh for the horizontal section model, and SH and Sv for the vertical section model). Here, we used the total stress and did not include 5 MPa pore fluid pressure at the depth of the repository. Deformation and failure of other smooth joints in the model are allowed during the whole calculation. Two deformation zones are selected for the earthquake modelling, one in the horizontal and one in the vertical section models. These are ZFMWNW0809A and ZFMA3 as indicated red in Figure 17.

**Table 4.** Absolute stress components as the present-day initial stress fields for the PFC2D horizontal and the vertical section models.

| Model | Stress components (MPa) | | | Remark and reference |
|---|---|---|---|---|
| | SH | Sh | Sv | |
| Horizontal | 40 | 22 | - | Most likely stress field (Martin, 2007) |
| Vertical | 40 | - | 12.5 | At the repository depth of 460 m, Reverse stress field (Fälth et al., 2010) |

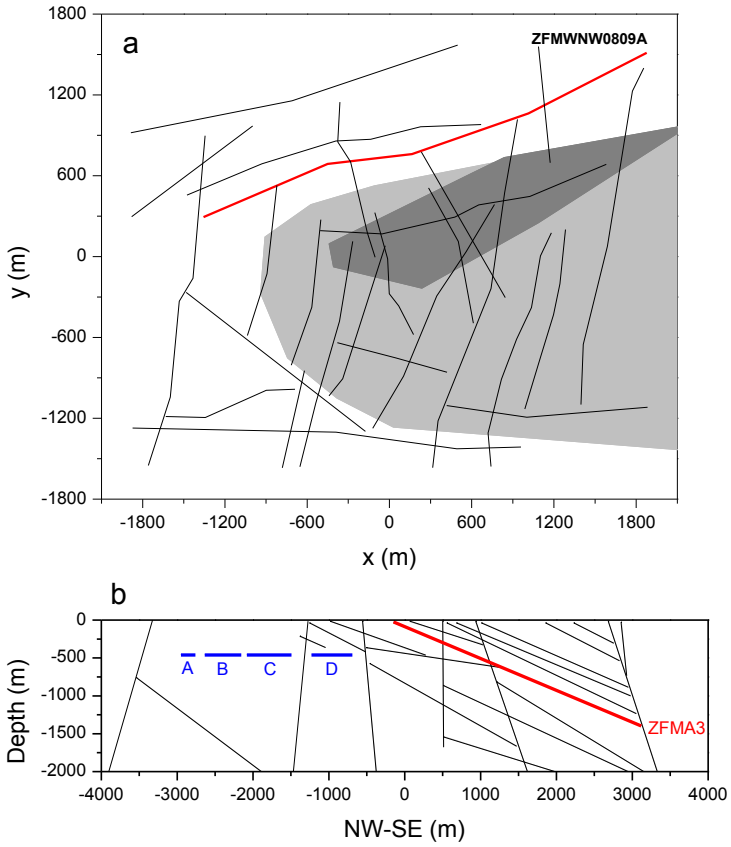


**Figure 17.** Deformation zones selected for the earthquake modelling (red) in the PFC2D (a) horizontal and (b) vertical section models.

The release of the accumulated strain energy in the earthquake hosting deformation zone is simulated by lowering the bond strength of the smooth joint contacts with a multiplication factor $10^{-20}$ for the tensile and cohesion strength of the smooth joints. In addition to this, friction and dilation angles of the smooth joints are lowered to 10% of their original values, i.e. from 35° to 3.5°. Such measure was taken to mimic a rupturing process and the strain energy release when the fracture asperities are lost due to the earthquake slip. Lowering of the joint normal and shear stiffness was not considered because of the minimal impact on the rupturing process. This is suggested as further study as it is expected to have influence on the post-earthquake behaviour. Upon releasing the strain energy, a seismic wave is generated at the activated deformation zone and propagates through the model. Models are given a few seconds to respond to the seismic wave.

The seismic moment magnitudes $M_0$/m of the simulated earthquakes correspond to the seismic energy released at the earthquake hosting deformation zones with 1 m thickness in the out-of-plane direction. Therefore, the seismic moment refers to a 1 m thick slice of the real deformation zones. In order to take into account of the seismic energy from a full size deformation zone, it is assumed that real deformation zones have a width equal to their length, therefore the Rupture Area (RA) = length × width = length$^2$. The ratio of 1:1 between the rupture length and the rupture width is

a conservative assumption but also reasonable as seen in Figure 18 from the rupture length vs. rupture width relation for tectonic earthquakes on natural faults from different sources in the literature. The simulated seismic moment $M_0$/m is then multiplied by the length to take into account of the seismic moment resulting from activation of the full size fault surface. The seismic moments ($M_0$) that correspond to the full size deformation zones are then converted to moment magnitudes ($M_w$) using the equation by Hanks and Kanamori (1979):

$$M_w = {}^{2}/_{3} \log M_0 - 6 \qquad \text{Eq. (3)}$$

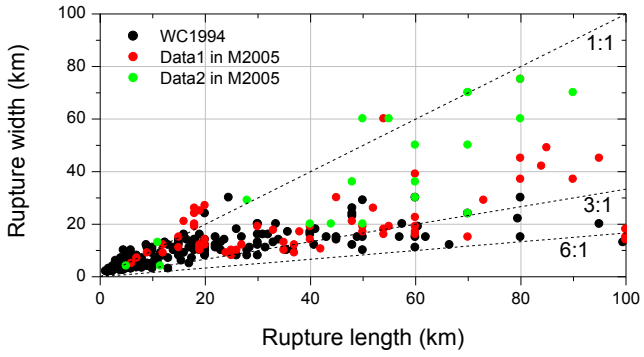


**Figure 18.** Rupture length vs. rupture width relation of the natural tectonic earthquake faults (WC1994: Wells and Coppersmith, 1994); Data1 in M2005: 2D earthquake slip inversion models in Manighetti et al.,2005; Data2 in M2005: Teleseismic earthquake slip models in Manighetti et al., 2005).

## 3.4. Modelling cases

Table 5 lists the modelling cases covered in this study. Descriptions of the key features of the models are provided at the bottom of the table.

**Table 5.** Modelling cases performed in this study.

| Loading[1)] Model type[2)] | Heating[3)]; | Stress[4)]; | DFN[5)]; | $DZ_{EQ}$; | $t_{EQ}$[6)] | Chapter |
|---|---|---|---|---|---|---|
| T (H) | Sim | Mls | DFN03h | | | 4 |
| | Seq | Mls | DFN03h | | | 4 |
| T (V) | Sim | Rsf | DFN06v | | | 5 |
| | Seq | Rsf | DFN06v | | | 5 |
| T+EQ (H) | Sim | Mls | DFN03h | ZFMWNW0809A | 100 yrs | 6 |
| T+EQ (V) | Sim | Rsf | DFN06v | ZFMA3 | 100 yrs | 6 |

1) Loading conditions
   - ✓ T: Thermal induced
   - ✓ T+EQ: Thermal and earthquake induced

2) Model types
   - ✓ H: Horizontal section model (Figure 11b)
   - ✓ V: Vertical section model (Figure 12b)

3) Heating
   - ✓ Sim: All panels are heated simultaneously
   - ✓ Seq: Panels are heated in sequence, A→B→C→D

4) Present-day initial stress fields
   - ✓ Mls: Most likely stress (SH vs. Sh in Table 4)
   - ✓ Rsf: Reverse stress field (SH vs. Sv in Table 4)

5) Discrete Fracture Network (DFN)
   - ✓ DFN03h: the most conservative realization for the horizontal model (Figure 11b)
   - ✓ DFN06v: the most conservative realization for the vertical model (Figure 12b)

6) Time of occurrence of the earthquake after completion of deposition.

# 4. Modelling of heat induced seismicity and fracture shear – horizontal section model

## 4.1. Temperature distribution

The distribution of rock temperature increase at several selected times resulting from simultaneous heating of the panels in the horizontal section model is shown in Figure 19. Panel A undergoes a maximum temperature increase at 50 years. The maximum temperature increase appears approximately 100 years after the start of the heating for Panels B, C and D. The temperature increase in Panel C lasts longer than in other panels as it contains the largest number of heat emitting particles (1746, see Table 3).

Figure 20 shows the temporal changes of the rock temperature increase monitored at several selected particles in the model as illustrated in Figure 16a. Particle #1 and Particle #4 show larger rates of temperature decay compared to that of Particle #2 and Particle #3. This is due to the fact that Panel A contains the smallest number of canisters and Panel D is distant from Panel C, which leads to less heat conduction from Panel C to D. Unlike the temperature increase monitored at the centre of the panel areas, Figure 20b shows a continuous increase of the rock temperature at the points at a distance of about 100 m outside the panel areas (Particle #6 and #7) until 1,000 years, after that a decrease of the rock temperature. The calculations were time consuming and it was decided to stop at 3,000 years when the curves in Figure 20 showed clear signs of temperature decrease after the peak temperature.

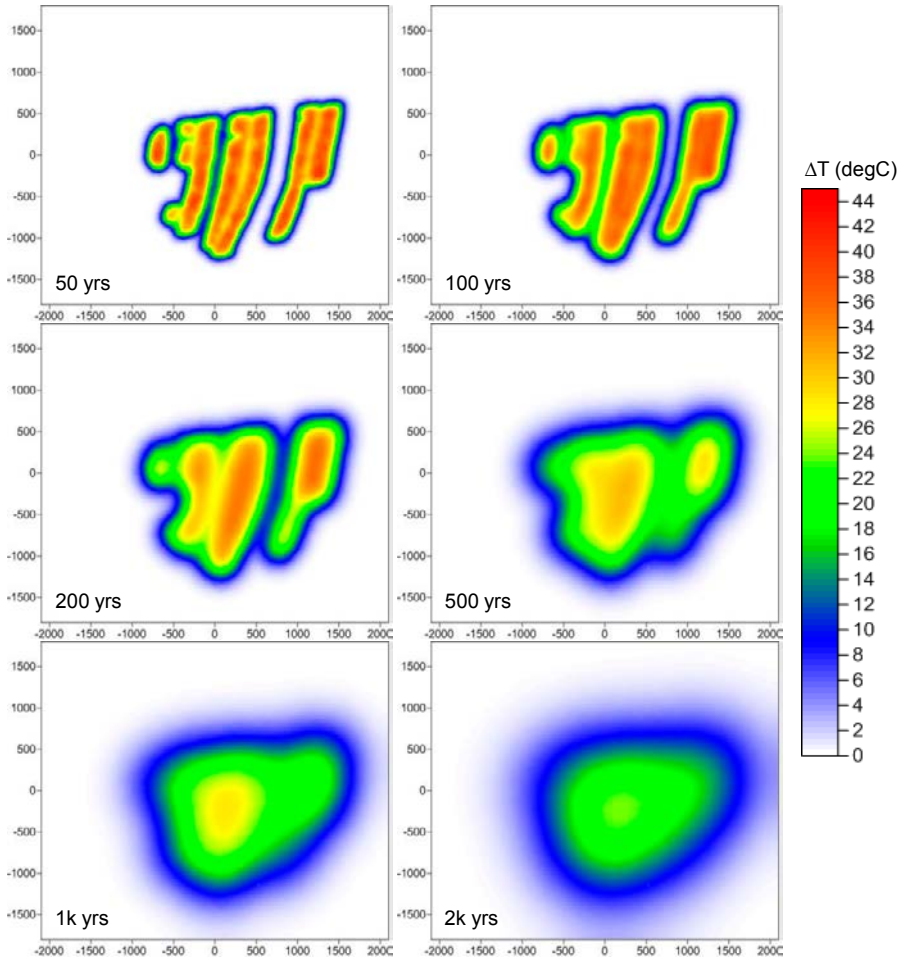


**Figure 19.** Distribution of the rock temperature increase at several selected times resulting from simultaneous heating of all panels in the PFC2D horizontal section model.

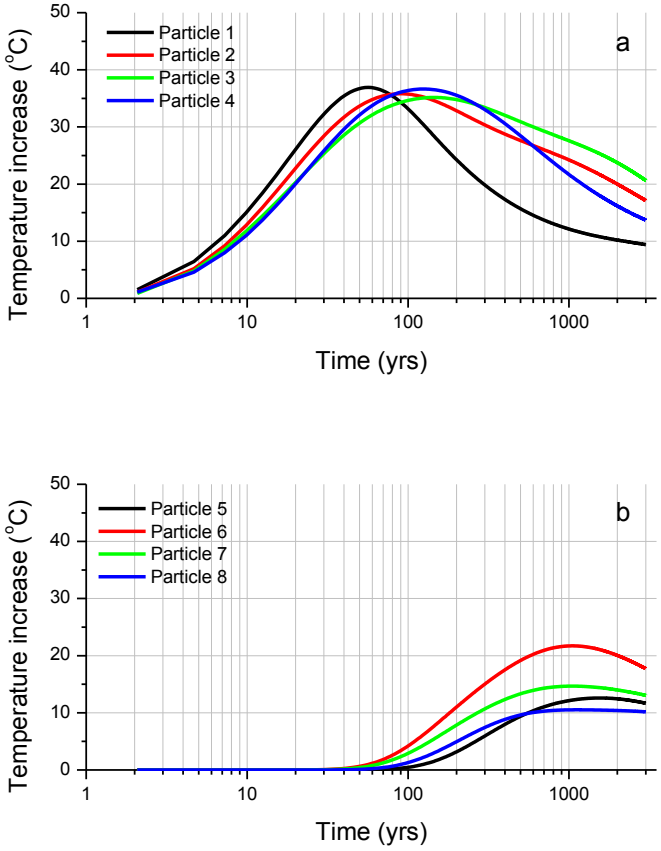


**Figure 20.** Temporal changes of the rock temperature increase monitored at several selected particles (Figure 16a, Particles #1 to #4: at the centre of panel areas, Particles #5 to #8: outside the panel areas) resulting from simultaneous heating of all panels in the PFC2D horizontal section model.

Distribution of rock temperature increase at several selected times from sequential heating of the panels is shown in Figure 21. Figure 22 shows the temporal changes of the rock temperature increase monitored at several selected particles in the PFC2D horizontal section model. The temperature increase in Panel A is the highest at 50 years. However, the peak of the temperature increase at the centre of Panels B, C and D appear approximately 100 years after start of the heating. Same as in the simultaneous heating, the model was run up to 3,000 years and Figure 22b shows that the temperature increases at the particles outside the panel areas (Particles #6 and #7) hit the peak temperature at 1,000 years and then decreases.

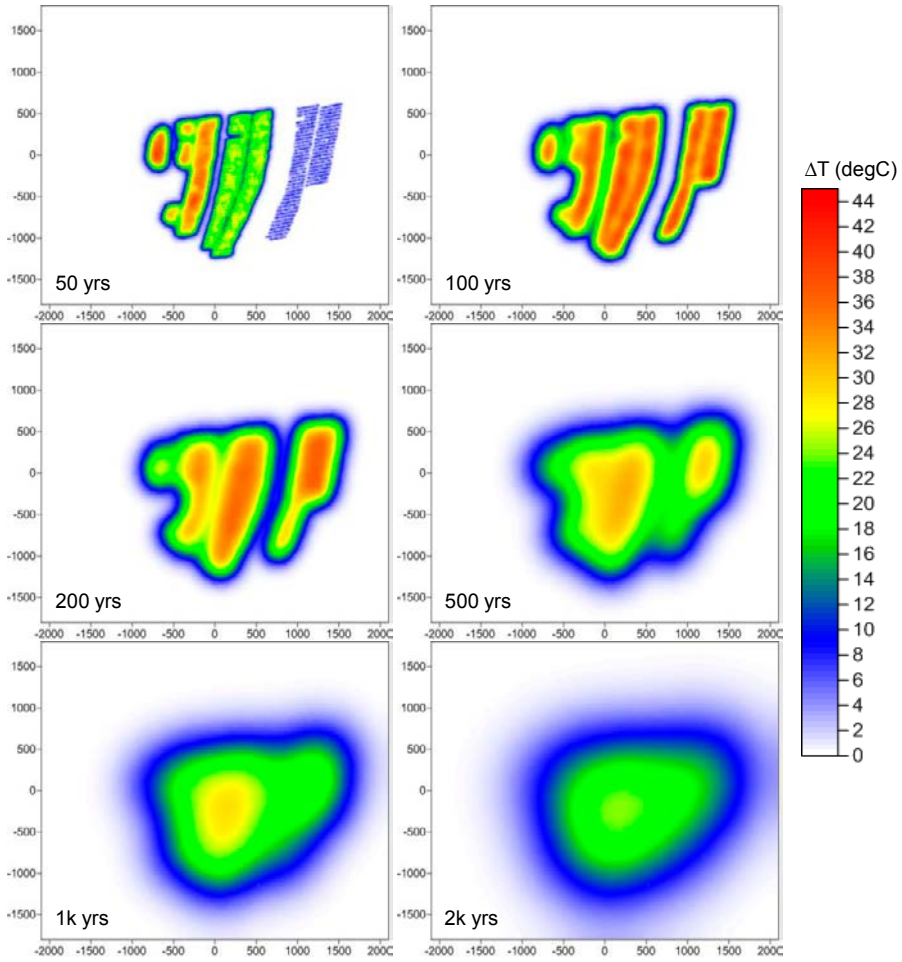


**Figure 21.** Distribution of the rock temperature increase at several selected times resulting from sequential heating of the panels in the PFC2D horizontal section model.

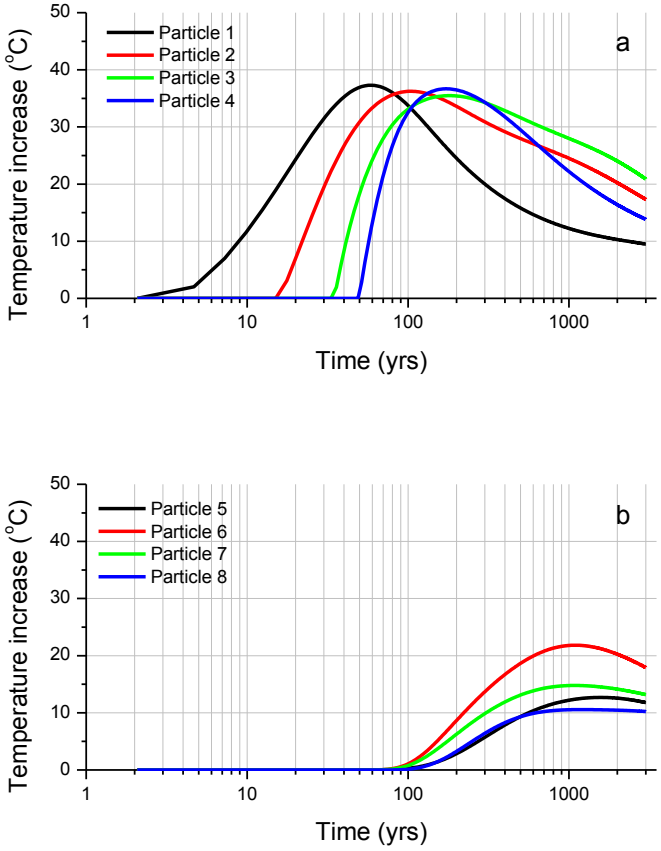


**Figure 22.** Temporal changes of rock temperature increase monitored at several selected points (Figure 15a, Particles #1 to #4: at the centre of panel areas, Particles #5 to #8: outside the panel areas) resulting from sequential heating of panels in the PFC2D horizontal section model.

## 4.2. Thermally induced stresses

Thermally induced stresses are monitored at the selected particles (Figure 16a). Figure 23 shows temporal changes of the stresses resulting from simultaneous heating in the direction of the major ($\sigma_1$) and minor ($\sigma_2$) initial principal stresses. The maximum change in $\sigma_1$ is about 60 MPa and takes place at the centre of Panel D (Figure 23a, Particle 4). The maximum change in $\sigma_2$ at the panel centre is about 40 MPa and occurs in Panel B (Figure 23c, Particle 2). The largest change in $\sigma_1$ outside the panels takes place at Particle #7 and is about 45 MPa, which is between Panel C and D (Figure 23b). The changes in the $\sigma_2$ outside the panels are below 20 MPa (Figure 23d).

The temporal evolution of the thermal stresses from the sequential heating (Figure 23) is similar to that resulting from the simultaneous heating and reach a peak between 50 and 200 years for the particles at the centre of the panels.

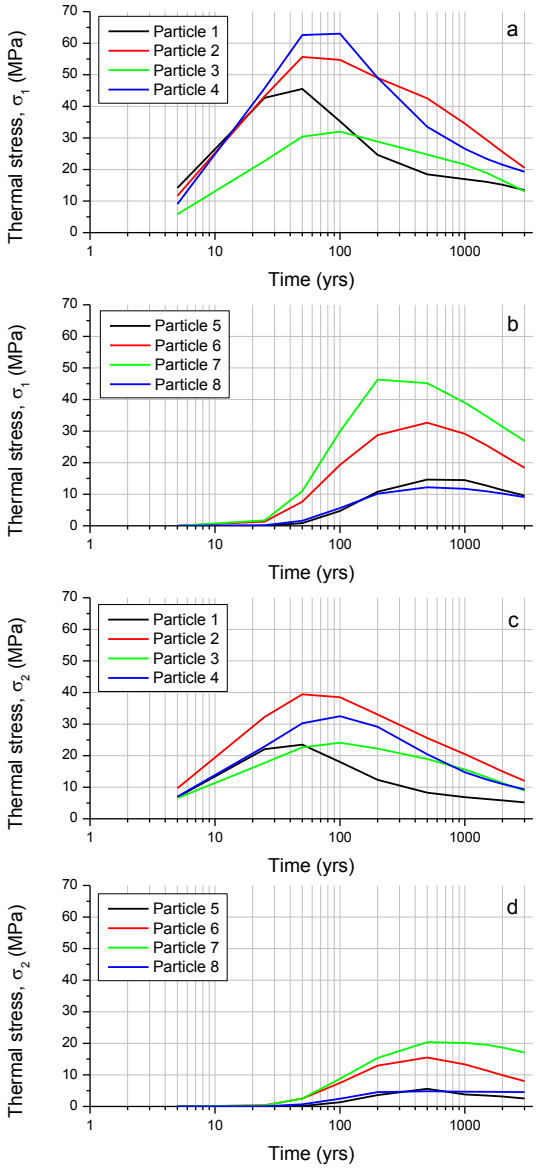


**Figure 23.** Temporal evolution of thermally induced major principal stress (σ1) (a) at the panel centres (Particles #1 to #4), (b) outside the panels (Particles #5 to #8), and minor principal stresses (σ2) (c) at the panel centres (Particles #1 to #4), (d) outside the panels (Particles #5 to #8), resulting from simultaneous heating of all panels in the PFC2D horizontal section model.

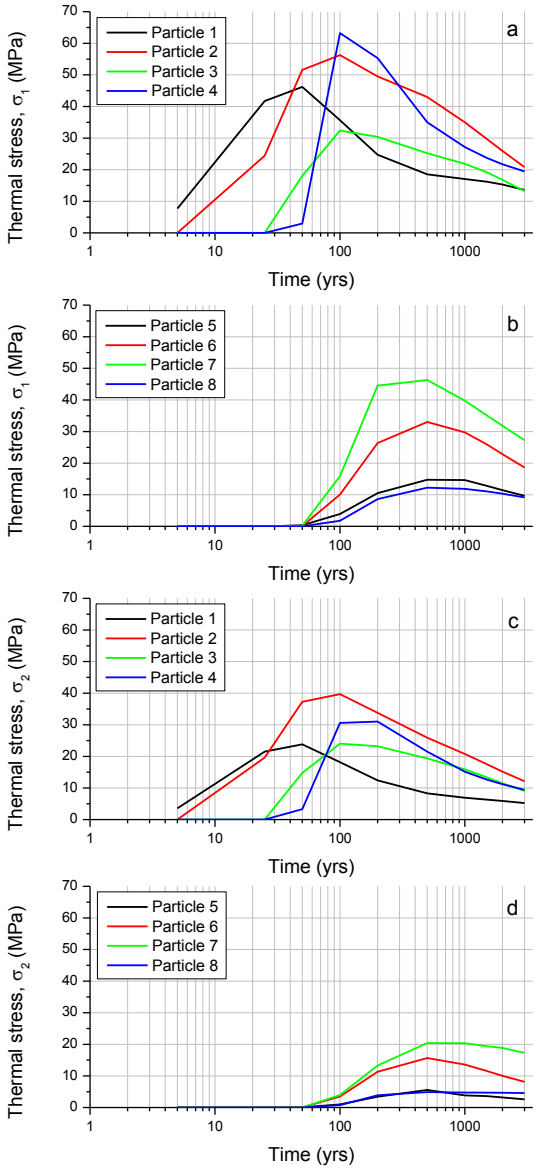


**Figure 24.** Temporal evolution of thermally induced major principal stress (σ1) (a) at the panel centres (Particles #1 to #4), (b) outside the panels (Particles #5 to #8), and minor principal stresses (σ2) (c) at the panel centres (Particles #1 to #4), (d) outside the panels (Particles #5 to #8), resulting from sequential heating of the panels in the PFC2D horizontal section model.

## 4.3. Induced seismicity

The heat emitted from the canisters results in thermally induced stress changes as shown in Figures 23 and 24 and consequently causes slip of the pre-existing fractures and failure of the rock mass. Figure 25 shows the distribution of thermally induced seismic events accumulated over (a) 100 years and (b) at 1,000 years after start of simultaneous heating of the repository panels. Figure 26 shows the results for the sequential heating.

Figures 25 and 26 contain information on the induced seismic event magnitudes. Seismic moment $M_0$/m due to the slip of the smooth joint is calculated using the following equation:

$$M_0 = GAd \qquad \text{Eq. (4)}$$

where $G$ is the shear modulus (30 GPa), $A$ is the smooth joint area ($m^2$, smooth joint length ×1 m thickness in the out-of-plane direction), and $d$ is the shear displacement (m). The moment magnitude $M_w$ is then computed using Eq. (3).

The distributions of the seismic events that accumulated over 100 year after the start of heating (Figure 25a for the simultaneous and Figure 26a for the sequential heating) demonstrate that the magnitudes of the seismicity is mostly below $M_w$1.1 and distributed within the footprint of the panels. However, the distribution of the seismic events evolves with time and tends to cluster at the area of high fracture density and at the areas where the fractures are intersecting one another and with the deformation zones.

Seismicity clusters tend to migrate away from the panel areas over time as shown in Figure 25b and Figure 26b for the simultaneous and sequential heating, respectively. The magnitudes observed at 1,000 year are mostly below $M_w$2.2 for the simultaneous and sequential heating.

The results should be interpreted with caution, because some of the large displacements of the smooth joints at the intersections can be numerical artefacts as discussed in Section 2.6. If the stress concentrated at the intersections is high enough to induce failure of the rock mass in the neighbouring areas, this can lead not a single large seismic event but to multiple events distributed over an area with magnitudes lower than the single large event could have.

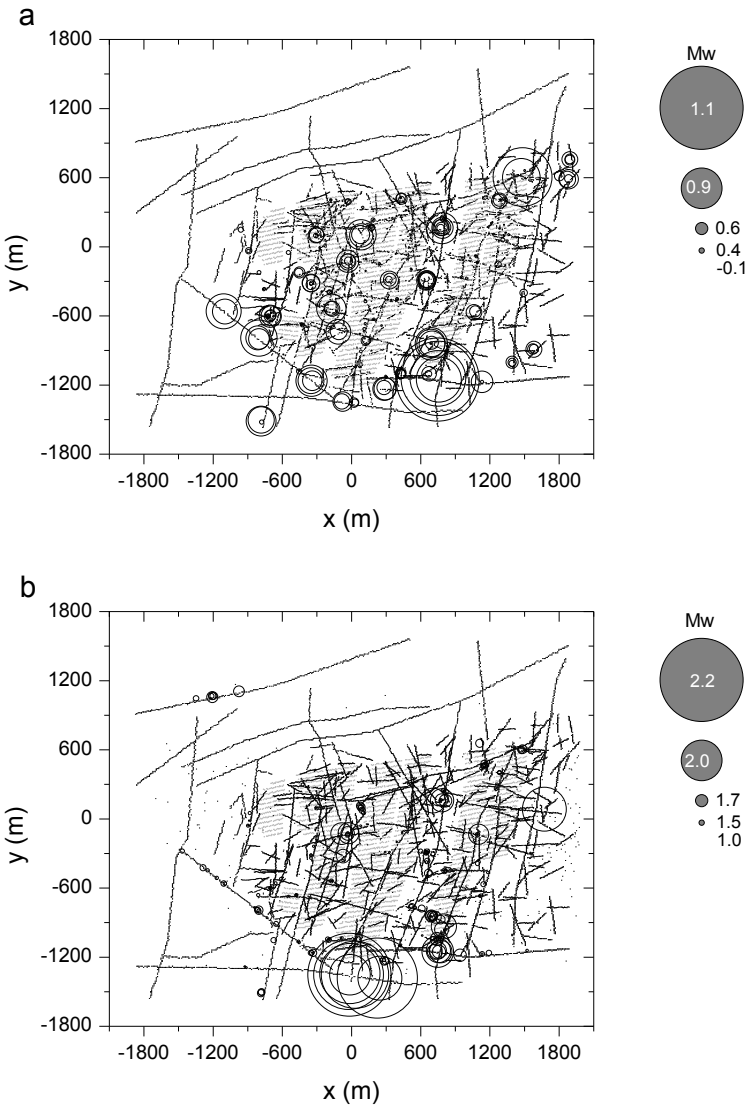


**Figure 25.** Distribution of the thermally induced seismic events accumulated over (a) 100 years and (b) 1,000 years after start of the simultaneous heating of all the panels in the PFC2D horizontal section model with DFN03h realization.

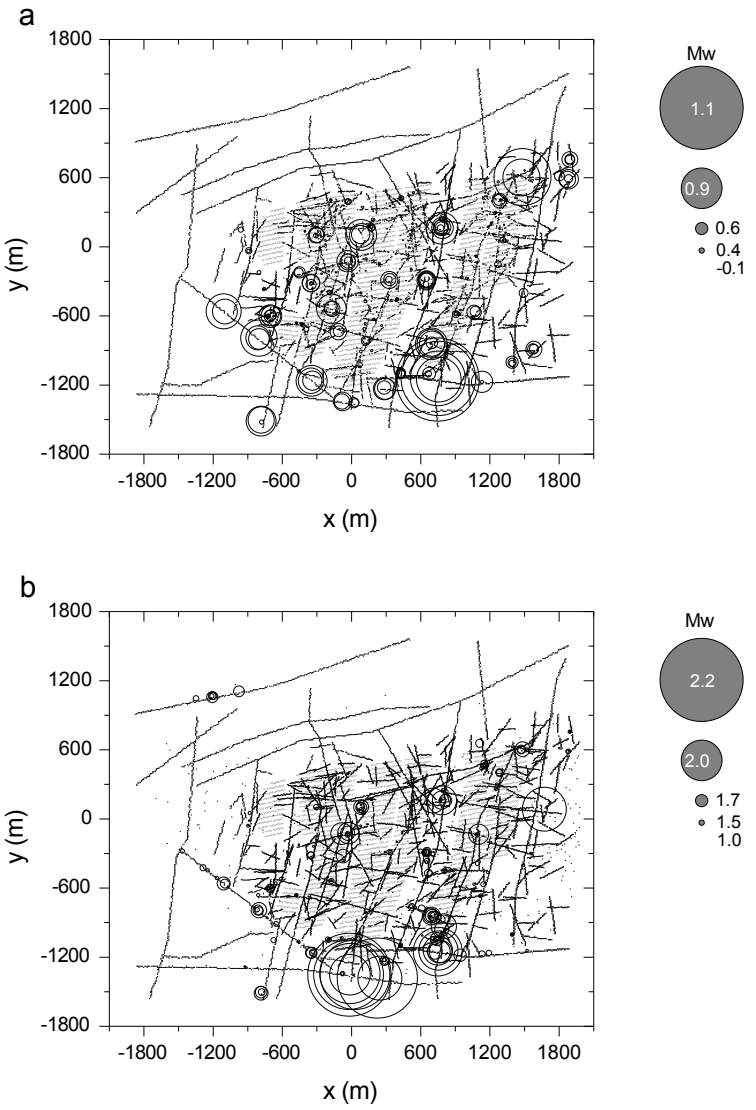


**Figure 26.** Distribution of the thermally induced seismic events accumulated over (a) 100 years and (b) 1,000 years after start of the sequential heating of the panels in the PFC2D horizontal section model with DFN03h realization.

## 4.4. Fracture shear displacements

All the fractures are classified into four classes depending on their length. Fractures in Class 1 have length between 100 m and 150 m. Fractures in Class 2 have length between 150 m to 200 m. Fractures in Class 3 have length between 200 m to 300 m, and the fractures in Class 4 have length between 300 m to 600 m. As discussed in Section 2.7, for each fracture, the median value of shear displacement of the smooth joints constituting a fracture is selected as a representative shear displacement of the fracture in order to avoid the artefact of the spikes in the displacement plots.
Figure 27 and 28 show the shear displacement of all the fractures at different times resulting from the simultaneous and the sequential heating, respectively.

For the simultaneous heating case (Figure 27), the results show that the shear displacements of all the fractures increase significantly during the first 20 to 100 years of repository heating and reach values of about 1,5 mm. After 3,000 years of the repository heating, all the fractures are showing shear displacement below 1 mm.

For the sequential heating case (Figure 28), the distributions of the data sets are very similar to those from the simultaneous heating case. After 3,000 years, all the fractures are showing shear displacement below 1 mm. Moreover, it is noteworthy that the maximum shear displacement of the majority of the fractures takes place at 100 years or 200 years.

Figure 29 shows the temporal changes of the median displacement of the fractures of which the traces are (a) contained within the footprints of the panels and (b) located outside the footprints of the panels. The figure shows that the fractures within the panel footprints undergo shear displacement of relatively large rate until 100 years, whereas those fractures outside the panel footprints show steady increase until about 1,000 years for then stabilize.

Twenty fractures are randomly selected from the sets of the fractures that are within (Figure 29a) and outside the footprints of the panels (Figure 29b) and the evolution of their shear displacements is plotted over time in Figure 30. This figure shows that the shear displacements of the fractures located within the panel footprints increase rapidly during the early time and reach the maximum values approximately at 100 years after the start of the repository heating. The displacements then decrease significantly during the time period between 200 years and 500 years and show steady decrease (Figure 30a). The fractures outside the panel footprints show lower rates of displacement and reach the maximum values approximately at 200 years or even after. The displacements then stay at constant values or increase steadily in the long term (Figure 30b).

Statistical analysis was made to the median shear displacements of all the fractures that are within the panel footprints and outside the panel footprints. Their temporal trends are shown in Figure 30c. The average and the standard deviation of the median values of all fractures are shown.

The fractures within the panel footprints show larger shear displacement in the early time of the repository heating. These displacements reduce with time. The displacement of fractures located outside the footprints of the panel increases with time for the whole period but tend to stabilize in the long term at the level of displacement of the fractures within the panel footprints.

It is observed that the shear displacement of the fractures within the panel footprints decreases but does not recover to the initial low levels. This is due to the dilation occurred during shearing of the fractures.

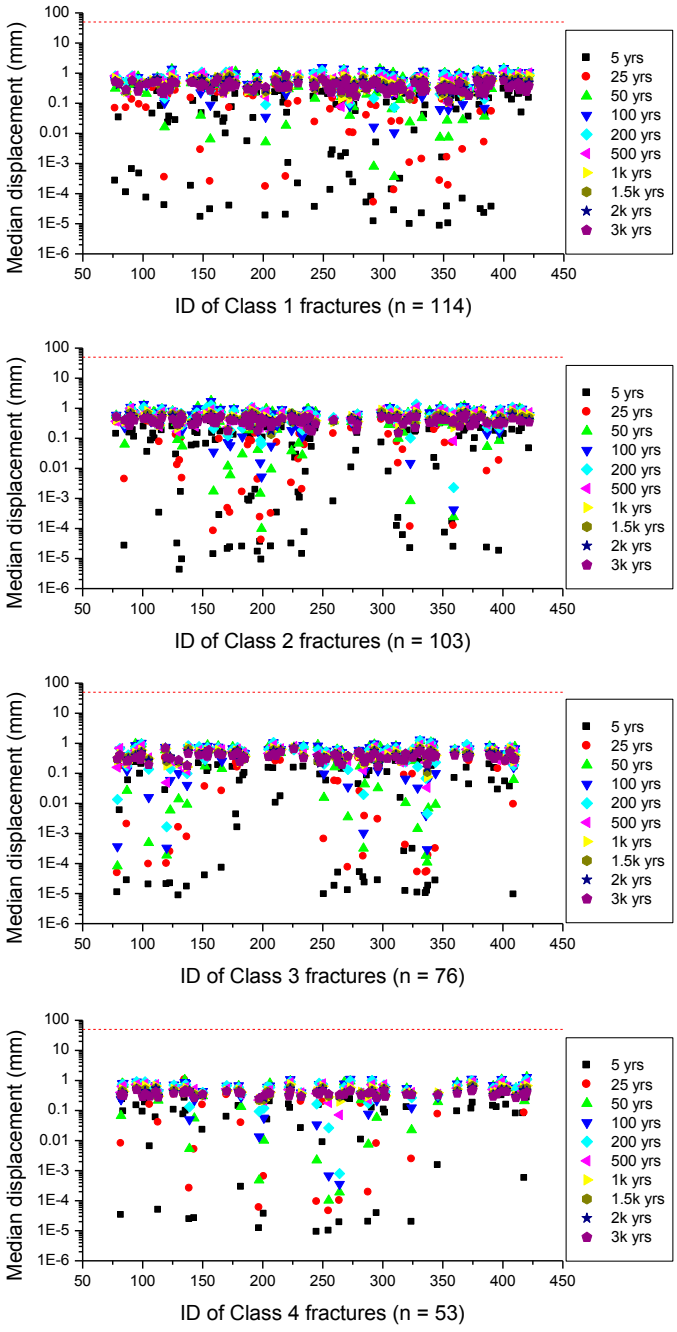


**Figure 27.** Temporal changes of the median shear displacement of the fractures in different length classes resulting from the simultaneous heating of all the panels in the PFC2D horizontal section model with DFN03h realization. The red dashed lines represent the 50 mm canister damage threshold.

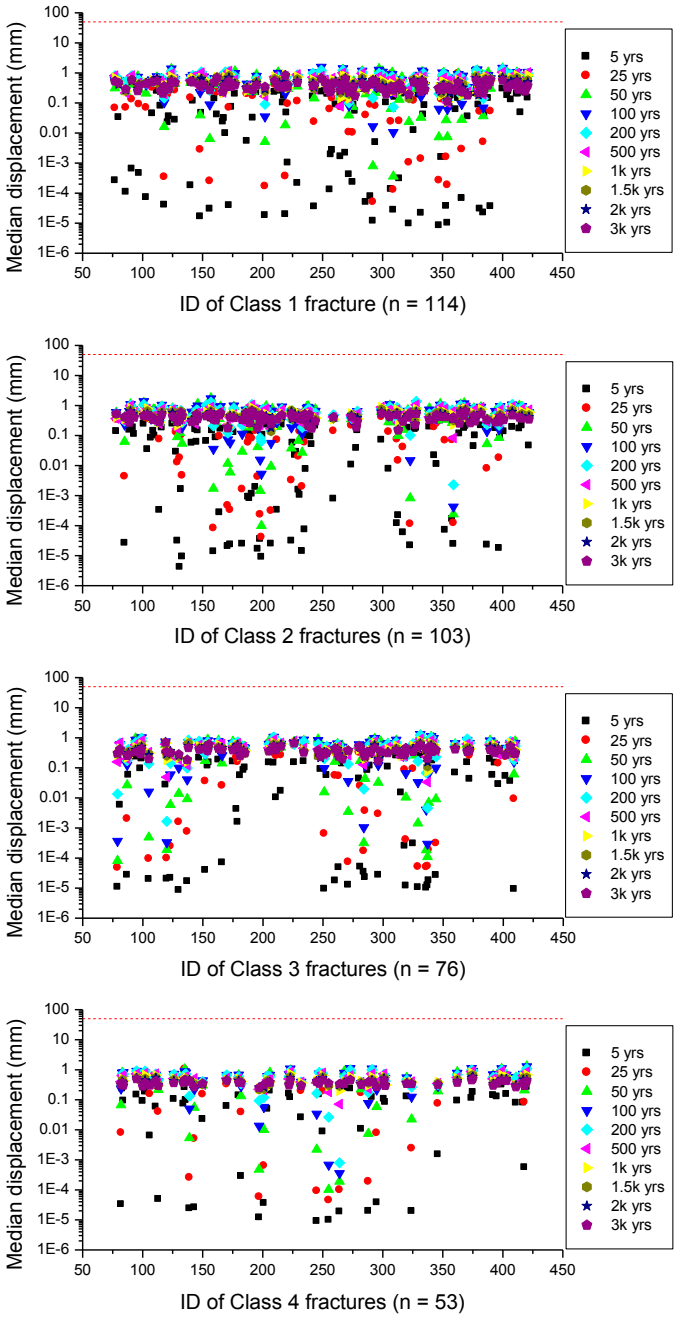


**Figure 28.** Temporal changes of the median shear displacement of the fractures in different length classes resulting from the sequential heating of the panels in the PFC2D horizontal section model with DFN03h realization. The red dashed lines represent the 50 mm canister damage threshold.

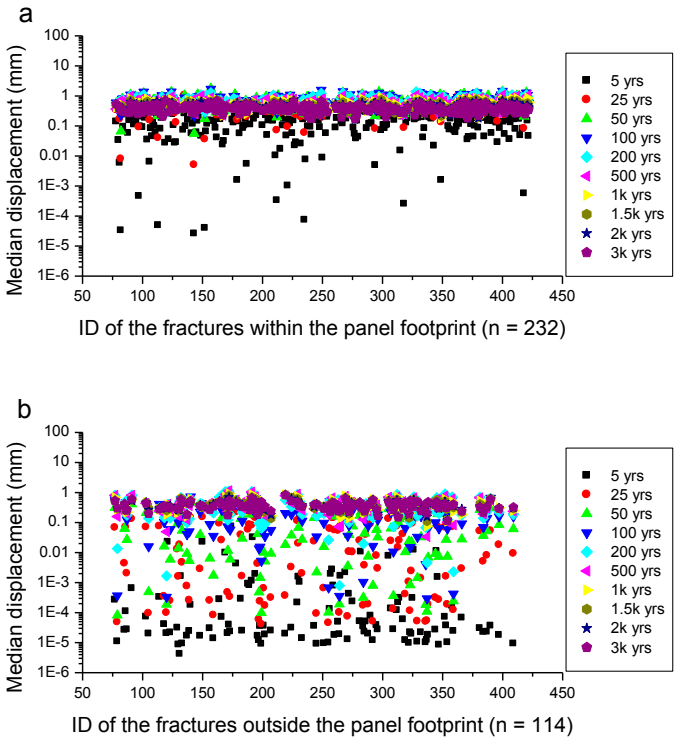


**Figure 29.** Temporal changes of the median shear displacement of the fractures (a) within the footprint of the panels and (b) outside the footprint of the panels resulting from the sequential heating of the panels in the PFC2D horizontal section model with DFN03h realization.

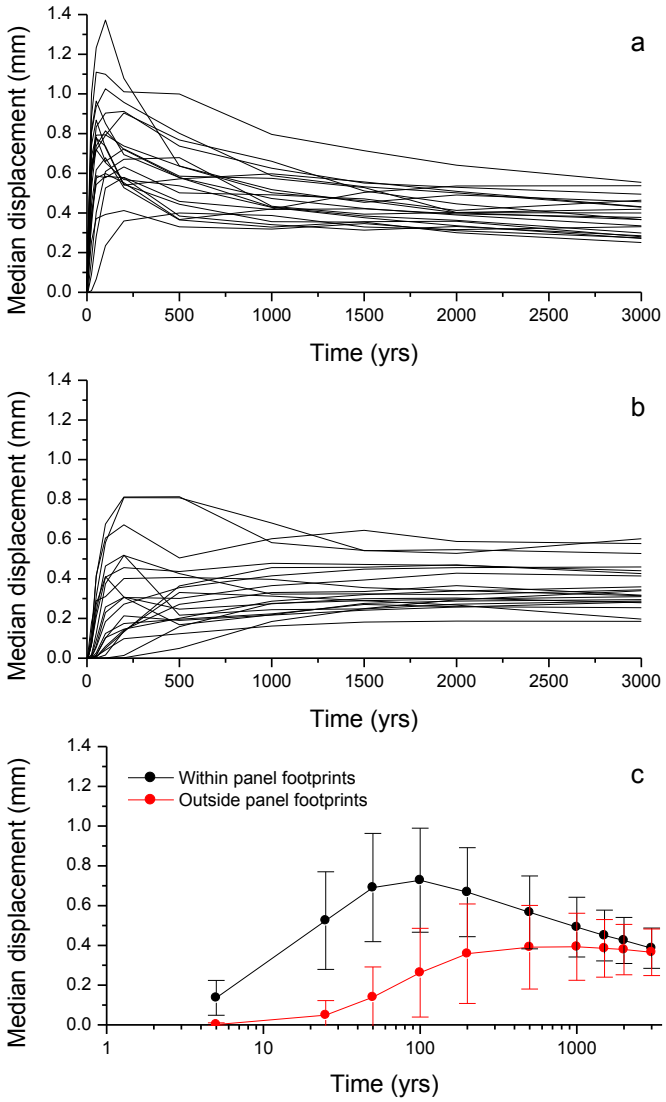


**Figure 30.** Temporal changes of the median shear displacement of twenty randomly chosen fractures (a) within and (b) outside the panel footprints. (c) average and standard deviation of the median displacement of the fractures that are within (black) and outside (red) the panel footprints, resulting from the sequential heating of the panels in the PFC2D horizontal section model.

## 4.5. The Consultants' assessment

Figure 31 compares the distribution of temperature increase at three time steps modelled with 3DEC in Hökmark et al. (2010) and modelled with PFC2D in this study for the simultaneous heating case. In general, the temperature increase distribution shows a good spatial agreement between the two models, except for the area of rock domain RFM045 (fracture domain FFM06, see Figure 11a). In RFM045, the canister spacing is 6.8 m instead of 6 m, as it was adopted in the PFC2D models for simplicity. This contributed to lower the temperature increase in that domain in the 3DEC analysis (personal communication with Mr. Harald Hökmark,

September 14, 2015). In the PFC2D model the same thermal conductivity of 3.57 W/mK was assigned to the RFM045 and RFM029.

Another difference between the two models is three dimensionality of the 3DEC model that can only be approximated by the PFC2D models. This is why relatively lower rock temperature increase is shown by the 3DEC model.

Two areas show strong similarity between the 3DEC and PFC2D results. Panel A and D show temperature increase at 50 years but lower than for the surrounding rock. Comparison of two sets of results demonstrates that the thermal modelling by PFC2D can reproduce qualitatively the results obtained by 3DEC modelling. The highest temperature shown in the 3DEC model is 28 °C, whereas it is 44 °C in the PFC2D model. This is also due to the fact that the contours used in visualization of the 3DEC results are based on a grid that is too coarse to capture the details around the rows of canisters and underestimate the real maximum temperature increases in the repository, which are around 50°C after 50 years and 35°C after 200 years (Hökmark et al., 2010). In the PFC2D modelling, however, despite the difference in size of the heat emitting particles and the canisters (see Table 2), the particles size is less coarse than the grid in the 3DEC model. This enables quantitatively closer match between the simulated temperature increase, e.g. 44°C (PFC2D) and 50°C at 50 years (real maximum, Hökmark et al., 2010).

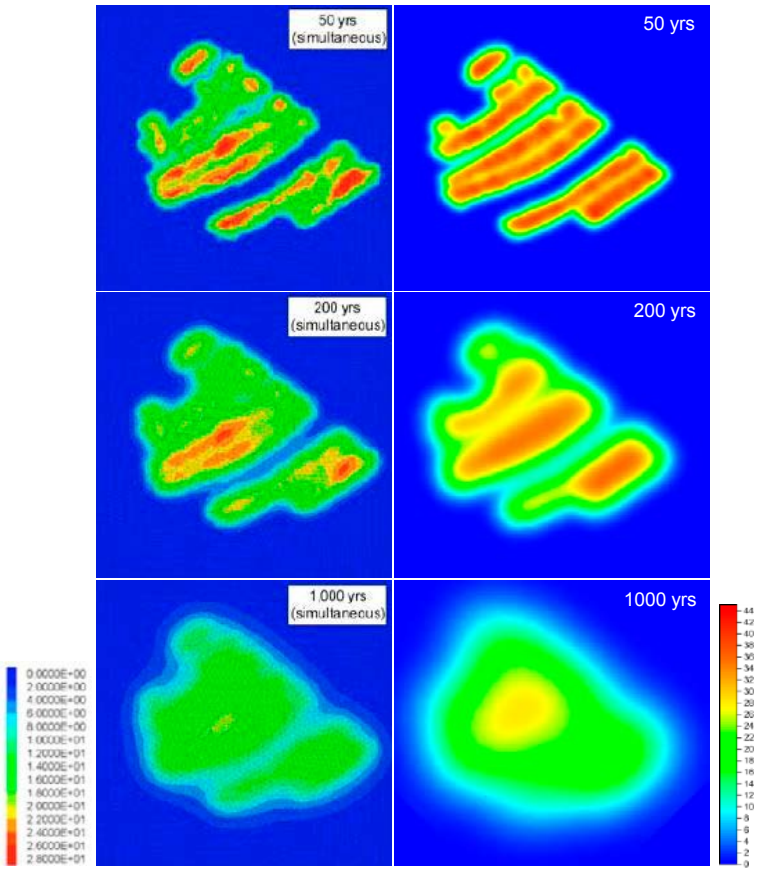


**Figure 31.** (Left column) Contour plots of the rock temperature increase at the repository level at Forsmark obtained in 3DEC modelling in Hökmark et al. (2010) and (right column) distribution of temperature increase modelled in the PFC2D horizontal section model both with simultaneous heating of the panels.

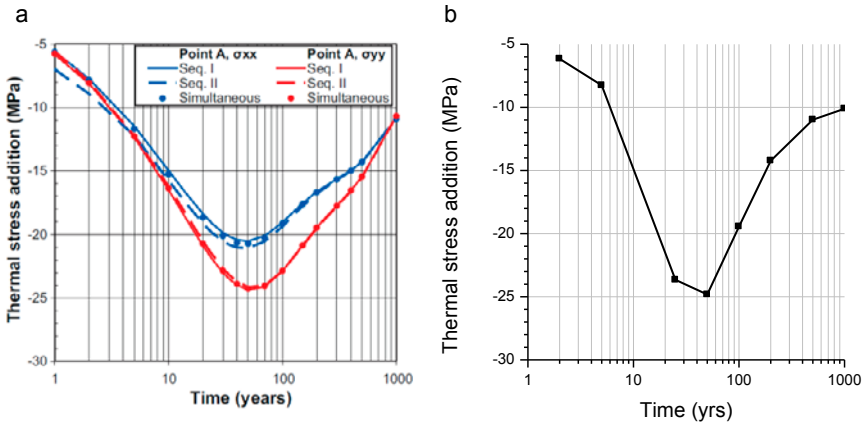


**Figure 32.** (a) Thermal stress increment at Point A in a generic repository consisting of rectangular deposition areas with simultaneous and sequential depositions (Figure 6-6 in Hokmark et al. 2010) and (b) increment of the thermally induced maximum principal stress monitored at the particle at the centre of Panel A modelled as a plane heat source.

Figure 32 compares the temporal changes of the thermal stress increments that are modelled (a) in the 3DEC modelling (Hökmark et al., 2010) and (b) in the PFC2D modelling. Figure 32a the thermal stress increment is monitored in a generic repository consisting of rectangular deposition area. In this modelling, the heat power applied to the rectangular deposition area is uniformly distributed over the entire deposition area by dividing the heat power curve (black curve in Figure 13) with the intervals between the deposition tunnels (40 m) and the deposition holes (6 m). The results show that the thermally induced maximum stresses ($\sigma_{xx}$ and $\sigma_{yy}$) are in the range between 20 MPa to 25 MPa.

Similar result is obtained in the PFC2D modelling as shown in Figure 32b. It should be noted that the result shown is obtained from the heat modelling where all the particles within Panel A area are grouped together and assigned with areal averaged heat power as same as in Hökmark et al. (2010). The stress components are then measured at one particle at the centre of the Panel A, i.e. Particle #1 in Figure 16a.

Despite the differences in the geometry of the models, boundary and initial conditions and the way of modelling heat transfer and thermal stresses between the two models, the results shown in Figure 32 show a strong similarity. The maximum thermal stress addition of 25 MPa is monitored at 50 years, and drops to 10 MPa at 1,000 years. This finding demonstrates that the modelling of heat transfer and thermal stress evolution in the PFC2D can be judged reliable.

Figure 33 compares two cases of distribution of thermally induced seismic events accumulated over 25 years after the start of simultaneous heating of the panels. Figure 33a is from Yoon et al. (2014) where the thermal modelling was done using a temperature controlled simultaneous heating of the four panels. The rock mass with initial temperature of 11.2 °C is instantaneously increased to 50 °C at the heater particles. Such large temperature increase over a few square kilometres results in thermal shock and induces relative large magnitude seismic events, e.g. $M_w$1.6, $M_w$2.2, $M_w$2.3 and $M_w$2.2 at the centre of the Panels A, B, C and D, respectively. These four large seismic events are computed using the numerical moment tensor in Yoon et al. (2014) which is a modified version of Hazzard and Young (2002, 2004). The instantaneous increase of the temperature field results in increase of the size of the particles due to the thermal expansion. This resulted in an increase of deviatoric

stresses at the bonded contacts and led to breakages of the bonds within the panels and at the boundary of the panels. Such bond breakages taking place almost simultaneously led to large changes of contact forces, hence, to large magnitudes with the event hypocentres located at the centre of the panels.

Figure 33b shows the result in this report for the simultaneous heating by means of controlled heat power and the largest seismic event has magnitude $M_w$0.7. Compared to Figure 33a from Yoon et al. (2014), at the same location in the temperature controlled model a value of $M_w$1.05 was obtained. This shows that thermally induced seismic events were overestimated in Yoon et al. (2014).

The results presented in this report should be interpreted with caution. This is due to the fact that the shear displacements of the smooth joints at the fracture intersections and deformation zone intersections are also likely to be overestimated, as discussed in Section 2.7. Stress concentration at the deformation zone intersection, indicated by the arrow in Figure 33b, can lead to failure of the rock mass adjacent to the intersection. This implies that the concentrated energy at the intersection can be distributed to the neighbouring area. This might result into, instead of a single induced seismic event with magnitude $M_w$0.7, into multiple seismic events with lower magnitudes distributed over the area adjacent to the intersection.

Figure 34 shows the critical fractures, indicated in red, for which (a) the mean shear displacement for temperature controlled input in Yoon et al. (2014), and (b) the median shear displacement for controlled heat power input in this report, exceed the canister damage threshold of 50 mm. In the example from Yoon et al. (2014), there are five critical fractures. Only one of these critical fractures, however, intersects the deposition panels. As discussed above, such shear displacements values are affected by the temperature controlled input in the models. When using the controlled heat power input in the models, the median shear displacement does not exceed the canister damage threshold for any of the fractures. Both the results in Figure 34 are affected by the artefact in the PFC2D models because of unbreakable and/or rattling particles.

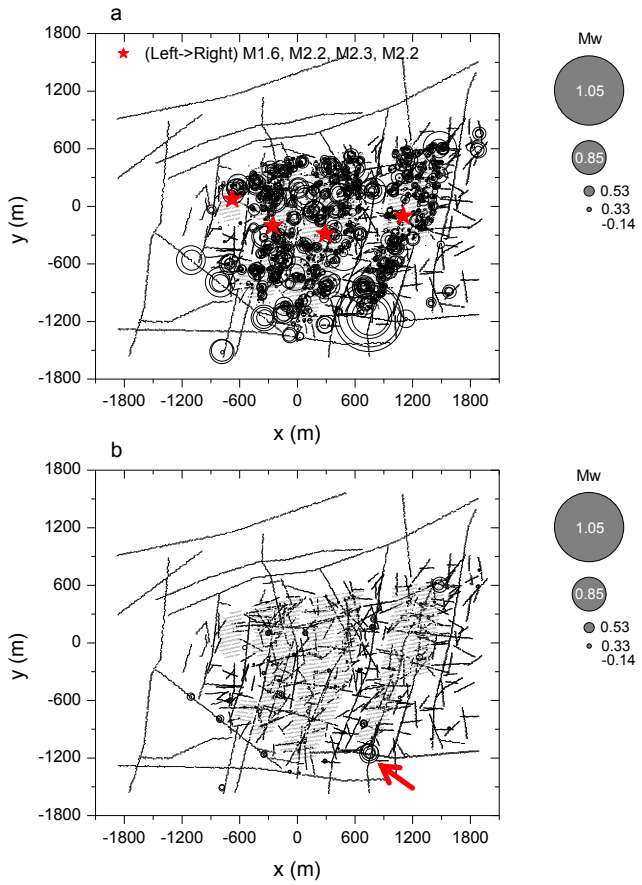


**Figure 33.** Comparison of the thermally induced seismic events accumulated over 25 years after start of simultaneous heating of the panels in the PFC2D horizontal section model with DFN03h realization, modelled (a) by Yoon et al. (2014) and (b) in this report.

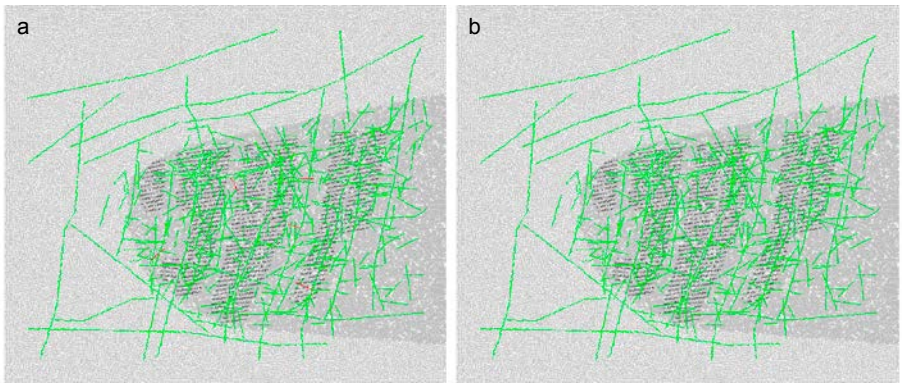


**Figure 34.** Location of the fractures (a) with mean shear displacement for temperature controlled input in Yoon et al. (2014), and (b) with median shear displacements for heat power controlled input in this report, exceeding canister damage threshold of 50 mm at 25 years after start of simultaneous heating of the panels in the PFC2D horizontal section model with DFN03h realization.

# 5. Modelling of heat induced seismicity and fracture shear – vertical section model

## 5.1. Temperature distribution

Figure 35 shows the temperature distributions at several selected times resulting from simultaneous heating of the panels in the PFC2D vertical section model. The distribution of temperature increase shown in Figure 36 is obtained by subtracting the initial temperature field (Figure 12d) from the absolute temperature distribution shown in Figure 35.

Two scanlines are drawn to see how the temperature increase changes with depth and with time. Scanline 1 cuts through Panel C, and Scanline 2 cuts through the area between Panel C and Panel D (Figure 36). The locations of the two scanlines are intended to be similar to Scanlines B and A in the SKB's 3DEC model as shown in Figure 16b (Hökmark et al. 2010).

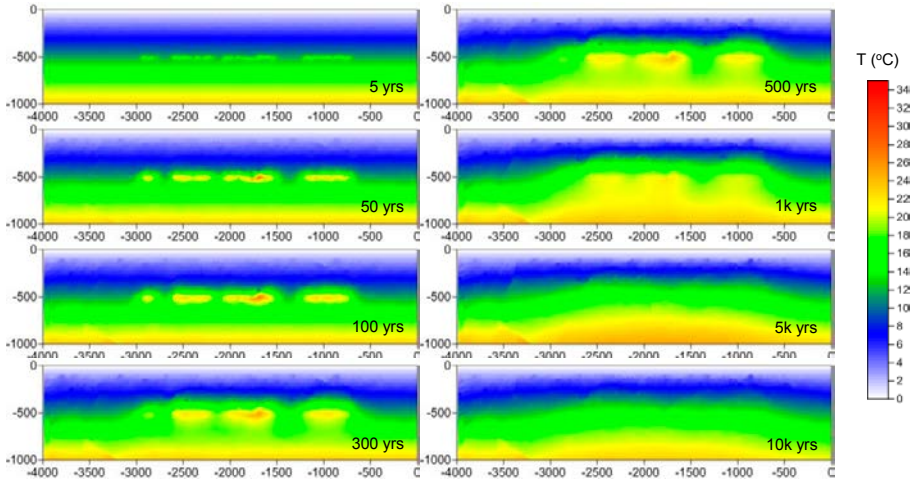


**Figure 35.** Distribution of the absolute temperature at several selected times resulting from the simultaneous heating of all the panels in the PFC2D vertical section model.

Figure 37 shows the temperature increase with depth monitored at the two scanlines. At early times, temperature increase concentrates at the repository depth. The temperature increase at the repository depth is maximum at 100 years. After longer times, heat is transferred to the upper and lower part of the rock mass and the profile of the temperature increase become more diffused. Temperature increase monitored along Scanline 2 shows that the temperature at the repository depth increases continuously until about 1,000 year and reaches a maximum of about +15°C.

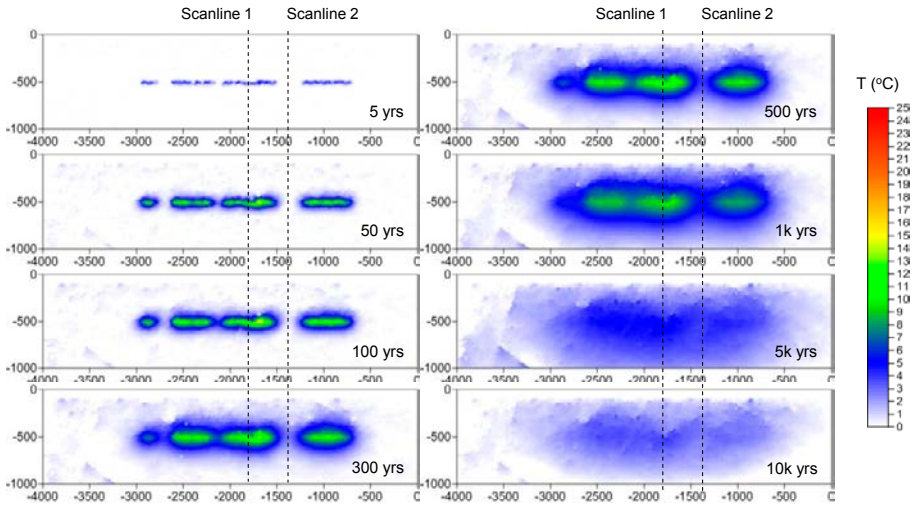


**Figure 36.** Distribution of the temperature increase at several selected times resulting from the simultaneous heating of all the panels in the PFC2D vertical section model.

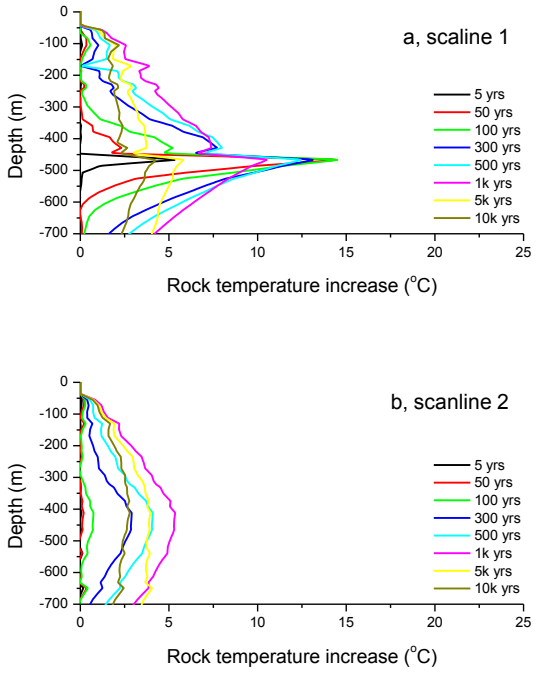


**Figure 37.** Rock temperature increase monitored at several selected times along (a) Scanline 1 and (b) Scanline 2, resulting from the simultaneous heating of all the panels in the PFC2D vertical section model.

Figure 38 shows the temperature distributions at several selected times resulting from the sequential heating in the PFC2D vertical section model. Distribution of the temperature increase shown in Figure 39 is obtained by subtracting the initial temperature field (Figure 12d) from the absolute temperature distribution as shown in Figure 38. Temperature increase monitored along the scanlines (Figure 40) is

almost the same as those in the simultaneous heating (Figure 37), except for very short times as 5 years (black curve in Figure 40a).

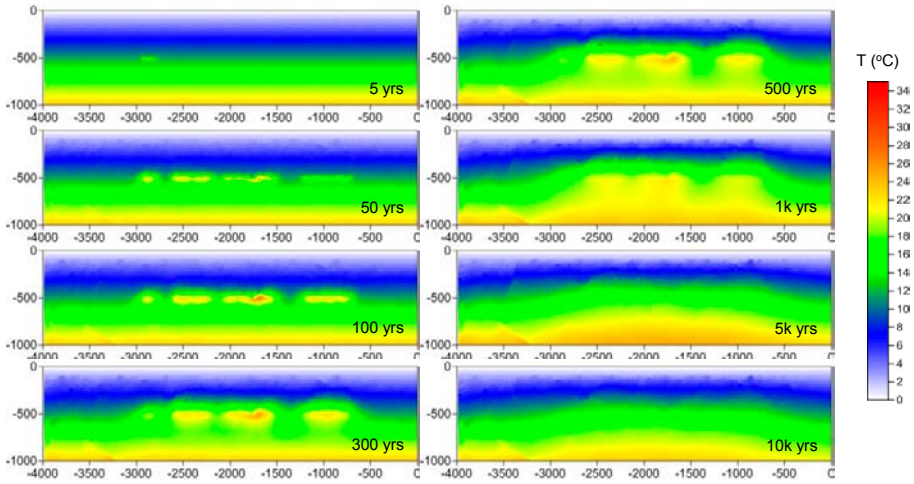


**Figure 38.** Distribution of absolute temperature at several selected times resulting from sequential heating of the panels in the PFC2D vertical section model.

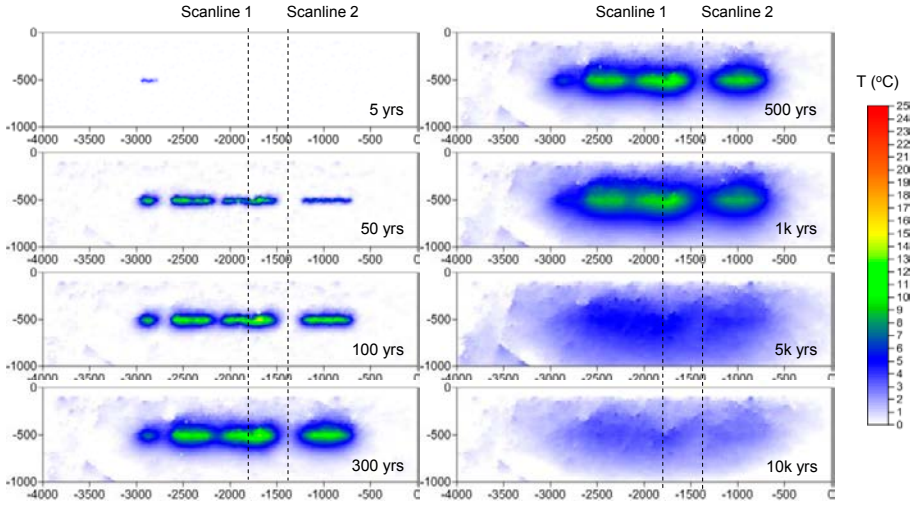


**Figure 39.** Distribution of temperature increase at several selected times resulting from sequential heating of the panels in the PFC2D vertical section model.

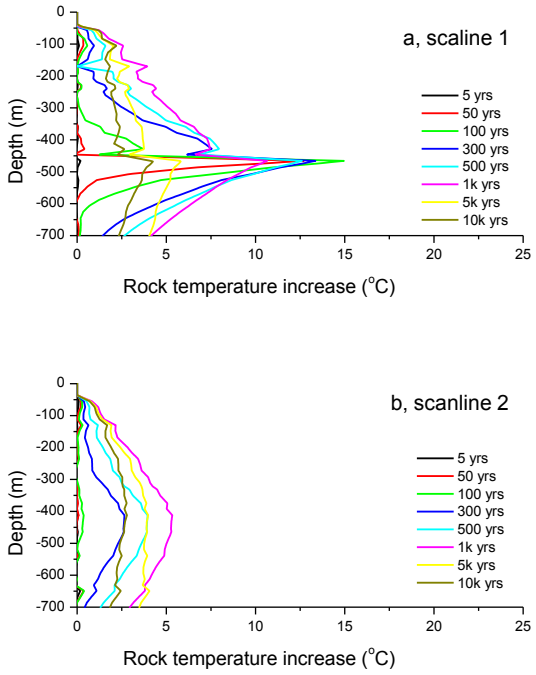


**Figure 40.** Rock temperature increase monitored at several selected times along (a) Scanline 1 and (b) Scanline 2, resulting from the sequential heating of the panels in the PFC2D vertical section model.

## 5.2. Thermally induced stresses

Thermally induced stress changes at the repository depth are monitored at Scanline 1 (passing through Panel C) and Scanline 2 (passing between Panel C and D). These are shown in Figure 41. The convention for the stresses is: compressive stress is negative and tensional stress is positive. We compare the results of PFC2D modelling with the results of 3DEC modelling in Hökmark et al. (2010). Scanline 1 in the PFC2D modelling corresponds to Scanline B in the 3DEC modelling. The result shows that the largest increment in the maximum horizontal stress and the vertical stress modelled in PFC2D are -11.5 MPa and -3.8 MPa, respectively, and occur at 1,000 years. By reading the graphs of 3DEC modelling results (circled parts in Figure 41), one can see that the largest increment in the maximum horizontal and the vertical stresses are -13 MPa and -2.5 MPa, respectively, and occur at 100 years (light green curves).

Comparison of the two results show that the thermally induced stress changes for the maximum horizontal and vertical stresses are comparable in terms of magnitude, but the major difference is the time when the stress changes become the largest, i.e. 1,000 years in the PFC2D modelling, and 100 years in the 3DEC modelling. The reason for such difference is partially due to the presence of the fractures. When the particle temperature increases, the particle size increases as a function of temperature and the thermal expansion coefficient. Particle size increase leads to changes in the contact forces around the particles which increase or decrease depending on the packing structure, and even breakage of bond which might hinder heat transfer. As the stress distribution depends on the stress components stored in the particles, which are based on the contact forces, the presence of smooth joints

mostly concentrated at the repository depth may have influence on the development of the thermally induced stresses due to rock damage and fracture slip. In 3DEC modelling, the modelled rock mass is elastic with isotropic and homogeneous properties and without discontinuities. This explains why the time of maximum temperature increase at near-field (100 years) matches with the time of maximum thermal stress (100 years).

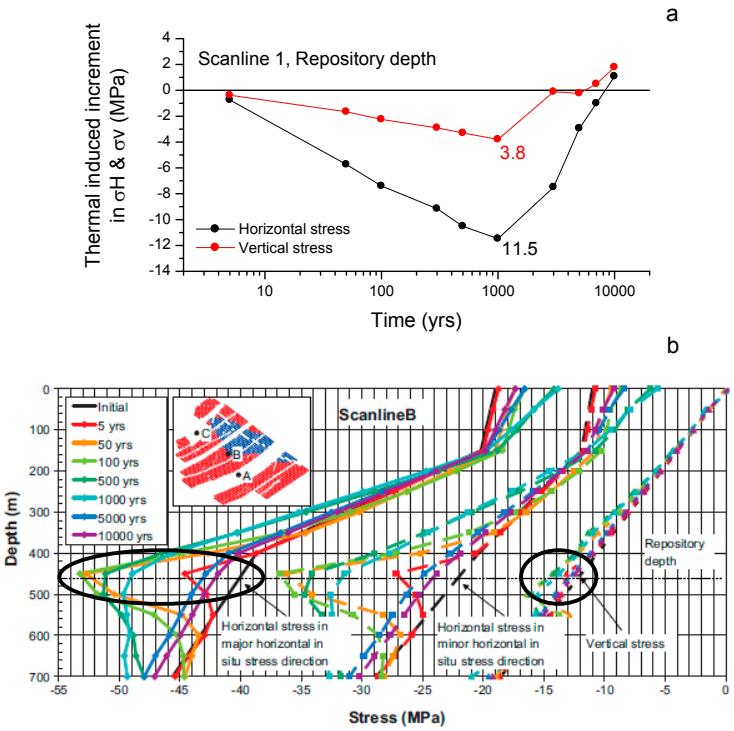


**Figure 41.** (a) Thermally induced changes in the maximum horizontal and the vertical stresses at the repository depth monitored by Scanline 1 in the PFC2D vertical section model with simultaneous heating (tension in positive and compression in negative) and (b) changes in the stresses with depth along Scanline B induced by the heating in 3DEC modelling (Hökmark et al. 2010).

We also monitored the thermally induced stress changes at the repository depth along Scanline 2, which passes between Panel C and D and there are less fractures compared to Scanline 1. The thermally induced stresses are, therefore, less influenced by the presence of the fractures. As shown in Figure 42, the largest increments in the maximum horizontal and the vertical stresses in PFC2D modelling are -3.6 MPa and -0.4 MPa, respectively, and occur at 500 years. The results from 3DEC modelling show that the largest increment in the maximum horizontal stress is -6.5 MPa and occurs at 500 years (seen by the dark green curve). The vertical stress changes are of the order of +3 MPa, therefore mostly tensional in the PFC2D and 3DEC modelling.

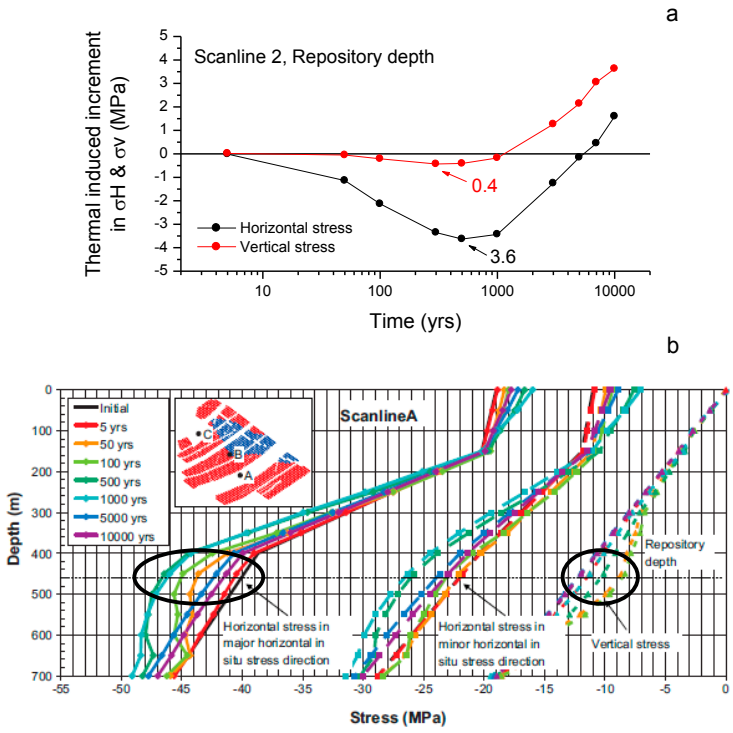


**Figure 42.** (a) Thermally induced changes in the maximum horizontal and the vertical stresses at the repository depth monitored by Scanline 2 in the PFC2D vertical section model with simultaneous heating (tension in positive and compression in negative), and (b) changes in the stresses with depth along Scanline A induced by the heating in 3DEC modelling (Hökmark et al. 2010).

## 5.3. Induced seismicity

Figure 43 shows the distribution of the thermally induced seismic events and smooth joints shear displacement at 100 years resulting from simultaneous and sequential heating of the repository panels in the PFC2D vertical section models. The largest magnitude is obtained at the point of intersection of two deformation zones, ZFMWNW0810 and ZFMA1 and reaches a magnitude $M_w$1.7. By the colouring of the smooth joints, gently dipping deformation zones close to the ground surface are showing slightly larger displacement than those steeply dipping.

As in the horizontal section model, the results should be interpreted with caution especially when studying the large magnitude seismicity at the location of deformation zone intersection. This is because the large displacement of the smooth joints at the deformation zone intersections can be attributed to numerical artefact as discussed in Section 2.7. If the stress concentrated at the deformation zone intersections is high enough to induce local failure of the rock, this can lead to multiple events distributed over a larger area with resulting lower magnitudes rather than one single event of $M_w$1.7.

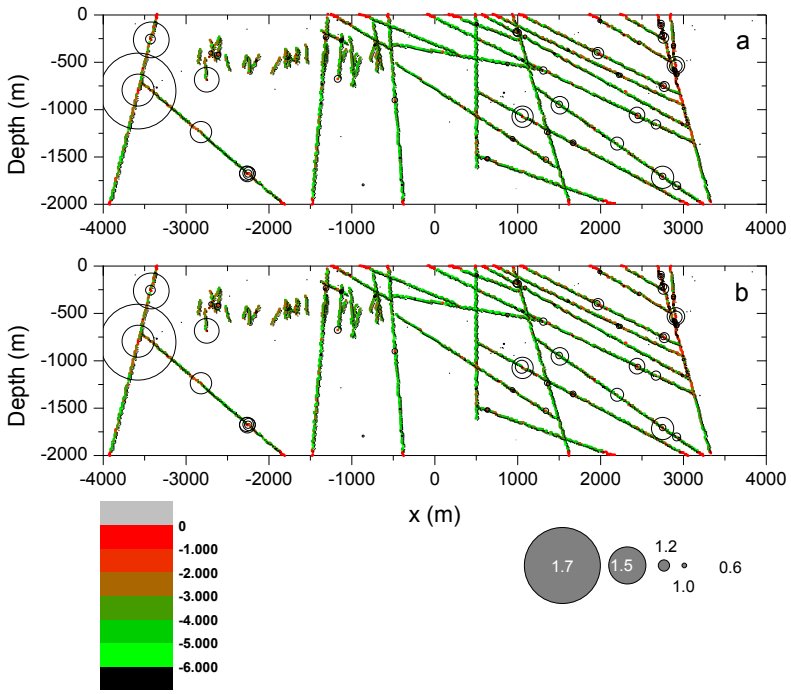


**Figure 43.** Distribution of the thermally induced seismic events associated with bond breakages and slip of the smooth joints that are accumulated over 100 years resulting from (a) simultaneous and (b) sequential heating in the PFC2D vertical section model with DFN06v realization.

## 5.4. Fracture shear displacements

The fractures are classified into two classes depending on the length. Fractures in Class 1 have length between 100 m and 200 m. Fractures in Class 2 have length between 200 m to 600 m. As discussed in Section 2.7, and as same as for the horizontal section models, the median value of shear displacement of the smooth joints constituting the fracture is selected as a representative shear displacement of the fractures.

Figure 44 shows the temporal changes of the median of the shear displacement of the (a) Class 1 fractures and (b) Class 2 fractures until 10,000 years resulting from the simultaneous heating of the panels. Temporal changes of the shear displacement of the fractures resulting from the sequential heating are similar to those from the simultaneous heating (Figure 45).

In both heating sequences (Figures 44 and 45), there are no fractures with median shear displacements larger than 50 mm within the simulated time of 10,000 years.

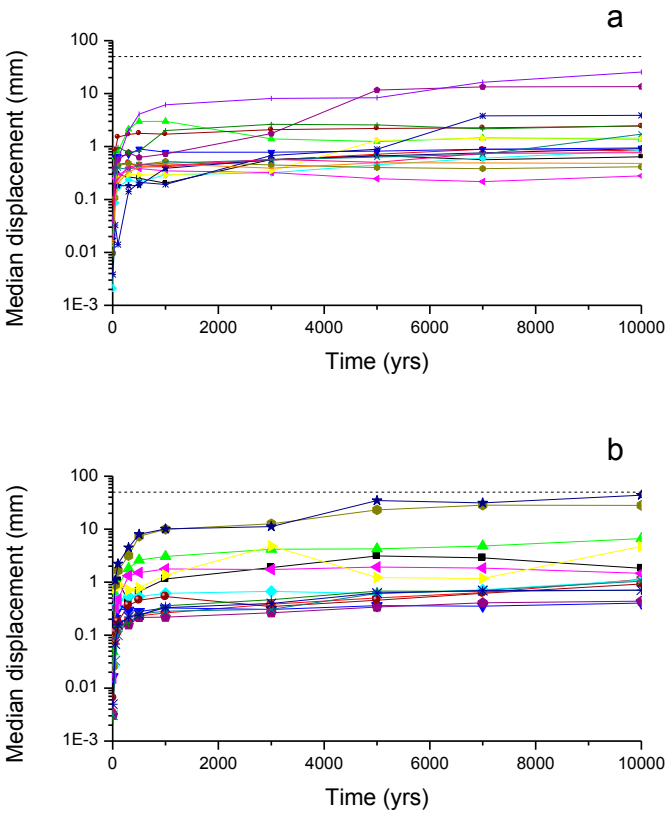


**Figure 44.** Temporal changes of the median shear displacement of the (a) Class 1 fractures (100 – 300 m) and (b) Class 2 fractures (300 – 600 m) in DFN06v realization, resulting from the simultaneous heating of all the panels in the PFC2D vertical section model, until 10,000 years. The dashed lines represent the 50 mm canister damage threshold.

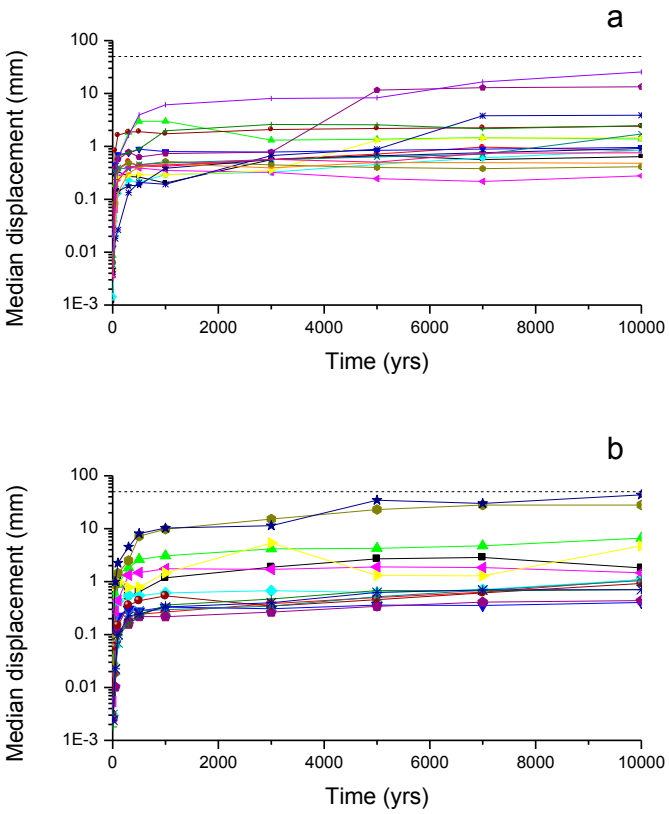


**Figure 45.** Temporal changes of the median shear displacement of the (a) Class 1 fractures (100 – 300 m) and (b) Class 2 fractures (300 – 600 m) in DFN06v realization, resulting from sequential heating of the panels in the PFC2D vertical section model, until 10,000 years. The dashed lines represent the 50 mm canister damage threshold.

## 5.5. The Consultants' assessment

Figure 46 compares the temperature increase with depth modelled with 3DEC (Hökmark et al., 2010) and modelled with PFC2D in this study. The figures for the PFC2D modelling (Figures 46b and 46d) are identical to Figure 37, but the colour code is changed in order to be consistent with the results of 3DEC modelling. In general, the distribution of the temperature increase shows a fair qualitative matching between the two results. A strong similarity is that the rock temperature increase is maximum at 100 years and then decreases. In the early time of the repository heating (time shorter than 50 years), the temperature increase is mostly concentrated at the repository depth, but the temperature curve become diffused in the long term due to the heat transfer to the upper and lower parts of the rock mass.

However, the temperature increase modelled with PFC2D does not show a quantitative good match to that modelled with 3DEC. The maximum temperature increase at the repository depth at 100 years is 26°C in 3DEC modelling, whereas it is about 15°C in PFC2D modelling. This is due to the fact that in the 3DEC model in Hökmark et al. (2010) the heat coming from the neighbouring deposition tunnels gives contribution to the temperature increase, while in the PFC2D modelling the applied heat power is averaged in the out-of-plane direction by dividing the power (black curve in Figure 13) with the distance interval between the deposition tunnels

(40 m), and there is no additional heat source contributed from the out-of-plane direction.

Temperature increase along depth at the point between the panel areas (Scanline A in 3DEC and Scanline 2 in PFC2D) shows continuous increase until it hits the maximum 1,000 years. Reduction of the temperature increase after 1,000 years is also confirmed in this study. Contrary to the temperature increase monitored in Scanline B and Scanline 1, the difference between the results of 3DEC and PFC2D is small (about 2 to 3°C).

Another discrepancy found between the results of 3DEC and PFC2D modelling is the wiggly distribution of the temperature in the rock mass above the repository depth. This is due to some heat induced breakage of particle bonds in the PFC2D model, and consequent discontinuous heat flow pipes that disturb the homogeneous temperature distribution that is instead observed in the 3DEC model (Figure 46a). In the 3DEC modelling, the rock mass is modelled as linearly elastic with homogeneous properties.

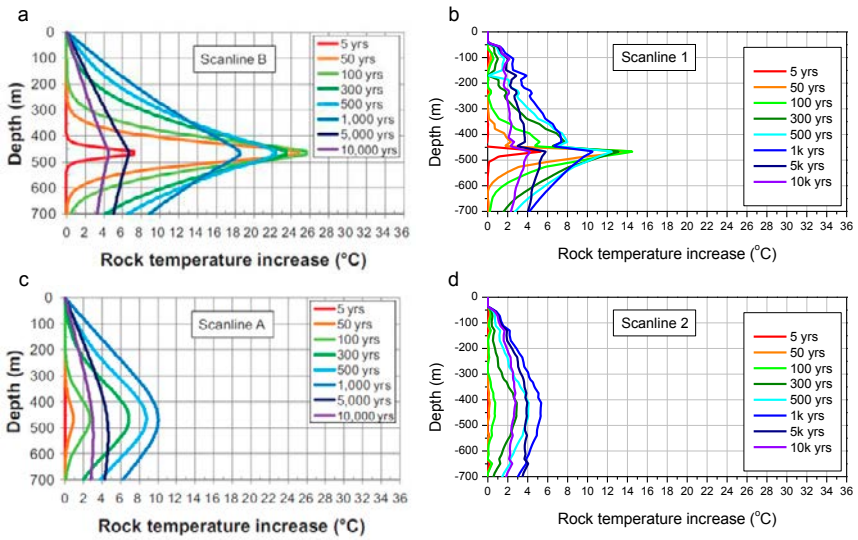


**Figure 46.** (Left column) Rock temperature increase along (a) Scanline B and (c) Scanline A from the 3DEC model (Hökmark et al. 2010) and (right column) the rock temperature increase along (b) Scanline 1 and (b) Scanline 2 from the PFC2D vertical section model in this study.

We tested the temporal evolution of the stresses under different mechanical boundary conditions assigned to the particles at the outer boundary layers of the model. For the modified mechanical boundary condition, stiff rollers are assigned to the left, bottom and right outer layer particles and the movement of the top surface is left free.

Thermally induced stress changes at the repository depth in the model with modified mechanical boundary condition are monitored along Scanline 1 (passing through Panel C) and Scanline 2 (passing between Panel C and D) and shown in Figure 47. Compressive stress is negative and tensional stress is positive. The result shows that the largest increment in the maximum horizontal stress and the vertical stress scanned by Scanline 1 are -8.5 MPa and -2.4 MPa, respectively, and occur at 300 years. Along the Scanline 2, the largest increment in the maximum horizontal

stress is -3.2 MPa and also occurs at 300 years. Change in the vertical stress is tensional.

From comparison of the thermal induced stresses in the models with different mechanical boundary conditions (Figures 41 and 42 vs. Figure 47), we concluded that the thermal induced stress changes shown in Figures 41 and 42 are closer to the thermally induced stress changes that are modelled in the 3DEC modelling. Large induced tensile increments of the stresses are not likely to occur on the long term either. This supports our decision for choosing the results of the modelling with the softened top boundary as in the rest of Chapter 5 and 6.

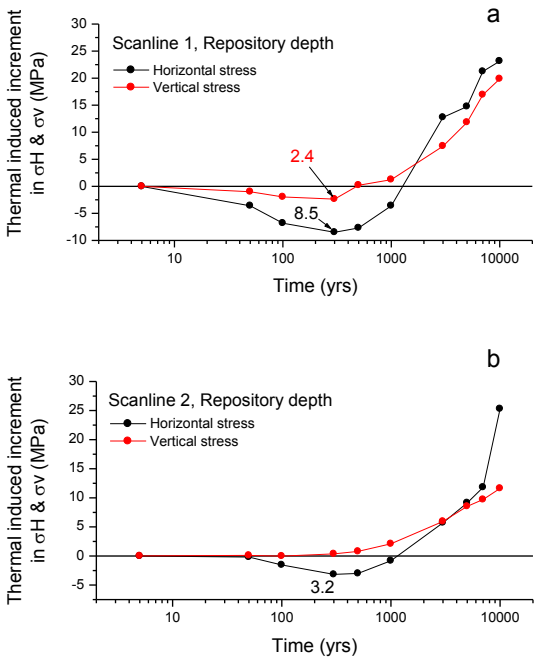


**Figure 47.** Thermally induced changes in the maximum horizontal and the vertical stresses at the repository depth monitored by (a) Scanline 1 and (b) Scanline 2 in the PFC2D vertical section model with sequential heating (tension in positive and compression in negative) with modified boundary condition.

# 6. Modelling of heat-and-earthquake induced seismicity and fracture shear – horizontal and vertical section models

## 6.1. Activation of ZFMWNW0809A in the horizontal section model

In this modelling case it is assumed that an earthquake takes place at the deformation zone ZFMWNW0809A at 100 years after the start of simultaneous heating of all the panels.

Figure 48a shows the thermally induced seismic events accumulated over 100 years since the start of heating of the panels. The values of shear displacement of the smooth joints constituting the fractures and the deformation zones are shown on a logarithmic scale by different colours. At 100 years after start of heating, ZFMWNW0809A is activated by releasing the strain energy stored at the trace of the deformation zone, which yielded $M_w$4.7 earthquake with hypocentre location indicated by red star. Activation of ZFMWNW0809A induces many seismic events mostly concentrated at areas of high fracture density and intersections with deformation zones (Figure 48b). The largest induced seismic event is $M_w$1.9. The median shear displacement of the activated ZFMWNW0809A is 71 mm. The median shear displacement is comparable to the empirical relation by Wells and Coppersmith (1994) in terms of fault length and slip displacement (see Figure E-1 in Appendix E).

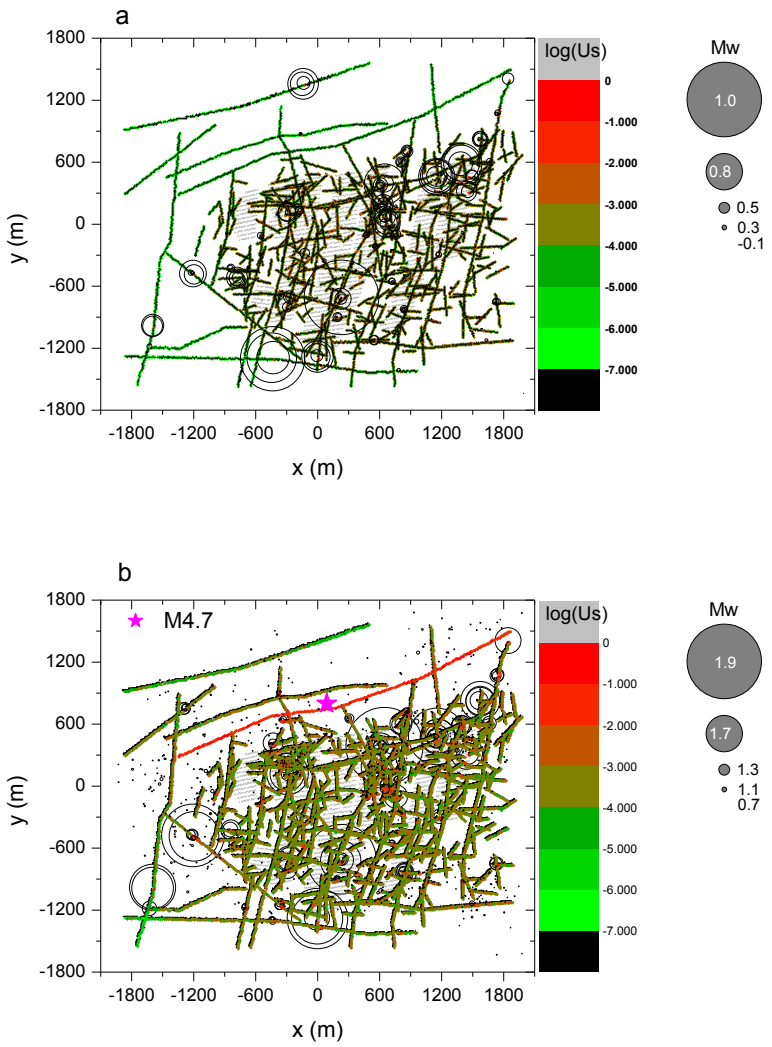


**Figure 48.** Distribution of the seismic events and the smooth joints shear displacements induced by (a) after 100 years of simultaneous heating, (b) earthquake at deformation zone ZFMWNW0809A occurring 100 years after the start of simultaneous heating of the panels in the PFC2D horizontal section model with DFN03h realization.

## 6.2. Activation of ZFMA3 in the vertical section model

This modelling case assumes that an earthquake takes place at the deformation zone ZFMA3 100 years after the start of simultaneous heating of the deposition panels. Figure 49a shows the thermally induced seismic events accumulated over 100 years since the start of the heating of the panels. Activation of ZFMA3 results in an earthquake of magnitude $M_w$4.7 with hypocentre location indicated by red star. This triggers a concentration of many events at the areas where the deformation zone intersects other zones (Figure 49b). The median shear displacement of ZFMA3 is 30 mm, which is comparable to the empirical relation by Wells and Coppersmith (1994) (see Figure E-2 in Appendix E). The figure shows that activation of ZFMA3 results in seismic event at the intersection of ZFMA1 and ZFMENE0810 with

magnitude $M_w$2.0. The result of this modelling shows that activation of one gently dipping deformation zone can trigger movement of other deformation zones that are located far (5 to 6 km) from the earthquake hypocentre.

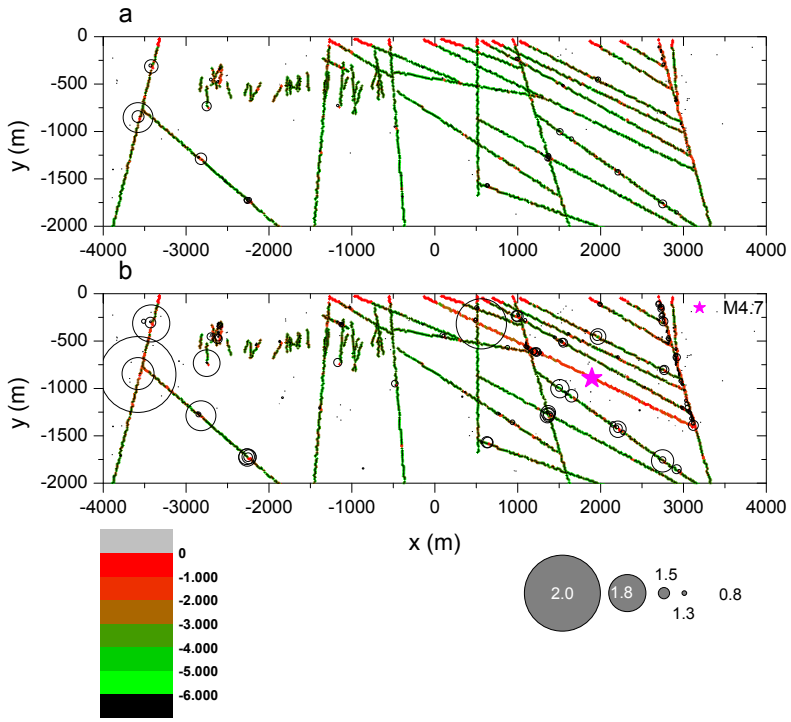


**Figure 49.** Distribution of the seismic events and the smooth joints shear displacements induced by (a) 100 years of simultaneous heating, (b) earthquake at deformation zone ZFMA3 occurring 100 years after the simultaneous heating of the panels in the PFC2D horizontal section model with DFN06v realization.

## 6.3. The Consultants' assessment

The results from both horizontal and vertical section modelling cases show that, due to the complexity of the geology, activation of a deformation zone can trigger movement of another deformation zone that is located far from the earthquake hypocentre and across the repository.

Figure 50 shows the median displacements of the fractures (a) in the horizontal and (b) in the vertical section models induced by 100 years of the repository heating (black dots) and induced by earthquakes at deformation zones ZFMWN0809A and ZFMA3 for the horizontal and vertical section models, respectively. In the horizontal section model, the majority of the fractures undergo increase in their shear displacement due to the occurrence of the earthquake. However, as shown in Figure 51a, shear displacements of some fractures decrease when the earthquake occurs. This is due to shear displacement of the fractures in reversed direction induced by the earthquake. In the vertical section model, most of the fractures undergo minor increase in their shear displacement, as shown by the difference of the displacement in Figure 51b. However, the occurrence of an earthquake at the

deformation zone ZFMA3 after 100 years of repository heating led to an increase of the shear displacement on one fractures in the repository area from 11 to 46 mm.

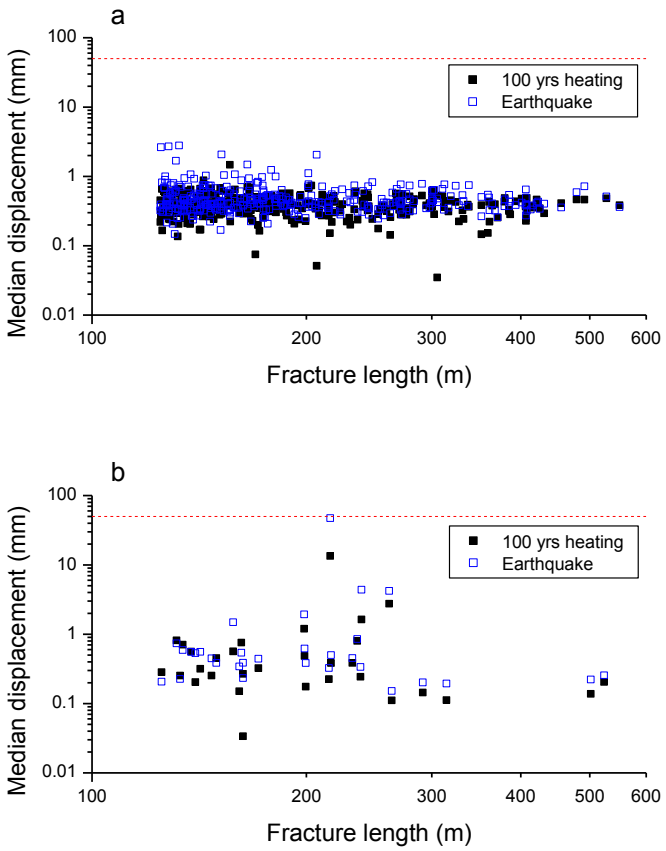


**Figure 50.** Median shear displacement of the fractures induced by 100 years of heating (black) and by an earthquake at deformation zones (blue), (a) ZFMWNW0809A in the horizontal section model and (b) ZFMA3 in the vertical section model.

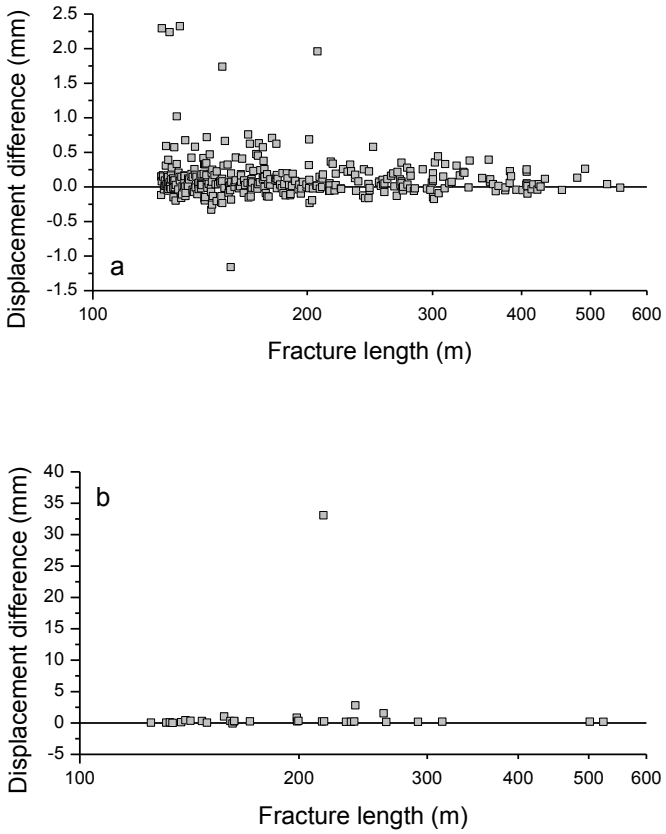


**Figure 51.** Increment (+) or decrement (-) of the median shear displacement of the fractures induced by an earthquakes at (a) ZFMWNW0809A in the horizontal section model and (b) ZFMA3 in the vertical section model compared to 100 years of simultaneous heating only.

# 7. Discussion

## 7.1. Issues related to 2D modelling of 3D problems and geological structures

The heat generated from the canister distributes in three dimensions through the repository volume. In a horizontal section model, the modelled plane is assumed to locate at the mid-height of the canisters. Due to the unit thickness of the models in the out-of-plane direction, it was necessary to modify the heat power curve taking into consideration that the 2D model should realistically represent the 3D geometry and distribution of the heat sources in the rock mass. For the horizontal section, it is assumed that about 10% of the total heat energy emitted from a full size canister goes into the modelled section. One possible solution might be scaling down the heat power curve (black curve in Figure 13). However, instead of scaling down the entire curve, the coefficients $t_i$ are modified so that the heat power is similar to the original curve for short-term and decay faster than the original for the long-term (see $t_i$ values in Table 2). By doing this, the temperature increase distribution in the 2D model match both quantitatively and qualitatively that observed in the 3D modelling by Hökmark et al. (2010).

For the vertical section model, the modelled plane is assumed along the NE-SW cross section through the repository volume (Figure 12a). Due to unit thickness in the out-of-plane direction, it is assumed that each panel contains only one line source where the heat power curve is divided by the deposition tunnel spacing (40 m). Unlike in the horizontal section model, the full size canister heat power curve is used here. The distribution of the temperature increase matches qualitatively well that simulated in the 3DEC modelling by Hökmark et al. (2010). However, the maximum temperature increase at the repository depth at 100 years is 15°C instead of 26°C as in the 3DEC modelling (Figure 46). This is due to the fact that in the 3DEC model by Hökmark et al. (2010), there is heat contribution from the neighbouring deposition tunnels. In PFC2D model the heat is averaged along the direction perpendicular to the deposition tunnels, i.e. heat power is divided by the deposition tunnel spacing, and there is no additional source of heat in the out-of-plane direction.

The fracture sets at Forsmark are mainly steeply and gently dipping. This means that some of the fractures cannot be captured by the horizontal or vertical section modelled.

Heat induced deformation of the rock mass and the fracture displacement are modelled with PFC2D under the assumption of plane-strain condition. This means that there is no movement of the rock mass in the out-of-plane direction, and rock mass deformation is concentrated on the modelled plane, e.g. repository depth at the mid-height of the canisters for the horizontal section model. This is a conservative assumption. If the heat induced expansion of the rock mass is allowed in the out-of-plane direction, as in a 3D model, there will be less amount of energy spent on the expansion of the rock mass in the model plane and this would consequently result in lower shear displacement of the fractures.

## 7.2. No fractures exceed the canister damage threshold of 50 mm

In the horizontal section PFC2D models, there are no fractures where the median of the shear displacement induced both by the simultaneous and sequential heating of the panels within the simulated time period of 3,000 years. Also, there are no fractures where the median shear displacement induced by an earthquake occurred at deformation zone ZFMWNW0809A after 100 years of the repository heating exceeds the canister damage threshold of 50 mm.

Even in the vertical section PFC2D model, there are no fractures where the median of the shear displacement induced both by the simultaneous and sequential heating of the panels exceed 50 mm within the simulated time period of 10,000 years. Also, there are no fractures where the median shear displacement induced by an earthquake occurred at deformation zone ZFMA3 after 100 years of the repository heating exceeds the canister damage threshold of 50 mm.

## 7.3. Seismicity at the intersections of the deformation zones

In all PFC2D modelling cases studied, it is shown that seismic events either induced by the heating and/or by the earthquakes tend to cluster at the place where the fracture density is high and where the deformation zones intersect. It is shown and discussed in Section 2.7 that the interaction between the fractures and deformation zones make the stress concentrate at the intersection area. In the PFC2D models, concentrated stress at the intersections results in localized displacement of the particles, hence the smooth joints around exhibit significantly large displacement. Such large displacements of the smooth joints can then interpreted as large magnitudes induced seismicity.

In nature, stress concentrated at the fracture intersections may easily lead to a local failure of the intact rock or shear of fractures, which consequently results in multiple seismic events distributed over an rock mass volume around the location of intersections. Field evidences on the Pärvie fault system in Ahmadi et al. (2015) support this interpretation. Figure 52 shows the cross section of the seismic imaging of the Pärvie fault system. Red dashed lines depict the interpreted faults. A dense cluster of seismic activity is located at a depth of 11.5 km, where the two faults, West-dipping R1 and the main East-dipping R3 (Pärvie) converge. This implies that the intersection of faults is the source of clustered seismic activity. Another field evidence can be found for Soultz-sous-Forêt in France as reported by Sausse et al. (2010) that shows seismicity clustered at intersections between faults.

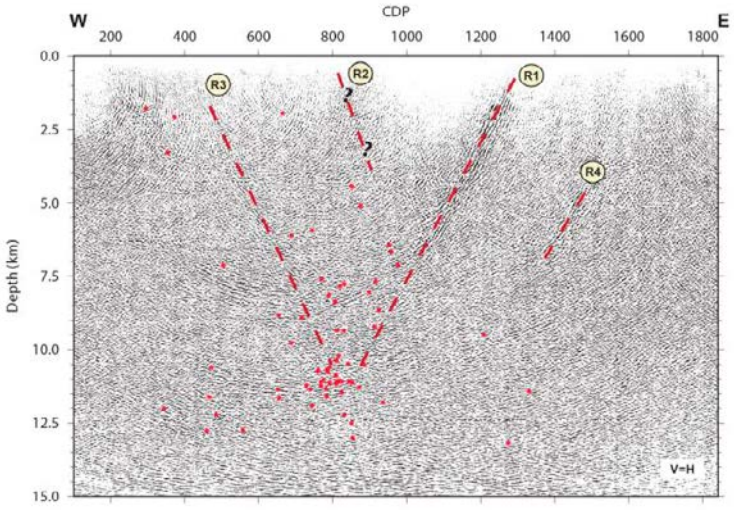


**Figure 52.** Cross section of the earthquakes overlaid on the interpreted migrated section (Figure 9 in Ahmadi et al. 2010).

## 7.4. Validity of magnitudes from PFC2D simulated earthquakes

For calculation of the magnitudes of the simulated earthquakes, we used the moment tensor approach. The numerical technique was developed by Hazzard and Young (2002, 2004) and later modified by Yoon et al. (2014) to make it functional to the failure of the smooth joint representing the deformation zones. Each bond breakage in PFC represents a smooth joint failure. When the bond breaks, the two particles on either side of the joint (event source particles) move and contacts surrounding the source particles undergo some deformation and result in a force change at the surrounding contacts. The moment tensor approach uses the change in contact forces around the bond breakages to construct a moment tensor from which seismic moments and moment magnitudes are computed.

In PFC2D, if a bond breakage initiates at the area of fracture intersection, a highly localized particle displacement as shown in Figure 6 could occur. In some cases this could overestimate the magnitude as the contact force determined by the relative displacement between the particles making the contact due to a numerical artefact of detachment of the particles as discussed in Section 2.7. It also means that also the magnitudes of the simulated earthquakes at deformation zones could be affected by this problem.

At the current state of knowledge, it is not possible to quantify how much the influence of the numerical artefact has on the calculation of earthquake activation magnitudes. Validation of the magnitudes can only be checked by comparing the results with empirical scaling relations of natural tectonic earthquakes, e.g. rupture area versus magnitude, rupture length versus slip displacement, slip displacement versus stress drop as reported by Wells and Coppersmith (1994), Leonards (2010), Zoback and Gorelick (2012). Table 6 lists several scaling parameters of the simulated deformation zones and earthquakes (L: rupture length, R: source radius, $M_w$: moment magnitude, $\Delta\sigma$: stress drop, $d$: median slip displacement).

The magnitudes of the simulated earthquakes are validated using the data of natural tectonic earthquakes in Wells and Coppersmith (1994) and in Manighetti et al.

(2005) in Figure 53. The PFC2D simulated earthquake data are indicated by the stars. The red stars indicate the modelling results where the width of the deformation zones in the out-of-plane direction is assumed to be the same as the length of the deformation zones, i.e. length:width = 1:1 as also shown in Figure 18. The blue stars are the modelling results with another assumption of rupture length:width ratio of 1:1/6.

The figure demonstrates that the magnitude of the natural tectonic earthquake is in general proportional to the size of the fault rupture surface area. The magnitudes of the PFC2D simulated earthquakes are at the bottom tail of the natural data population, but all within the ±3 standard deviation uncertainty range of the empirical regression by Wells and Coppersmith (1994).

**Table 6.** Scaling parameters of the simulated earthquakes.

| Activated DZ | L (m) | R (m) | $M_w$ | Δσ (MPa) | $d$ (m) |
|---|---|---|---|---|---|
| ZFMWNW0809A | 3482 | 1925 | 4.7 | 0.6 | 0.071 |
| ZFMA3 | 3537 | 1333 | 4.8 | 2.2 | 0.039 |

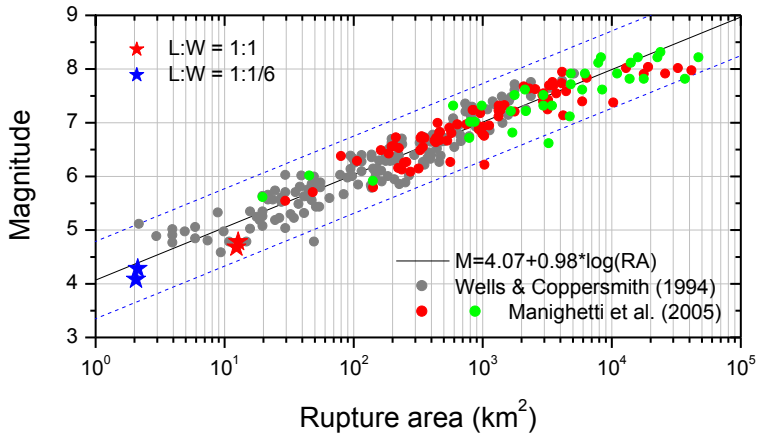


**Figure 53.** Relation between rupture areas and magnitudes of natural tectonic earthquakes and the simulated earthquakes in this study (red and blue stars) and comparison with the regression in Wells and Coppersmith (1994). Uncertainty range of the regression (±3σ) is indicated by the dashed lines.

A second validation of the simulated earthquakes is shown in Figure 54 by using the diagram of fault size versus magnitude, versus slip displacement and versus stress drop in Zoback and Gorelick (2012). The range of deformation zone length is indicated by the vertical shaded bar and the magnitude range of the simulated earthquakes is indicated by the horizontal shaded bar.

From the diagram, the slip displacement and the stress drop estimations of the earthquake are approximately between 0.01 m to 0.1 m and 0.5 MPa to 5 MPa,

respectively. The data of the PFC2D simulated earthquakes in Table 6 match reasonably well the estimations made based on the diagram.

The comparisons of the PFC2D simulated earthquake data with the empirical regressions demonstrate that the results of earthquake simulations are reasonable. It implies that, despite the fact that there is a chance of being influenced by the two dimensionality of the simulation and by some occurrence of the numerical artefact in computation the magnitude, the results are evaluated to be reasonable in terms of various scaling parameters of natural tectonic earthquakes reported in the literature.

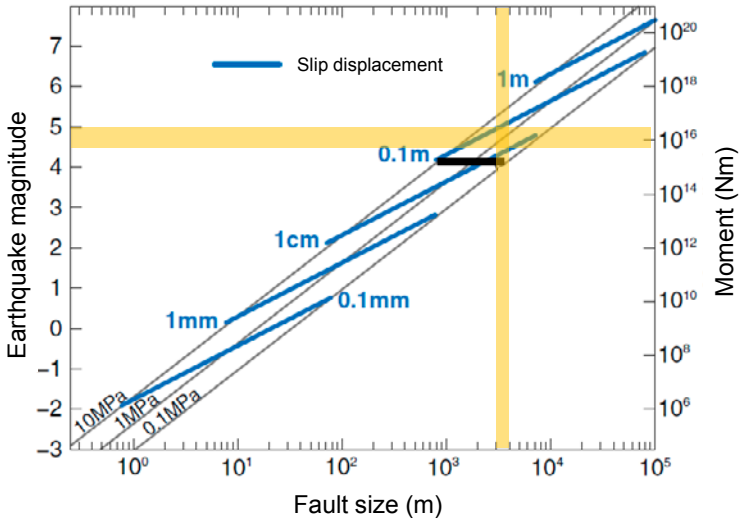


**Figure 54.** Relationships among various scaling parameters for earthquakes (modified from Figure 2 in Zoback & Gorelick, 2012). Range of the fault size and the PFC2D simulated magnitudes are indicated by the shaded bars.

## 7.5. Reanalysis and validity check of the fracture shear displacements in Yoon et al., 2014

In this section, we discuss the validity of the results that were presented in SSM's Technical Note 2014:59 (Yoon et al., 2014). Two issues in that Technical Note have been argued as major drawbacks. The first is that the thermal loading is applied by means of temperature control where the temperature of the repository panel rock mass is increased instantaneously from 11 to 50°C. The second is that if the numerical artefacts at some intersections between fractures were not eliminated therefore the results are seriously influenced.

Figure 55 shows two results of fracture shear displacement from the model shown in Figure 47 in Yoon et al. (2014), where the left diagram shows the distribution of the mean and the right one shows the distribution of the maximum shear displacement. The maximum displacement distribution shows that 17 fractures (about 5% of total number of fractures) experience larger shear displacements than 50 mm, which corresponds to the canister damage threshold shown in red in the figure. Due to the numerical artefacts with displacement "spikes", the maximum displacements cannot be used as a safety assessment parameter. For this reason, the mean values of displacements are presented as results in Yoon et al. (2014) to filter out the "spikes" also interpreted as numerical "outliers". However, due to the significantly large

displacement at some points (displacement spikes) where fractures intersect, it has been argued that even the mean values are not the reliable estimate of the fracture shear displacement.

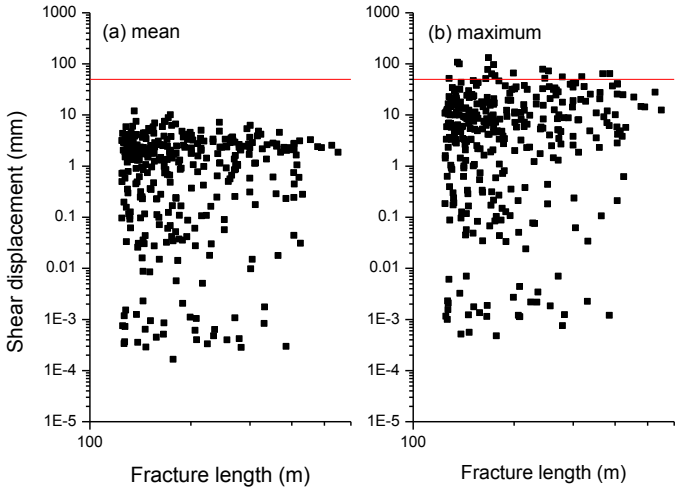


**Figure 55.** Distribution of (a) mean and (b) maximum shear displacement of the fractures resulting after 50 years of sequential panel heating as reported in Yoon et al. (2014).

To investigate this issue we present another comparison shown in Figure 56. The upper row figures are the (a) mean, (b) median, and (c) maximum displacements of the fractures from the results of one model simulation in Yoon et al. (2014) (sequential panel heating, at 50 years, with DFN03h realization, see Figure 48 in the reference). The bottom row figures are the (d) mean, (e) median and (f) maximum displacements of the fractures from the results presented in Figure 21 in this report where the thermal loading is done under power-adjusted control. The comparison of the figures, i.e. mean versus mean, median versus median, maximum versus maximum, demonstrates that the displacement distributions are slightly shifted to lower level when the power-adjusted control and the elimination of the numerical artefacts as in Sections 2.7 are introduced. However, it does not affect the results so much in terms of conservativeness, i.e. upper part of the displacement distribution is similar.

We come back to Figure 55a where the mean values are used as representative displacements of the fractures in Yoon et al. (2014) and compare it with the displacement distributions resulting from power controlled thermal loading where the numerical artefacts are eliminated (Figure 56d, 56e, and 56f). The comparison demonstrates that the mean displacement result in Yoon et al. (2014) (Figure 55a) can be assumed to be more conservative than the results of the mean and median displacement distributions in the models where the artefacts are eliminated (Figure 56d and 56e), but not as conservative as the maximum displacement distribution (Figure 56f).

This implies that, despite the facts that the results in Yoon et al. (2014) are obtained by a less reliable way of inputting the thermal load, i.e. panel rock mass temperature is instantaneously increased from 11 to 50°C, and the numerical artefacts are not properly eliminated, the results can be used with some precaution for judgement on the maximum shear displacements on target fractures necessary for the assessment of the repository operational safety and safety after closure.

Before elimination of the numerical artefacts

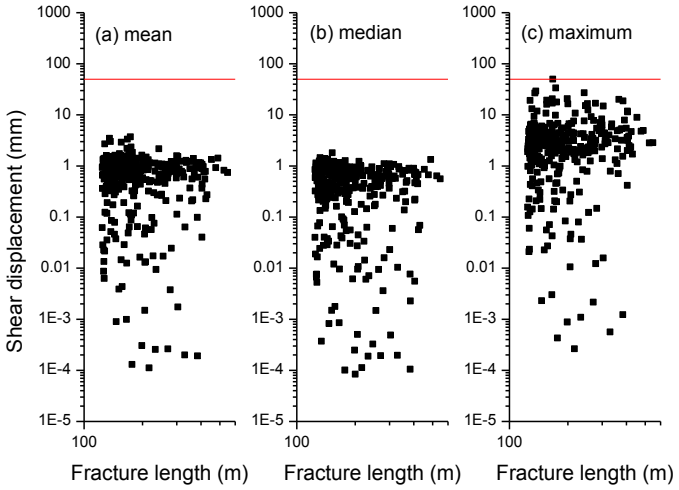


After elimination of the numerical artefacts

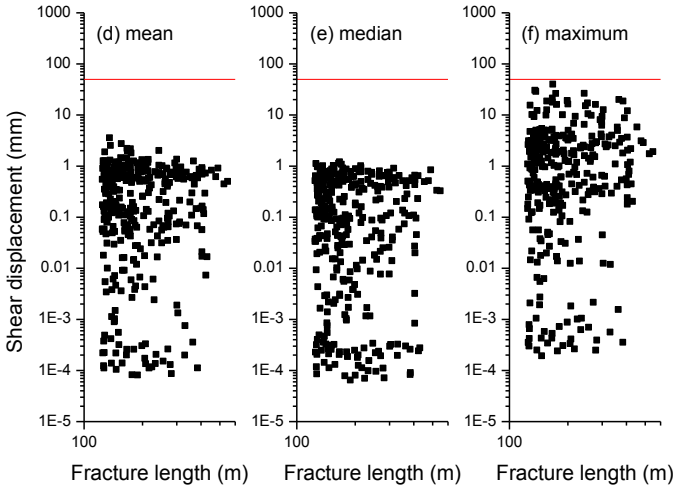


**Figure 56.** Distributions of the mean (a and d), median (b and e), and maximum (c and f) shear displacements of the fractures resulting after 50 years of sequential panel heating under adjusted power control in this report. Top row figures (a to c) are the results before eliminating the numerical artefacts and the bottom row figures (d to f) are after eliminating the numerical artefacts in PFC2D.

## 7.6. Summary of the results in this report

Table 7 lists the key results of the six modelling cases in this report, where the columns of the table are explained as follows:

- Column A: Loading condition of the model and the model type
  - T: Thermal induced;
  - EQ: Earthquake induced;
  - H: Horizontal section model;

    - V: Vertical section model
- Column B: Key variations in the modelling
    - Sim: Simultaneous panel heating;
    - Seq: Sequential panel heating;
    - DFN realization
    - Activated deformation zone for earthquake modelling;
    - Occurrence time of earthquake.
- Column C: Moment magnitude of the deformation zone activation with assumption of full size
- Column D: Total number of repository fractures in the DFN realizations
- Column E: Number of repository fractures of which median shear displacement exceed 50 mm, in each trace length class, e.g. Class 1/2/3/4 for the horizontal section model, and Class 1/2 for the vertical section model, for:
    - Thermal induced (T) modelling: at the end time of the simulation (3,000 years for the horizontal section model and 10k years for the vertical section model);
    - Thermal and earthquake induced (T+EQ): (first row) after 100 years of repository heating, (second row) after occurrence of an earthquake
- Column F: Maximum median shear displacement (mm) of the repository fractures in each length class, e.g. Class 1/2/3/4 for the horizontal section model and Class 1/2 for the vertical section model, for:
    - Thermal induced (T): at the end time of the simulation (3,000 years for the horizontal section model and 10k years for the vertical section model);
    - Thermal and earthquake induced (T+EQ): (first row) after 100 years of simultaneous heating, (second row) after occurrence of an earthquake

**Table 7.** Summary of the results of eight modelling cases.

| A | B | C | D | E | F |
|---|---|---|---|---|---|
| T (H) | Sim; DFN03h | - | 346 | 0/0/0/0 | 0.9/0.7/0.7/0.6 |
| | Seq; DFN03h | - | 346 | 0/0/0/0 | 0.9/0.7/0.7/0.6 |
| T (V) | Sim; DFN06v | - | 31 | 0/0 | 25.6/44.0 |
| | Seq; DFN06v | - | 31 | 0/0 | 25.5/43.6 |
| T+EQ (H) | Sim; DFN03h; ZFMWNW0809A; 100 years | 4.7 | 346 | 0/0/0/0<br>0/0/0/0 | 0.9/1.4/0.7/0.6<br>2.7/2.0/2.0/0.7 |
| T+EQ (V) | Sim; DFN06v; ZFMA3; 100 years | 4.8 | 31 | 0/0<br>0/0 | 1.2/13.1<br>1.9/46.1 |

# 8. The Consultants' overall assessment and conclusions

The Authors have conducted three campaigns of 2D numerical modelling related to the influence of heating and earthquakes on the repository for spent nuclear fuel at Forsmark with horizontal and vertical sections of the repository. In addition, the Authors have conducted basic and fundamental investigations on how rock fractures are represented in PFC2D and their displacements under shear loading.

The first modelling campaign deals with shear displacement of a rock fracture represented by a collection of smooth joints. In the second modelling campaign, shear displacement of the repository fractures and seismic events induced by the heat from canisters containing the spent nuclear fuel were conducted. The third modelling campaign deals with superposition of heat generation and seismic events on selected deformation zones during the short term period of the repository (e.g. operation and/or after closure) under the present-day stress field. An earthquake is modelled in a generic way, where the strain energy stored due to the stress field at a specific deformation zone is released instantaneously.

From the results of the three modelling campaigns, general conclusions can be drawn as listed below:

- Shear displacement of a fracture represented by a collection of smooth joints show a good match to the analytical solution in case of an isolated fracture under shear loading. However, in case of multiply intersecting fractures, a numerical artefact of the PFC2D code, which is due to the rigidity of the particles, tends to overestimate the shear displacement results and produce outliers. Therefore, for a representative and conservative value of shear displacement of the fractures and to exclude these outliers, the Authors have used throughout the report the median value of shear displacement of the collection of smooth joints forming a target fracture.
- The Authors also presented a method that can eliminate the influence of the numerical artefacts on the calculations of shear displacement of the repository fractures with the PFC2D code. Simulations of the modelling cases with this method may result in more reliable estimates of the fracture shear displacement, and in that case the maximum value of the fracture shear displacement could be used for the safety assessment of the repository.
- Heat from the disposed spent nuclear fuel can induce shear of the repository fractures in the repository. The results of the horizontal section models show that there are no fractures within or outside the deposition panel footprints exceeding the canister damage threshold of 50 mm at the repository depth during the simulated time period of 3,000 years. Also the vertical section models show that there are no fractures with shear displacement larger than 50 mm until 10,000 years after start of the repository heating.
- In the horizontal section model, the occurrence of an earthquake at deformation zone ZFMWNW0809A with magnitude $M_w$4.7 after 100 years of heating increases the fracture shear displacement. Also in the vertical section model, the occurrence of an earthquake at deformation zone ZFMA3 after 100 years of heating increase the fracture shear displacement. However, all fractures in both the horizontal and vertical section models

undergo a shear displacement of less than the canister damage threshold of 50 mm.

- It is the Authors' conclusion that, taking properly into account the effects of the numerical artefacts in PFC2D models and the 2D nature of the modelling, the integrity of the canisters of a repository of spent fuel in crystalline rock can be demonstrated. This is based on the fact that there are no fractures exceeding a shear displacement threshold of 50 mm, either induced by heating or by a combination of heating and tectonic seismic loading occurring during the operation or at short term after the closure of a repository.

# 9. The Consultants' recommendations

Several issues are addressed by the Authors and deserve further study.

*Discrete Fracture Network (DFN) realizations*

Among the ten DFN realizations provided to the Authors by SSM, two networks are chosen in this study. To draw more general conclusions about the sensitivity and influence of DFN on the modelling results, the Authors suggest that additional simulations shall be conducted with different DFN realizations.

*Target fractures of length shorter than 125 m*

The DFNs adopted have fracture length in the range between 125 and 600 m. As some of the earthquake modelling cases show that the shortest fractures might have large shear displacement, it is expected that target fractures that are even shorter than 100 m could undergo large shear displacement under particular circumstances. Therefore, the Authors suggest that the fracture length range of the DFNs should be enlarged to contain smaller fractures.

*Damage at the fracture intersections*

Concentrated stress at the fracture intersection may lead to failure of the rock mass, which cannot be captured in the present PFC2D model due to non-breakable and rigid particles. This artefact is found to be the main reason for the shear displacement spikes at the fracture intersections. To solve this problem, a "virtual damage" law should be developed and implemented in the modelling where a particle representing intact rock is checked to see if the stresses are high enough to induce failure of the rock inside it. If the stresses exceed the strength limit in the "virtual damage" law, the energy concentrated at the particle can then be distributed to the neighbouring particles and contacts. Using this approach, the singularity problem related to the shear displacement spikes at the fracture intersection, also called outliers, may be removed. Another effect of stress concentrations and particle rigidity are "rattler particles". The Authors have developed a scheme by FISH programming in the PFC2D code to detect and eliminate the rattlers, and to overlook at the smooth joints attached to the rattler particles when calculating the shear displacement of target fracture fractures. These scheme could be advantageously implemented in PFC2D models.

*Sequential heating*

Panel-by-panel sequential heating assumes that canisters are not disposed at the same time. This is more realistic than the modelling cases where all canisters are disposed at the same time throughout the whole repository and start releasing heat simultaneously. However, the simulated sequential heating applied in the report is considered still unrealistic and the Authors suggest conducting more realistic and detailed modelling of sequential heating following the estimated 2 days per one canister deposition rule presented by SKB.

*Generic earthquake modelling*

Release of the stored strain energy is simulated by lowering the bond strength of the smooth joint contacts in the activated deformation zone. The Authors suggest that, in addition to lowering of the strength parameters, also lowering of joint normal and shear stiffness should be tested to observe how it affects the earthquake activation magnitudes and the after-shock behaviour. Also, lowering of the strength parameters

in several steps is suggested as a way of emulating less brittle rupturing of the deformation zones.

*Earthquake activation time during thermal/operational phase of the repository*

In the heating and earthquake induced modelling cases, earthquake activation is simulated 100 years after start of simultaneous heating of the repository. The Authors suggest conducting several more modelling cases where an earthquake occurs at different selected times during the thermal/operational phase of the repository.

*Activation of multiple deformation zones*

In the heating and earthquake induced modelling cases, it is assumed that an earthquake occurs at a single deformation zone, e.g. ZFMWNW0809A or ZFMA3. However, there can be a situation where multiple deformation zones parallelly oriented, spatially close and/or connected are activated at the same time, e.g. Singö deformation zone (ZFMWNW0001) and its splays or multiple gently dipping deformation zones in the South-East area of Forsmark.

*3D modelling*

In order to reduce the uncertainties in the modelling results associated with 2D modelling of complex 3D problems, the Authors suggest performing 3D modelling of the Forsmark site with PFC3D. The seismic event modelling in this report and in Yoon et al. (2014) are based on assumptions that future earthquakes (i.e. post-glacial earthquakes) will take place at some of the repository bounding deformation zones, which are all vertical and steeply-dipping (ZFMWNW0809A, ZFMWNW2225, etc.). However, as raised by Lund (2015), gently dipping faults are more prone to reactivate due to the effect of glacial ice load. A few large deformation zones are located above (ZFMA2, ZFMA3, etc.) and below (ZFMA1) the repository depth, thus, it is necessary to conduct seismic event modelling under 3D settings, as also SKB has done (e.g. Fälth et al., 2010). A research project sponsored by SSM on this topic has been initiated (File No. SSM2014-3668).

# 10. References


Ahmadi O, Juhlin C, Ask M, Lund B, 2015. Revealing the deeper structure of the end-glacial Pärvie fault system in northern Sweden by seismic reflection profiling. Solid Earth 6, p. 621-632.

Backers T, Stephansson O, 2011. The influence of temperature and fluid pressure on the fracture network evolution around deposition holes of a KBS-3V concept at Forsmark, Sweden. SSM Research Report 2011:26, Swedish Radiation Safety Authority (SSM).

Backers T, Meier T, Gipper P and Stephansson O, 2014. Rock Mechanics – Confidence of SKB's models for predicting the occurrence of spalling – Main Review Phase. SSM Technical Note 2014: 10, Swedish Radiation Safety Authority (SSM).

Fälth B, Hökmark H, 2007. Mechanical and thermo-mechanical discrete fracture near-field analyses based on preliminary data from the Forsmark, Simpevarp and Laxemar sites. SKB R-06-89, Swedish Nuclear Fuel and Waste Management Co (SKB).

Fälth B, Hökmark H, Munier R, 2010. Effects of large earthquakes on a KBS-3 repository. Evaluation of modelling results and their implications for layout and design. SKB TR-08-11, Swedish Nuclear Fuel and Waste Management Co (SKB).

Hanks TC, Kanamori H, 1979. A moment magnitude scale. Journal of Geophysical Research 84(B5), p. 2348-2350.

Hökmark H, Lönnqvist M, Kristensson O, Sundberg J, Hellström G, 2009. Strategy for thermal dimensioning of the final repository for spent nuclear fuel. SKB R-09-04, Swedish Nuclear Fuel and Waste Management Co (SKB).

Hökmark H, Lönnqvist M, Fälth B, 2010. THM-issues in repository rock. Thermal, mechanical, thermo-mechanical and hydromechanical evolution of the rock at the Forsmark and Laxemar sites. SKB TR-10-23, Swedish Nuclear Fuel and Waste Management Co (SKB).

Itasca Consulting Group Inc, 2012. Technical Memorandum – 5.0 Parallel Bond Enhancement.

Leonard M, 2010. Earthquake fault scaling: Self-consistent relating of rupture length, width, average displacement, and moment release. Bulletin of Seismological Society of America 100, p. 1971-1988.

Lund B, 2015. Palaeoseismology of Glaciated Terrain. Encyclopedia of Earthquake Engineering DOI 10.1007/978-3-642-36197-5_25-1.

Manighetti I, Campillo M, Sammis C, Mai PM, King G, 2005. Evidence for self-similar, triangular slip distributions on earthquakes: Implications for earthquake and fault mechanics. Journal of Geophysical Research 110, B05302.

Martin CD, 2007. Quantifying in situ stress magnitudes and orientations for Forsmark. Forsmark state 2.2. SKB R-07-26, Swedish Nuclear Fuel and Waste Management Co (SKB).

Ofoegbu GI, Smart KJ, 2013. Rock Mechanics – Confidence of SKB's models for predicting the occurrence of a damage zone around the excavations. SSM Technical Note 2013:35, Swedish Radiation Safety Authority (SSM).

Pollard DD, Segall P, 1987. Theoretical displacements and stresses near fractures in rock: with application to faults. Fracture Mechanics of Rock. Academic Press Inc, London, p. 277-349.

Probert T, Claesson J, 1997. Temperature field due to time-dependent heat sources in a large rectangular grid. II. Application for the KBS-3 repository. SKB TR-97-27, Swedish Nuclear Fuel and Waste Management Co (SKB).

Shen B, 2014. Development and applications of rock fracture mechanics modelling with FRACOD: A general review. Geosystem Engineering 17, p. 235-252.

SKB, 2011. Long-term safety for the final repository for spent nuclear fuel at Forsmark Main report of the SR-Site project Volume I. SKB TR-11-01, Swedish Nuclear Fuel and Waste Management Co (SKB).

Sausse J, Dezayes C, Dorbath L, Genter A, Place J, 2010. 3-D model of fracture zones at Soultz-sous-Forêts based on geological data, image logs, induced seismicity and vertical seismic profile. Comptes Rendus Geoscience 342, p. 531-545.

Sundberg J, Wrafter J, Ländell M, Back P-E, Rosén L, 2008. Thermal properties Forsmark. Modelling stage 2.3. Complementary analysis and verification of the thermal bedrock model, sage 2.2 SKB R-08-65, Swedish Nuclear Fuel and Waste Management Co (SKB).

Wells DL, Coppersmith KJ, 1994. New empirical relationships among magnitude, rupture length, rupture width, rupture area, and surface displacement. Bulletin of Seismological Society of America 84, p. 871-889.

Yoon JS, Stephansson O, Min K-B, 2014. Relation between earthquake magnitude, fracture length and fracture shear displacement in the KBS-3 repository at Forsmark Main Review Phase, SSM Technical Note 2014:59, Swedish Radiation Safety Authority (SSM).

Zoback MD, Gorelick SM, 2012. Earthquake triggering and large-scale geologic storage of carbon dioxide. Proceedings of the National Academy of Sciences (PNAS) 109(26), p. 10164-10168.

# Acknowledgement

The Authors like to thank Mr. Saeha Kwon of Seoul National University for the heat conduction analysis by COMSOL. We thank Dr. Baotang Shen of CSIRO Energy for his comments and help in FRACOD2D analyses of intersecting fractures, and Sacha Emam and Matthew Purvance of ITASCA for their comments and technical advices on the PFC2D modeling in this report.

**APPENDIX A**

# Coverage of SKB reports

| Reviewed reports | Reviewed sections |
|---|---|
| TR-10-23 | Section 5. Thermal evolution |
| TR-97-27 | Section 3. Local solution |
| R-06-89 | Section 4. Description of models, Figure 4.6 |
| TR-08-11 | Entire report |

# Influence of the particle size and the fracture insertion order on the shear displacement distribution

In this Appendix, close-up views of the seven locations of fracture intersections in the PFC2D models in Section 2.3 in this report for the case of fracture insertion order of 12345. Displacement fields at seven fracture intersections in the coarse and fine particle assemblies are examined (Figure B-1). Figures of fracture intersection where the shear displacement spike takes place are indicated by asterisk '*' in Figure B-2. Left column figures are from the coarse particle assembly and right column figures are from the fine particle assembly.

Distributions of smooth joint shear displacements of five intersecting fractures in the fine particle assemblies with different fracture insertion orders are shown in Figure B-3.

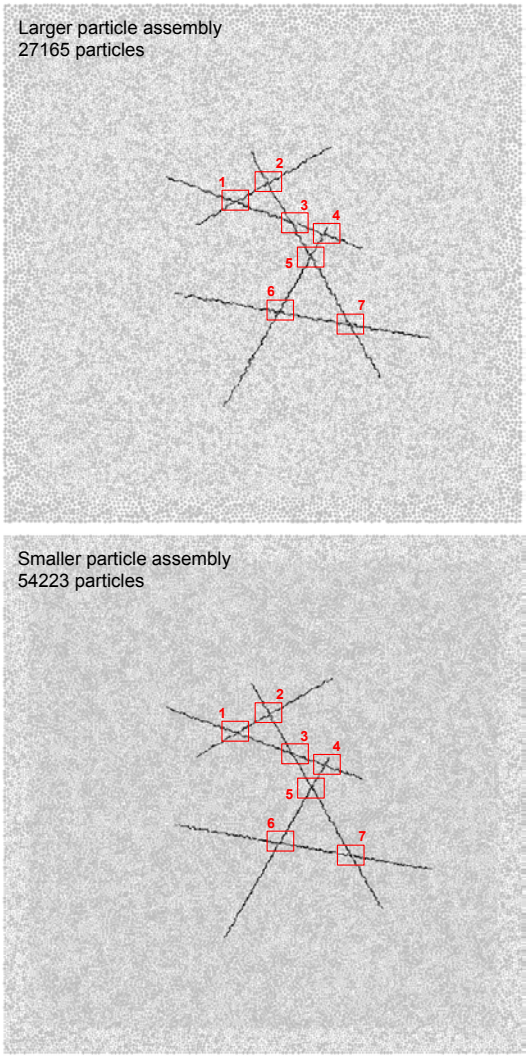


**Figure B-1.** Particle assemblies with (top) coarse particles and (bottom) fine particles, containing five intersecting PFC fractures. Fracture intersections are numbered for referencing the close-up views.

| | |
|---|---|
| Intersection 1 | Intersection 1 |
| 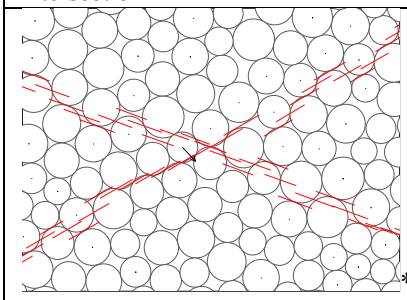 | 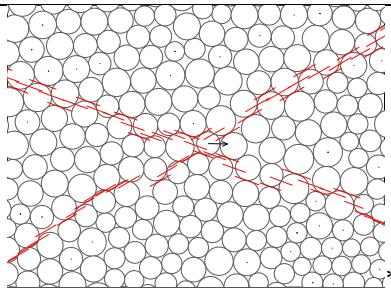 |
| Intersection 2 | Intersection 2 |
| 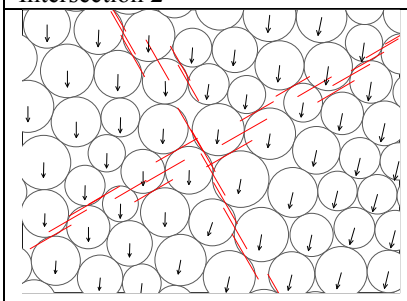 | 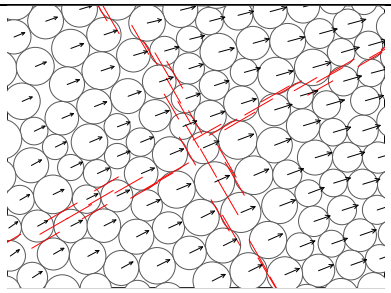 |
| Intersection 3 | Intersection 3 |
| 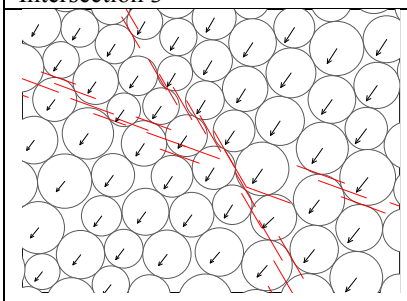 | 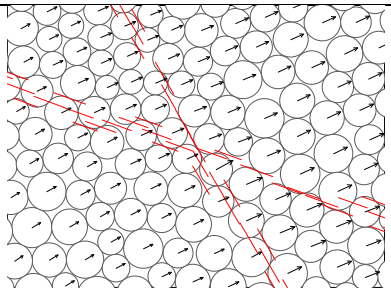 |
| Intersection 4 | Intersection 4 |
| 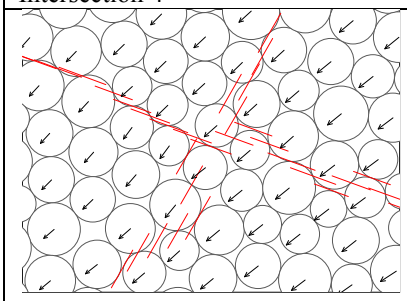 | 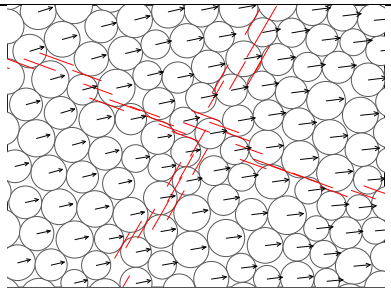 |
| Intersection 5 | Intersection 5 |
| 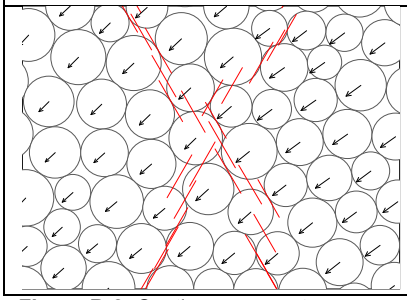 | 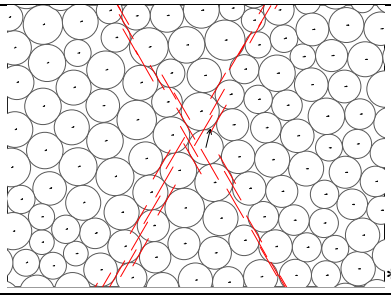 |

**Figure B-2.** Continues on next page.

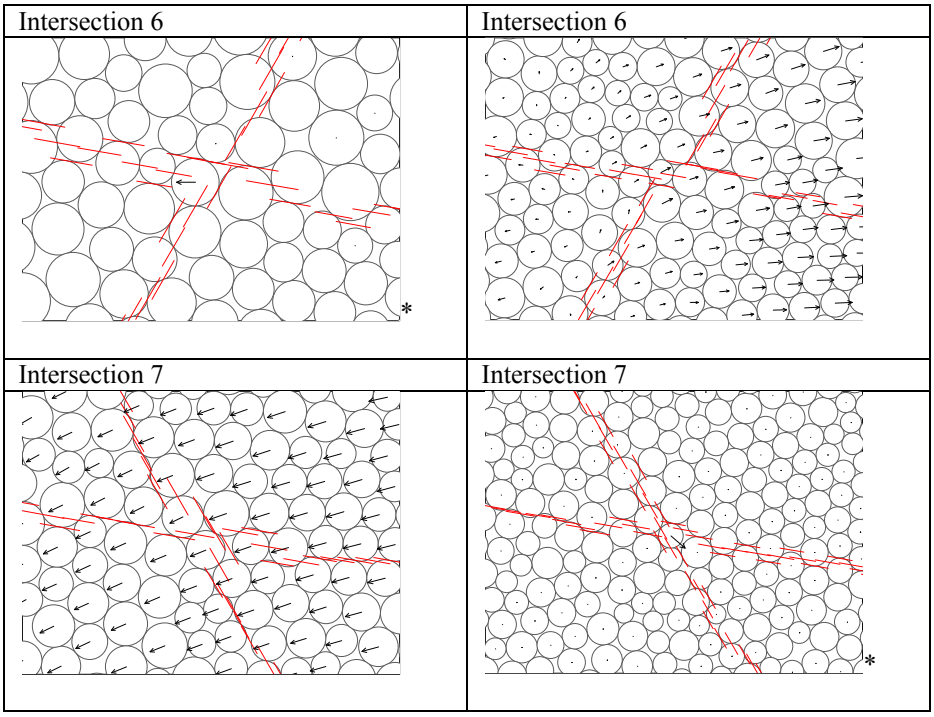


**Figure B-2 cont.** Close-up views of the seven locations of fracture intersections in the (left) coarse and (right) fine particle assemblies.

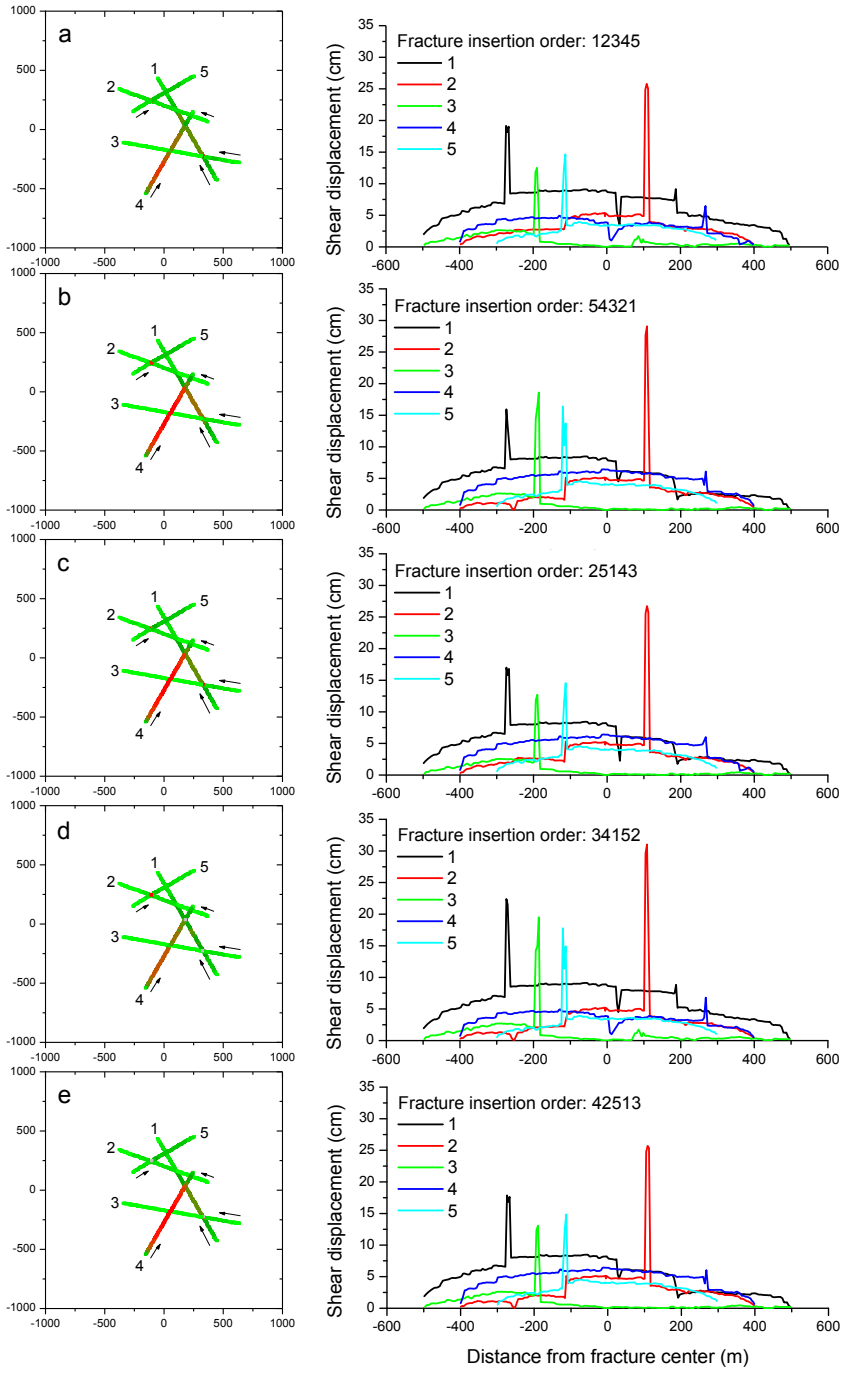


**Figure B-3.** Shear displacement profiles of five intersecting fractures in the fine particle assembly with different fracture insertion orders of (a) 12345, (b) 54321, (c) 25143, (d) 34152, and (e) 42513.

# Results of FRACOD2D modelling

In this Appendix, the fracture setting shown in Appendix B is tested using the boundary element based code called FRACOD2D (Shen, 2014) which enables simulation of propagation of fractures at the tips.

FRACOD2D is a two-dimensional boundary element code designed to simulate fracture propagation and interaction of randomly distributed fracture in an elastic rock medium. The code uses Displacement Discontinuity Method (DDM) and can simulate both tensile and shear failures. The code has been used in other SSM reports such as in Backers and Stephansson (2011).

Input parameter and material and fracture properties are listed below in Table C-1. It should be noted that, the fracture toughness values for Mode I and Mode II are set larger by three orders of magnitude. Such setting of the fracture toughness is necessary to make the test condition consistent to the PFC2D tests (Appendix B) and the analytical solution, where the shear displacements are concentrated only at the fracture trace. This allows no fracture propagation.

**Table C-1.** Material properties used in FRACOD2D modelling.

| Property | Value | Remark |
|---|---|---|
| Rock Young's modulus | 59 GPa | Results from uniaxial compression test |
| Rock Poisson's ratio | 0.28 | |
| Rock Mode I fracture toughness | 2.5e3 MPa√m | |
| Rock Mode II fracture toughness | 4.0e3 MPa√m | |
| Fracture normal stiffness | 60.4 GPa/m | |
| Fracture shear stiffness | 3.4 GPa/m | |
| Friction angle | 5.7 deg. | 0.1 friction coefficient. |
| Cohesion | 0 MPa | |
| Fracture dilation angle | 0 deg. | |

## Single isolated fracture subjected to a shear loading

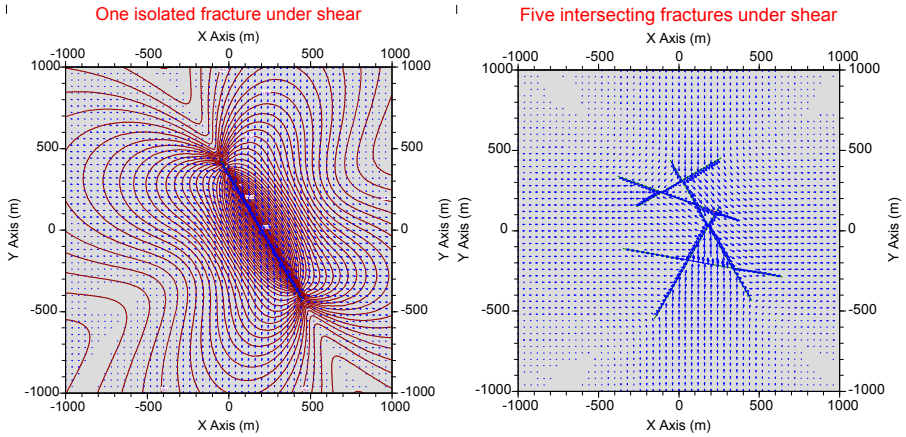


**Figure C-1.** Distribution of displacement shown by contours (left) and by vectors (right).

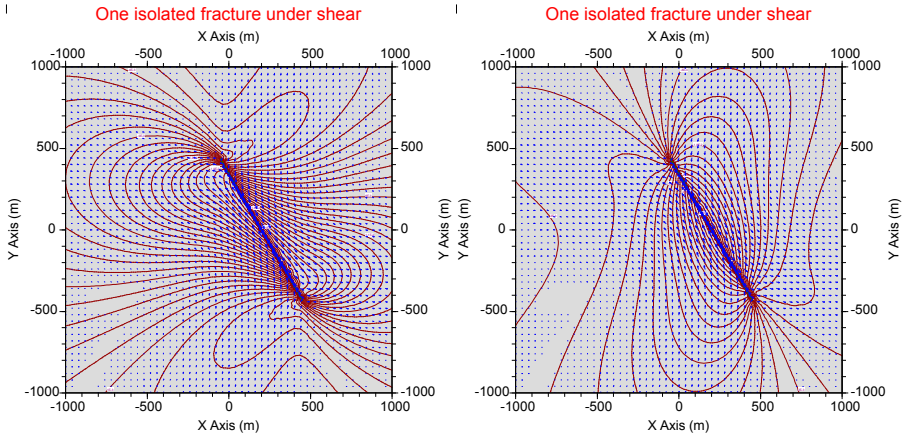


**Figure C-2.** Distribution of displacement in x-direction (left) and in y-direction (right).

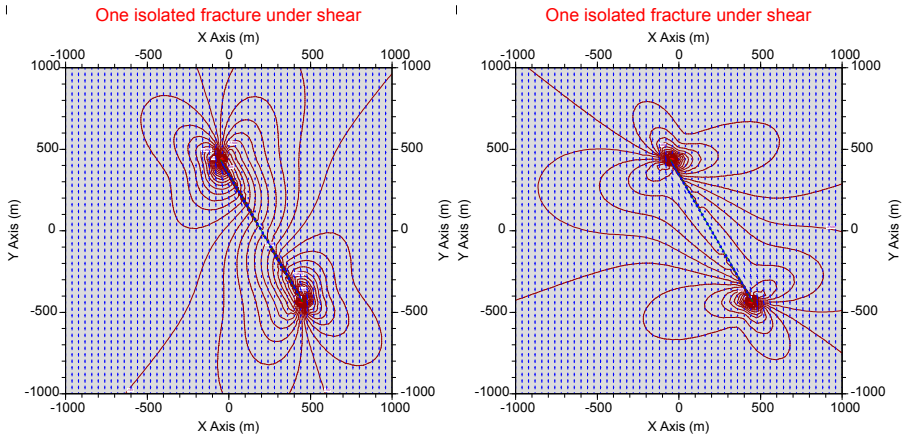


**Figure C-3.** Distribution of maximum (left) and minimum (right) principal stresses.

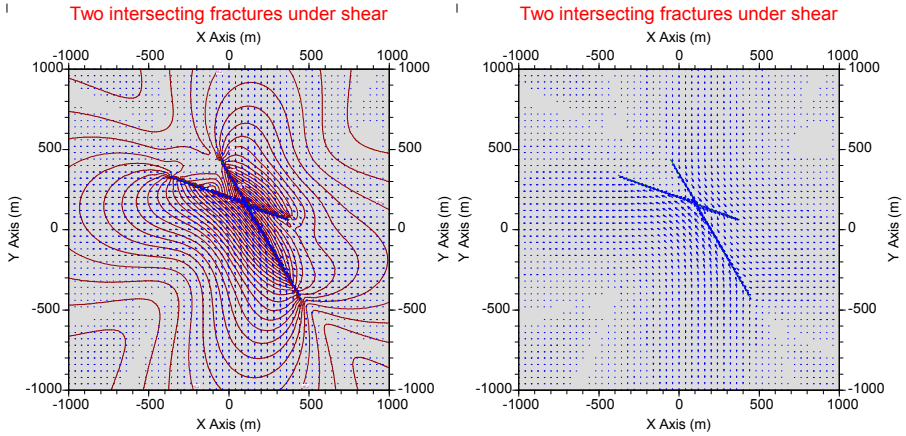


**Figure C-4.** Distribution of displacement shown by contours (left) and by vectors (right).

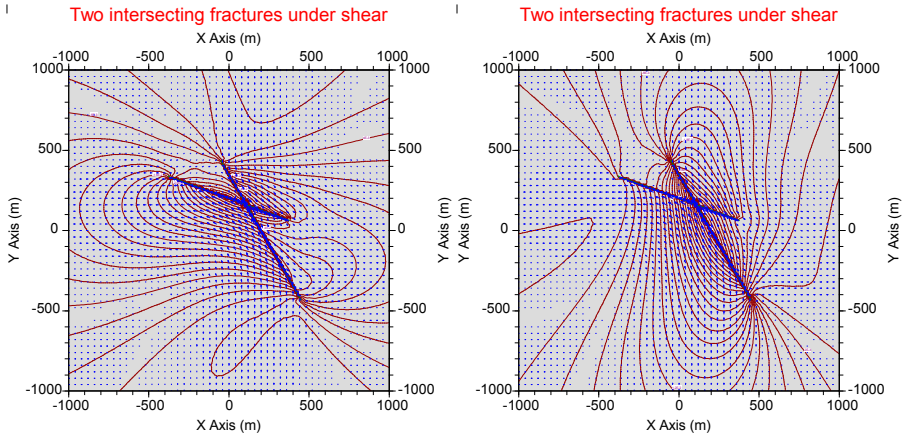


**Figure C-5.** Distribution of displacement in x-direction. (left) and in y-direction (right).

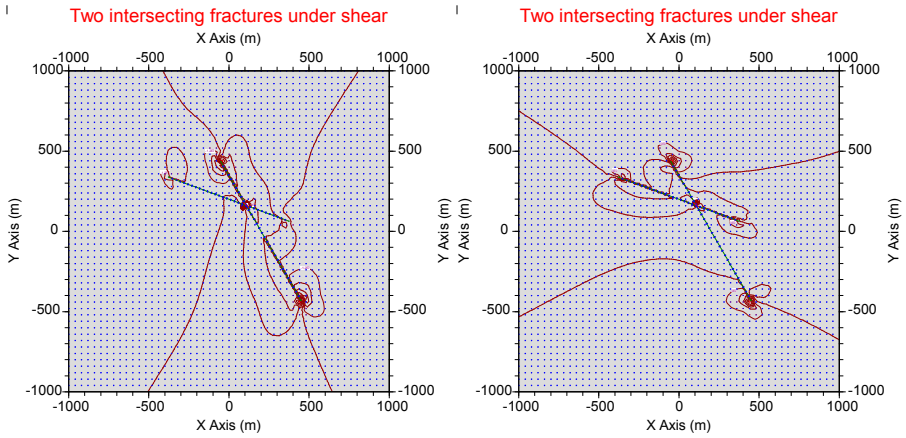


**Figure C-6.** Distribution of maximum (left) and minimum (right) principal stresses.

Five intersecting fractures subjected to a shear loading

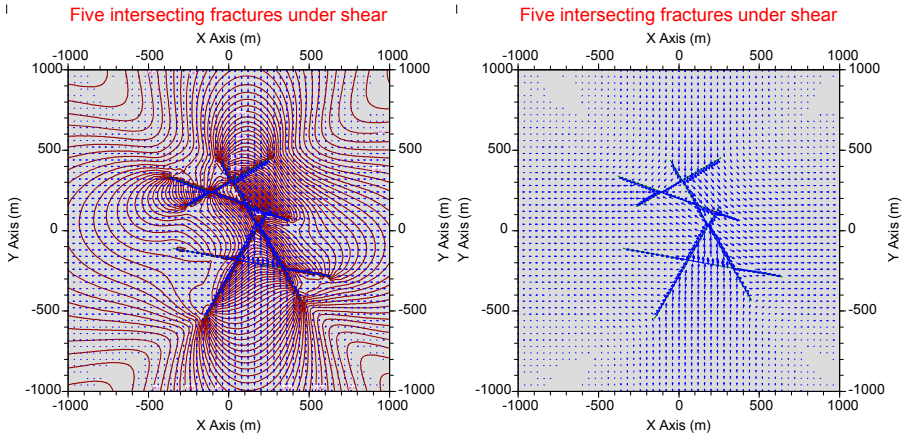


**Figure C-7.** Distribution of displacement by contours (left) and by vectors (right).

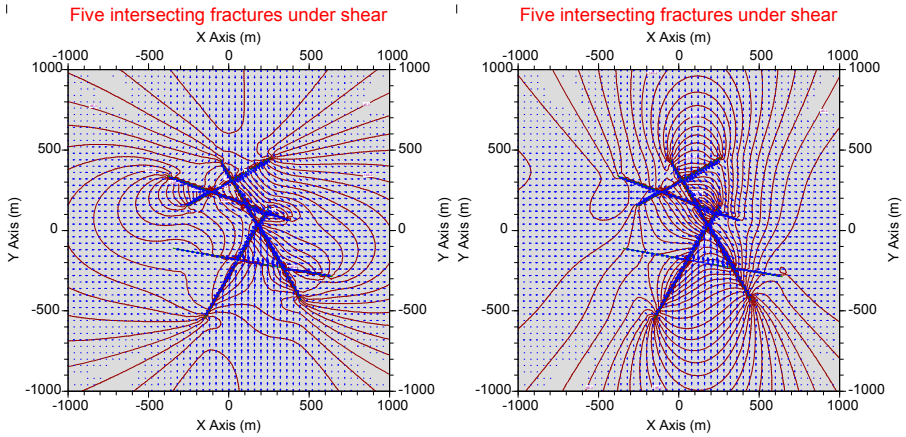


**Figure C-8.** Distribution of displacement in x-direction (left) and in y-direction (right).

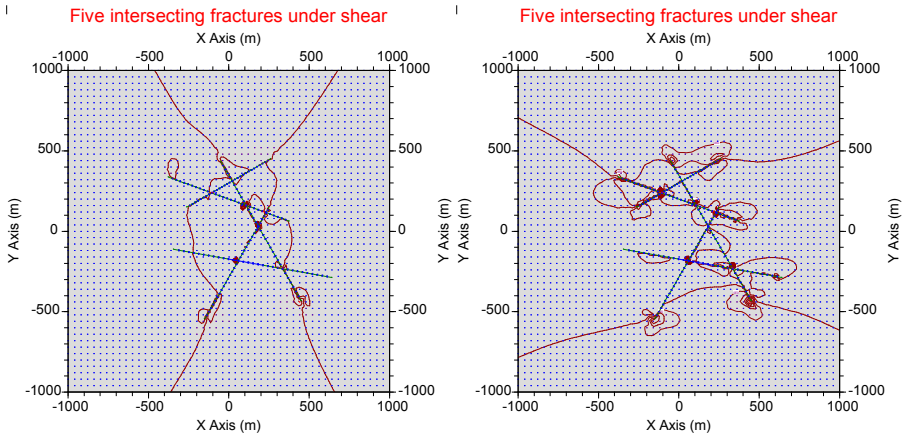


**Figure C-9.** Distribution of maximum (left) and minimum (right) principal stresses.

Below two figures are the results of PFC2D modelling showing the distributions of the maximum and minimum principal stresses in the model with five intersecting PFC fractures. The fracture intersection where the particle displacement singularity takes place (indicated by the arrow) is enlarged and show on the right.

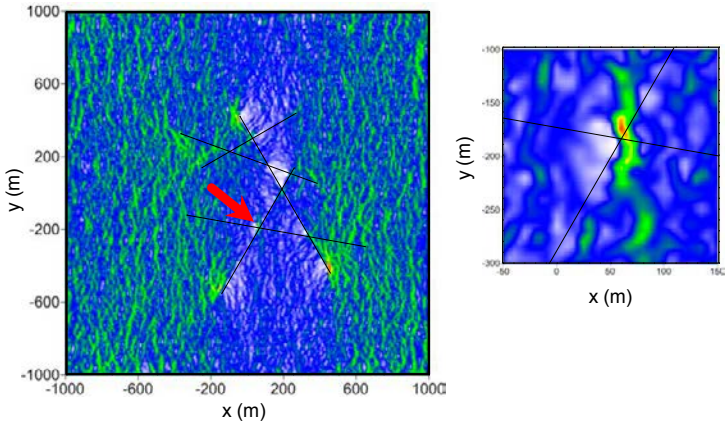


**Figure C-10.** Distribution of the maximum principal stress in the PFC2D model with five intersecting fractures under shear. Enlarged view of the fracture intersecting area (indicated by the arrow) is shown on the right.

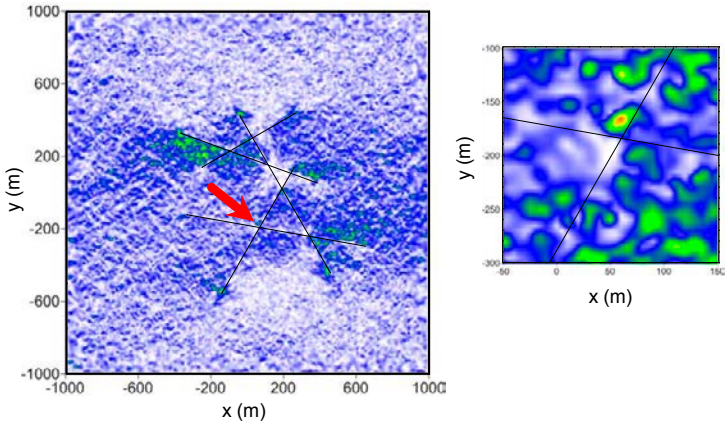


**Figure C-11.** Distribution of the minimum principal stress in the PFC2D model with five intersecting fractures under shear. Enlarged view of the fracture intersecting area (indicated by the arrow) is shown on the right.

# Results of COMSOL modelling

In this Appendix, we present a series of heat conduction analysis using COMSOL. The main purpose of the modelling using FEM based COMSOL software is to compare the temperature evolution in 3D and in 2D. The analysis by COMSOL served as a basis for the thermal analysis in PFC2D.

Figure D-1 shows the modelled geometry. The repository is represented by a plane with thickness of 4.8 m. The heat sources are distributed in the plane with spacing of 6 m and 40 m for the deposition holes and for the deposition tunnels, respectively. Figure D-2 shows the boundary conditions and the heat power assigned to the repository. The power function P(t) is identical to the heat power curve shown in black in Figure 15. The power function is divided by the spacing between the deposition holes (6 m) and between the deposition tunnels (40 m). It is further divided by the thickness of the repository, 4.8 m. This was necessary as the PFC2D model has a thickness of 1 m in the out-of-plane direction.

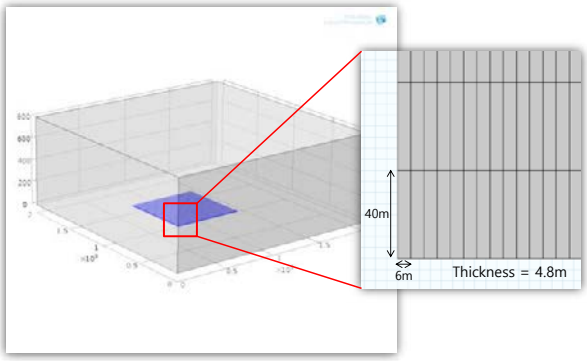


**Figure D-1.** Geometry of the COMSOL model.

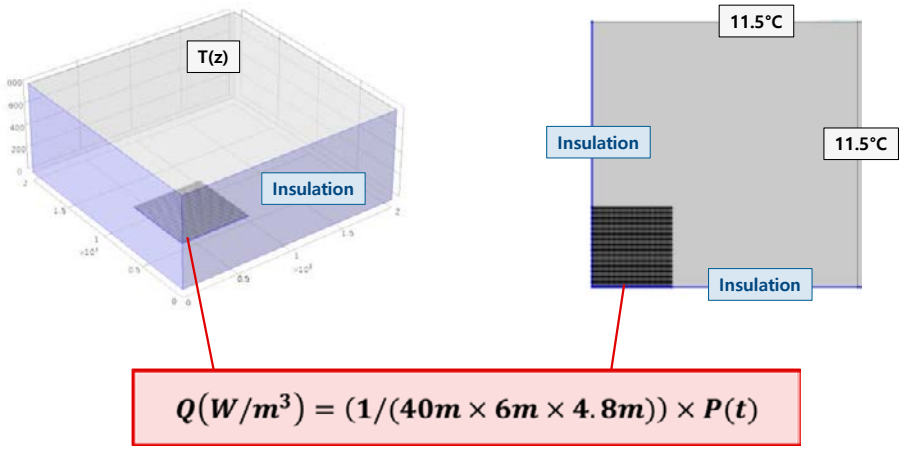


**Figure D-2.** Boundary conditions and the power function applied to the plane heat source.

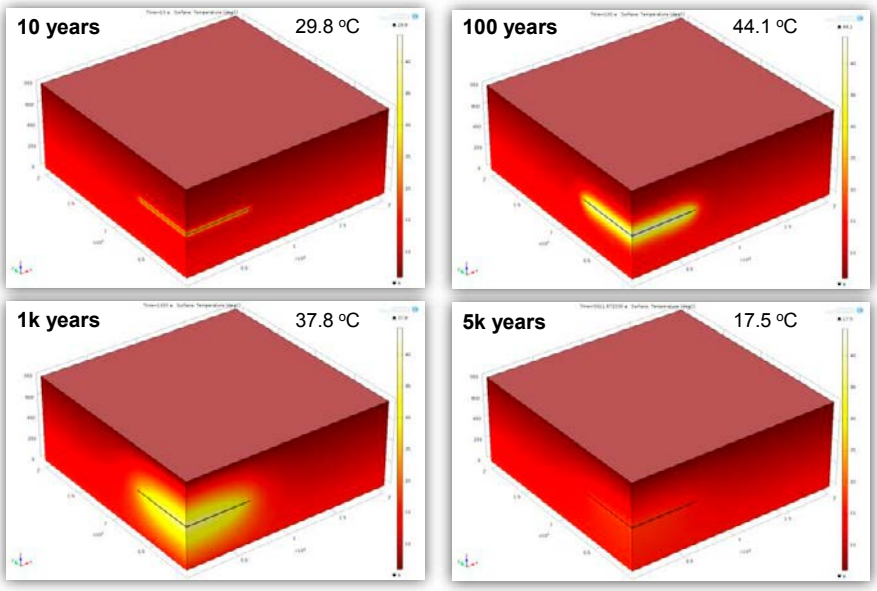


**Figure D-3.** Distribution of temperature and the maxim temperature in 3D model at selected times.

Figure D-3 shows 3D distribution of the temperature and the maximum temperature at the selected times. The results indicate that the temperature reached the maximum of 44°C after 100 years of heating. Figure D-4 shows temporal changes of the temperature monitored at several selected points in the heat panel. The maximum temperature of 44°C is simulated at Point A (at centre of the panel) after 100 years of heating.

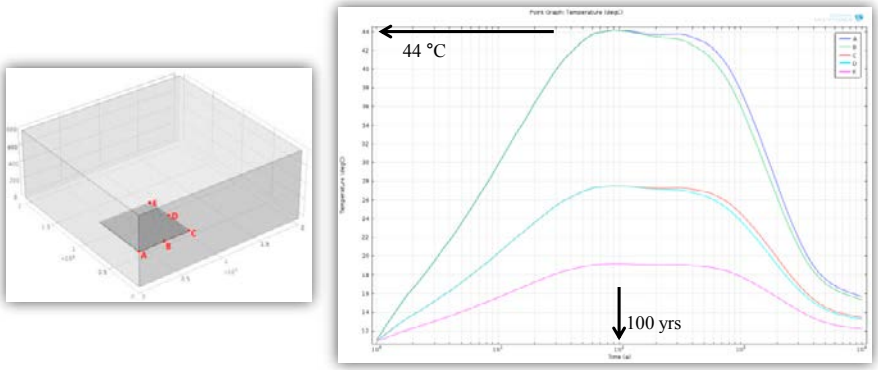


**Figure D-4.** Temporal changes of the temperature monitored at several selected points in the plane heat source.

The model is changed to 2D setting where the top and the bottom planes are assigned insulated boundary conditions. The same heat power is applied to the 2D model. The simulated temperature at the centre of the panel reaches the maximum of 3600 °C after 1000 years of heating (Figure D-5).

The model is then changed again to 3D setting with insulated boundary condition assigned to the top and the bottom planes. The heat plane has unit length in the z-

direction. The simulated temperature at the centre of the panel reaches the maximum of 3600 °C after 1000 years of heating (Figure D-6). The results are identical to those from the 2D modelling.

The results of the COMSOL modelling demonstrate that the temperature distribution in 2D model and in 3D model with unit length and with insulated boundary condition to the top and the bottom planes significantly overestimates the temperature evolution, e.g. 44 °C versus 3600 °C at the centre of the panel. The results demonstrate that the heat power of the full size canister (black curve in Figure 15) should be modified properly in the PFC2D modelling (red curve in Figure 15), in order to avoid overestimation of the temperature.

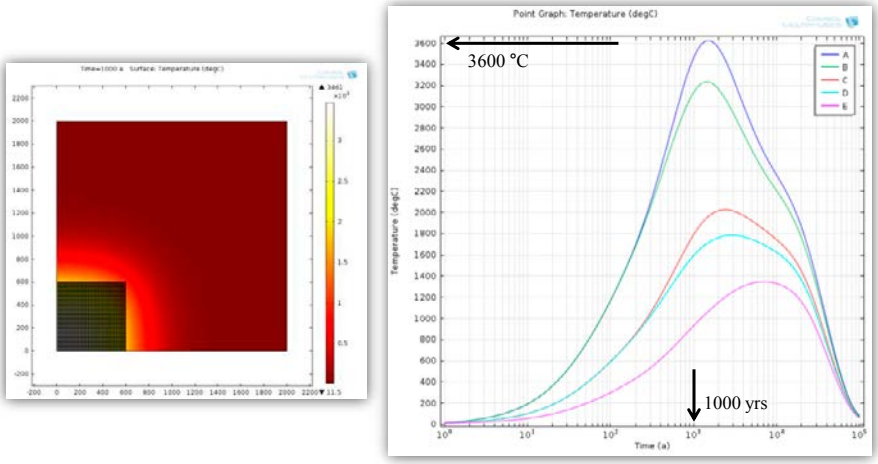


**Figure D-5.** Temporal changes of the temperature monitored at several selected points in the plane heat source simulated in 2D setting.

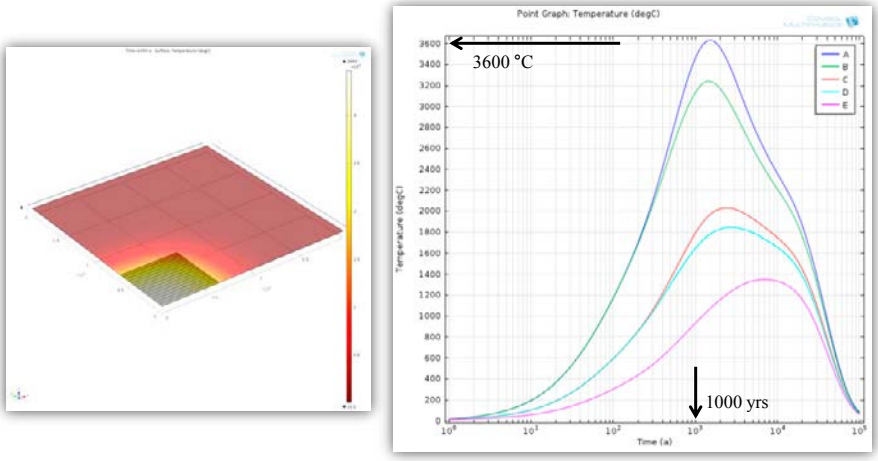


**Figure D-6.** Temporal changes of the temperature monitored at several selected points in the plane heat source simulated in 3D setting with unit length in z-direction.

**APPENDIX E**

# Additional plots of the modelling results

In addition to the results of the median shear displacement of the fractures shown in the main part of the reports, additional results are presented in this Appendix.

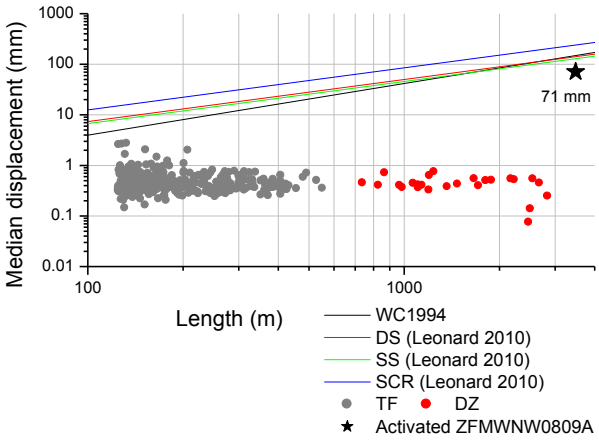


**Figure E-1.** Median shear displacement of the fractures (gray dots) and the deformation zones (red dots) with respect to the length induced by activation of ZFMWNW0809A at 100 years after start of simultaneous heating in the PFC2D horizontal section model with DFN03h realization. Median shear displacement of the activated ZFMWNW0809A is 71 mm and compared with the empirical relations from Wells and Coppersmith (1994) and Leonard (2010).

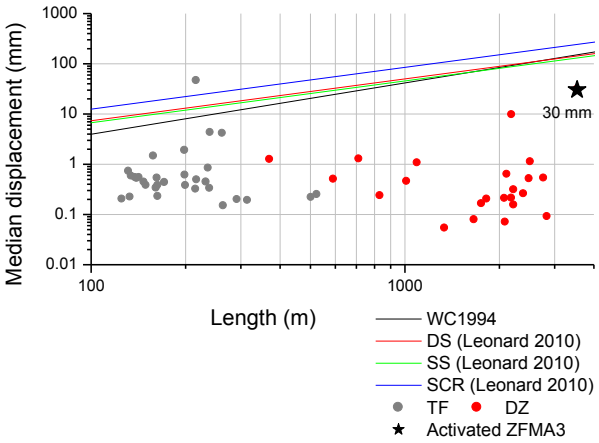


**Figure E-2.** Median shear displacement of the fractures (gray dots) and the deformation zones (red dots) with respect to the length induced by activation of ZFMA3 at 100 years after start of simultaneous heating in the PFC2D vertical section model with DFN06v realization. Median shear displacement of the activated ZFMA3 is 30 mm and compared with the empirical relations from Wells and Coppersmith (1994) and Leonard (2010).

2016:23

The Swedish Radiation Safety Authority has a comprehensive responsibility to ensure that society is safe from the effects of radiation. The Authority works to achieve radiation safety in a number of areas: nuclear power, medical care as well as commercial products and services. The Authority also works to achieve protection from natural radiation and to increase the level of radiation safety internationally.

The Swedish Radiation Safety Authority works proactively and preventively to protect people and the environment from the harmful effects of radiation, now and in the future. The Authority issues regulations and supervises compliance, while also supporting research, providing training and information, and issuing advice. Often, activities involving radiation require licences issued by the Authority. The Swedish Radiation Safety Authority maintains emergency preparedness around the clock with the aim of limiting the aftermath of radiation accidents and the unintentional spreading of radioactive substances. The Authority participates in international co-operation in order to promote radiation safety and finances projects aiming to raise the level of radiation safety in certain Eastern European countries.

The Authority reports to the Ministry of the Environment and has around 300 employees with competencies in the fields of engineering, natural and behavioural sciences, law, economics and communications. We have received quality, environmental and working environment certification.

**Strålsäkerhetsmyndigheten**
**Swedish Radiation Safety Authority**

SE-171 16 Stockholm
Solna strandväg 96

**Tel:** +46 8 799 40 00
**Fax:** +46 8 799 40 10

**E-mail:** registrator@ssm.se
**Web:** stralsakerhetsmyndigheten.se